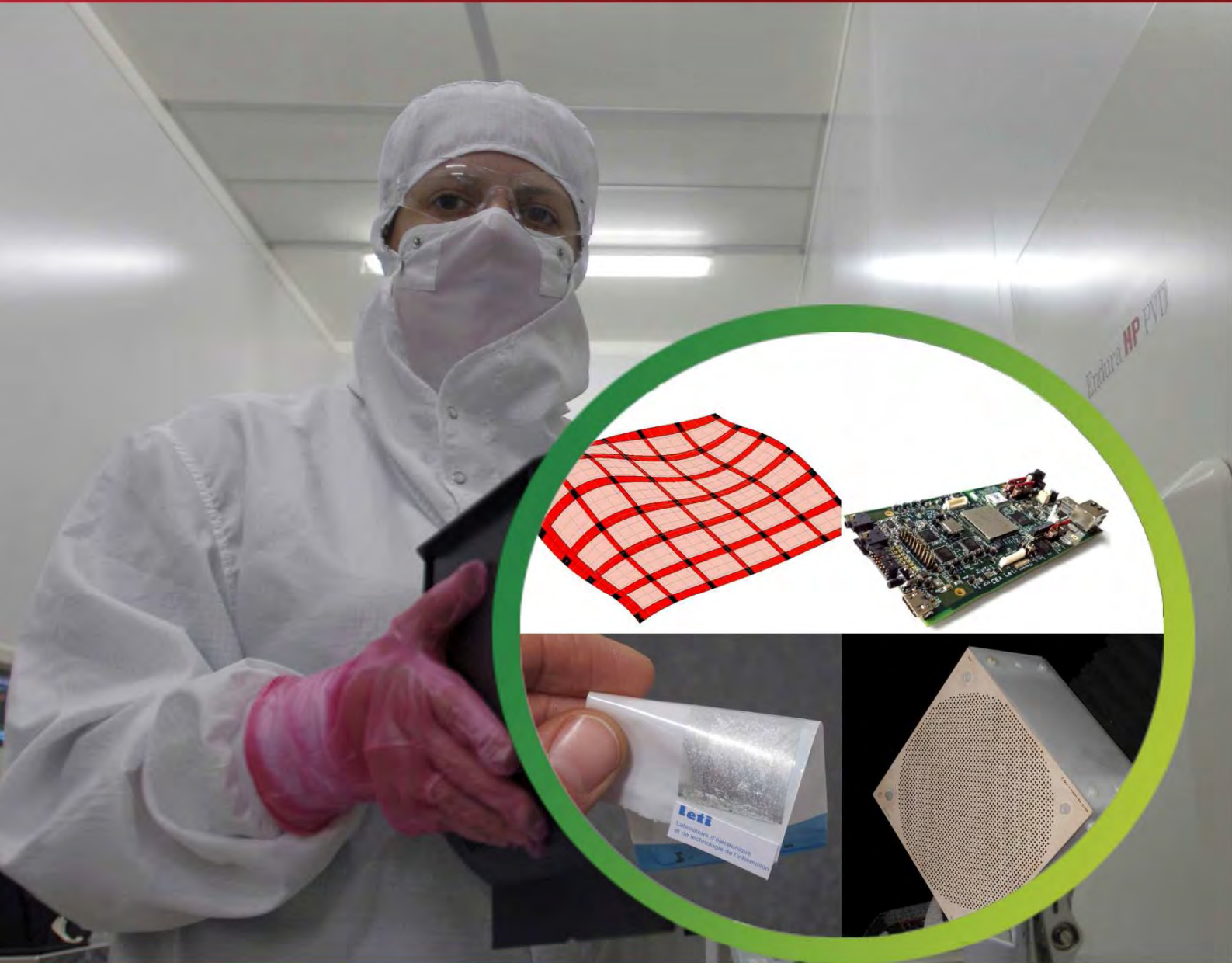


DE LA RECHERCHE À L'INDUSTRIE



leti



Annual Research Report 2014

Systems and Solutions  
Integration





## Systems and Solutions Integration

**Leti** is an institute of **CEA**, a French research-and-technology organization with activities in energy, IT, healthcare, defense and security.

By creating innovation and transferring it to industry, Leti is the bridge between basic research and production of micro- and nanotechnologies that improve the lives of people around the world.

Backed by its portfolio of 2,200 patents, Leti partners with large industrials, SMEs and startups to tailor advanced solutions that strengthen their competitive positions. It has launched more than 50 startups. Its 8,000m<sup>2</sup> of new-generation cleanroom space feature 200mm and 300mm wafer processing of micro and nano solutions for applications ranging from space to smart devices. Leti's staff of more than 1,700 includes 200 assignees from partner companies. Leti is based in Grenoble, France, and has offices in Silicon Valley, Calif., and Tokyo.

Visit [www.leti.fr](http://www.leti.fr) for more information

**Systems and Solutions Integration** research activities are mainly devoted to Telecommunications, Internet of Things and Power Management Systems. These activities include the design and development of fixed or nomadic devices and sensor networks with embedded power management, energy harvesting, sensors, data and information processing, RF communications and security functions. The R&D works are performed with academic or industrial partners with the strategic objective to improve the next generation of industrial products thanks to the integration of emerging nanotechnology techniques. Industrial partners range from SME to large international companies. Typical internal equipments are available to partnership R&D works such as RF Anechoic Chamber, Information Technology Security Evaluation Facility, Magnetometers Test Facility, and a Students Platform for Industrial Innovation.




## Systems and Solutions Integration



Edito	<b>1</b>
Key figures	<b>3</b>
Scientific activity	<b>5</b>
Cellular communications	<b>11</b>
Wireless short-range communications	<b>27</b>
Antennas and propagation	<b>37</b>
Sensors and systems	<b>47</b>
Energy	<b>57</b>
PhD degrees awarded in 2014	<b>63</b>





Edito

**Roland Blanpain**  
**Head of Systems and Solutions**  
**Integration Division**

Few years ago, CEA-LETI decided to focus drastically on SMI/SME support for innovation and technological transfer. The objective was, when relevant, to enrich or to upgrade future industrial products with advanced electronic functions to boost industry and employment. DSIS Division was created at CEA-LETI to coordinate this action in the field of Technologies for Information and Communication and Energy Management.

Based on MINATEC Campus in the Laboratory for Electronics & Information Technology (CEA-LETI), the Systems and Solutions Integration Division is today offering a large spectrum of technological solutions to foster the industry competitiveness. To propose such innovative capabilities, relevant research projects have to be raised and achieved. This document will introduce you on basic technological bricks investigated in the DSIS Division, sometimes in collaboration with other Leti or CEA laboratories or with external partnership.

Of course, a large part of research in Information and Communication technologies is devoted to new wireless transmission techniques. These works cover a large spectrum of our future daily life such as cellular networks, indoor communications, short range high data rate radio links but also contactless systems and more recently new relevant and efficient use of the old analog TV frequency bands.

A second key point is to provide technologies for miniaturized, efficient and smart sensors. This domain includes new conceptual physical approaches, such as arrays of sensors with embedded signal processing, and aims at delivering solutions close to industrial requirements.

Finally, the most emerging and promising works are dedicated to energy management, including improvement of global efficiency and environmental preserving aspects. Beyond the mandatory energy management for both the future electrical vehicle and the smart grid, this strategic area unveils new energy harvesting solutions for nomadic devices.





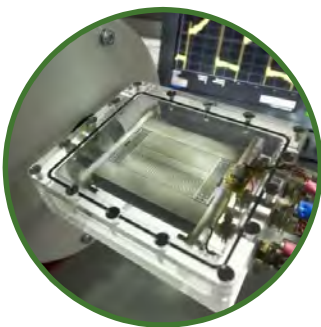
## Systems and Solutions Integration

### Key figures



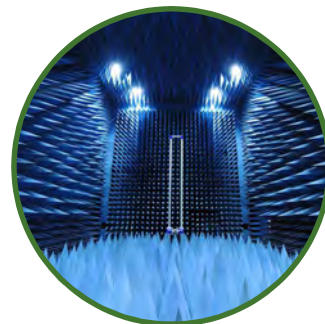
149 permanent researchers  
44 PhD students and post-docs  
48 short-term contracts

24 M€ budget  
90% external funding



47 patents granted in 2014  
400 patents portfolio  
31 book chapters and journals  
117 conferences and workshops

Technical facilities:  
3 anechoic chambers  
Magnetometer test ground  
Information Technology Security  
Evaluation Facility (ITSEF).



3 new common laboratories





## Scientific activity

### Publications

- 148 publications in 2014, including book chapters, and top journals or conferences such as IEEE journals, EWSHM, AGU meeting, EuMW, EuCNC, IEEE WCNC, IEEE GlobeCom, etc.

### Prize and Awards

- J-F. Pintos, project leader, received the 2<sup>nd</sup> prize FIEEC 2014 (Fédération des Industries Electriques, Electroniques et de Communication) for his work on miniature antennas for handheld terminals.

### Experts

- 1 Research Director, 1 International Expert, 9 Senior Experts, 12 Experts.

### Scientific Committees

- Conferences Technical Program Committees: IEEE RFID, IEEE ISWCS, COSADE, CROWNCOM, EuCNC, ICCVE, Euromicro DSD, ICCE, IEEE PIMRC, WPMC, IEEE ICUWB, IEEE VTC-Fall, BodyNets, IEEE ICC, MONAMI, IEEE WCNC, IEEE GlobeCom.
- IEEE DYSPAN standard committee, voting member in the working groups IEEE P1900.6 and IEEE P1900.7.
- ANR (National Research Agency), DGA (General Directorate for Armament), 5G PPP.

### Conferences and Workshops organizations

- Workshops and special sessions organized in the following conferences: EuCAP, EuCNC, IEEE CAMA, URSI GASS, IEEE ISWCS, Euromicro DSD.

### International Collaborations

- Univ. of Bologna, Catholic Univ. of Louvain-la-Neuve, Queens Univ. of Belfast, Czech Technical University.





# 1

## Cellular communications

*Beyond 4G mobile networks*

*Coding*

*FBMC technology*

*EMF exposure*



## Millimeter-wave access and backhauling for 5G mobile communication system

Research topics: mobile communications, millimeter-waves

A. De Domenico, D. Kténas, L. Dussopt, E. Calvanese Strinati, C. Dehos, and J. L. González

**ABSTRACT:** The exponential increase of mobile data traffic requires disrupting approaches for the design of future 5G systems. This work investigates the extension of cellular networks with millimeter-wave backhaul and access links. We evaluate the feasibility of this technology and present the requirements from the transceiver, antennas, and modulation scheme points of view. Furthermore, a dedicated system architecture to support this technology is described, technical challenges are discussed, and design options highlighted.

Millimeter-wave (mmW) technology was recently proposed to enable broadband radio access and backhauling in future wireless networks (see Fig.1). The large bandwidth available at frequencies in the 30–300 GHz range will enable unprecedented connection speed to mobile users, and traffic capacity to network operators. In our research, we focus on 60 and 70/80 GHz bands that provide notable advantages with respect to the 30 GHz technology since larger bandwidths are available, they are license free or light-licensed, they enable higher frequency reuse, and they are available almost worldwide.



Figure 1: mmW access and backhaul physical architecture.

In the foreseen 5G heterogeneous network, the legacy technologies guarantee low-latency, basic coverage, voice, and signaling to mobile users, while mmW small cells provide the ultimate capacity when needed. mmW equipments must support all kinds of installation locations not originally meant for telecom infrastructure such as building facades. The radio equipment should be as cheap as possible, and installation and maintenance should be limited to reduce significant additional costs. Reliability must be high, and there must be features to support easy installation: automatic beamsteering and Self-Organized Networking (SON) features are key points in mmW networks. Whenever a mobile device connected to a legacy network requires massive data exchange within the coverage of a mmW small cell, the serving Macro Base Station has to assist the User Equipment to perform the mmW cell discovery.

Control/user plane (C/U plane) splitting enables this new paradigm: with C/U splitting, mobile terminals can receive system information and issue access requests to a base

station and getting assigned radio resources for high-rate data transmission at a different base station (Fig.2).

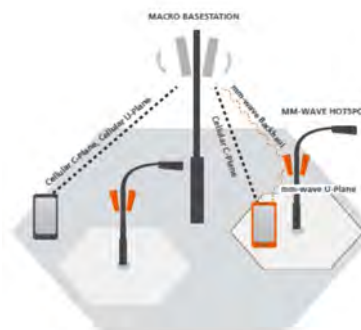


Figure 2: Control/user plane split concept.

Future mmW backhaul deployment will require a small form factor, low power, low cost, and better tolerance to vibration will be required, while providing 10 Gb/s typical aggregated data rates. In the E-band, some recent research efforts have started to respond to these requirements using the SiGe BiCMOS technology. For short links, the 60-GHz band may offer an alternative to the E band and enable the use of an even lower-cost technology such as complementary metal oxide semiconductor (CMOS).

From the access perspective, the 60-GHz mobile transceiver radio shall be compatible with both IEEE 802.11ad standard and future mmW technology for outdoor radio access. This prerequisite imposes small aperture antennas at the mobile side and thus directive beamforming antennas at the mmW base station. Power consumption constraints will impose simple modulation schemes. The OFDM modulation used in IEEE 802.11ad is very well suited for indoor environments; however, it may not be the best option for longer-range outdoor links. Additionally, it may require power consumption not compatible with a battery-operated mobile terminal. Indeed, single-carrier modulations, in spite of offering less spectral efficiency and robustness, may prove to be more suitable for handheld terminals.

In our preliminary system-level evaluation, downlink transmissions can reach 165 Mb/s at 75 m using simple BPSK modulation with a 1/8 of the bandwidth of the IEEE 802.11ad standard. At shorter distances, the modulation order or bandwidth can be traded off for higher data rates. In the uplink, the BPSK transmissions range can reach up to 25 m.

### Related Publications:

- [1] C. Dehos, J.L. González, A. De Domenico, D. Kténas, L. Dussopt, "Millimeter-wave access and backhauling: the solution to the exponential data traffic increase in 5G mobile communications systems?," *IEEE Communications Magazine*, vol. 52, no. 9, pp. 88-95, Sept. 2014.
- [2] R.J. Weiler, M. Peter, W. Keusgen, E. Calvanese-Strinati, A. De Domenico, I. Filippini, A. Capone, I. Siaud, A-M. Ulmer-Moll, A. Maltsev, T. Hausteiner, K. Sakaguchi, "Enabling 5G backhaul and access with millimeter-waves," *2014 European Conference on Networks and Communications (EuCNC)*, Bologna, Italy, 23-26 June 2014.



## On the impact of backhaul network on distributed cloud computing

Research topics: mobile communications, small cell cloud computing

J. Oueis, E. Calvanese Strinati, A. De Domenico, S. Barbarossa

**ABSTRACT:** Within the cloud computing paradigm, small cells are federated in computation clusters. However, effective cooperation among geographically neighboring small cells is prone to backhauling energy costs and delay limitations. This paper is a framework for evaluating backhauling performance in small-cell cloud architecture. We consider several backhaul technologies and topologies. Our simulations explicit the limitations of clustering in small cell cloud imposed by backhauling.

In small-cell (SC) cloud, small cells cooperate through cluster formation and cooperate for communication and energetic purposes, as well as for pooling computational resources. In fact, the small cloud network boosts the computational capacity of mobile terminals, and its proximity to users' equipment reduces the end-to-end service latency. To enhance the computation and storage capacities, SCs are backhauled together and exchange data. The choice of the small clusters depends on multiple constraints. Backhaul characteristics, technology, and topology play an important role in cluster formation. In this work, we study and evaluate the different trade-offs of base station clustering in a SC cloud network. We focus on the backhaul influence on cluster size and characteristics in terms of latency and power consumption. Several backhaul technologies and topologies are compared in the investigations.

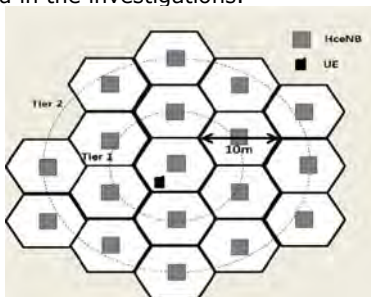


Figure 1: Cellular deployment of small cells.

As a system model, we consider a cellular deployment model of hexagonal compartments of 5 m radius each (Fig. 1). A mobile user, at a distance  $d$  from its serving SC, requests a computation offloading task that consists of computing  $W$  instructions in  $L_{app}$  seconds. The number  $N$  of SC in the cluster should be set in order to satisfy the following constraint:

$$N = \left\lceil n \in \mathbb{N} / \Delta_{cluster}(n) \leq L_{app} - \frac{N_{UL}}{R_{UL}} - \frac{N_{DL}}{R_{DL}} \right\rceil$$

where  $\Delta_{cluster}$  is the experienced latency and the last two terms account for uplink and downlink transmission times, respectively. The cluster latency is modeled for ring, tree, and full mesh topologies and can be minimized by an appropriate distribution of the computation load.

In a second step, we also model the communication power consumption of the SC computing cluster. This consumption depends on  $N$ , the backhaul technology, and the backhaul topology [1]. We consider three backhaul topologies: ring, star, and full mesh, and three technologies: optical fiber,

microwave and OTA LTE. We consider equal load distribution among the SCs in the cluster and we compare different backhaul characteristics in terms of latency and power consumption (Fig. 2, 3, Table 1).

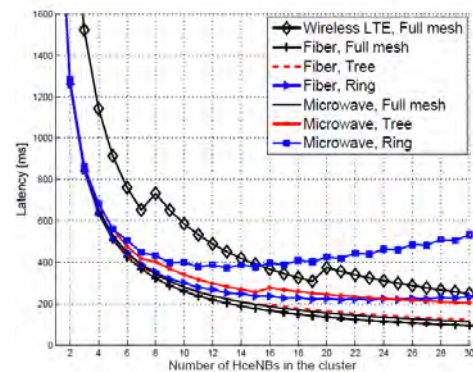


Figure 2: Cluster backhaul latency for various backhauls.

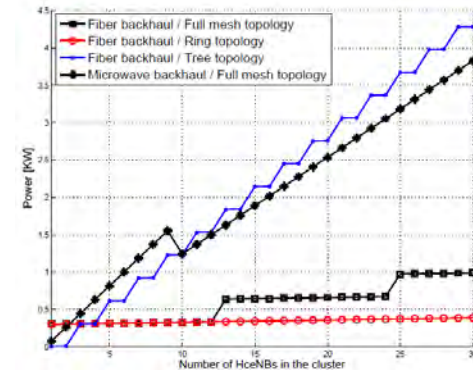


Figure 3: Cluster backhaul power consumption for various backhauls.

Criterion	Wireless LTE	Fiber	Microwave
Load dependent latency	Yes	No	No
Load dependent power consumption	Yes	No	Yes
Topology with lowest latency	Full mesh	Full mesh	Full mesh
Topology with lowest power consumption	Full mesh	Ring	Full mesh
Latency classification	*	***	**
Power consumption classification	*	***	**

Table 1: Comparison of backhaul technologies.

In summary, this work investigates the impact of backhaul on cooperative clusters of SCs and provides a preliminary vision on the SC cluster backhaul. The full detailed study and power and latency models are reported in [2].

### Related Publications:

- [1] P. Monti, S. Tombaz, L. Wosinska, J. Zander, "Mobile backhaul in heterogeneous network deployments: technology options and power consumption," *14<sup>th</sup> Int. Conf. on Transparent Optical Networks (ICTON)*, Coventry, England, 2-5 July 2012.
- [2] J. Oueis, E. Calvanese-Strinati, A. De Domenico, S. Barbarossa, "On the impact of backhaul network on distributed cloud computing," *2014 IEEE Wireless Communications and Networking Conference Workshops (WCNCW)*, pp. 12-17, Istanbul, Turkey, 6-9 April 2014.

## Multi-parameter decision algorithm for mobile computation offloading

**Research topics: mobile communications, small cell cloud computing**

**J. Oueis, E. Calvanese Strinati, S. Barbarossa**

**ABSTRACT: A novel offloading algorithm that takes decision about offloading mobile computation to a cloud of connected small cells is presented. The proposed algorithm incorporates a multitude of parameters in the decision process while reducing the mobile handset energy consumption and keeping a good user quality of experience. Simulations show that our proposed algorithm is able to extend the mobile battery life and ensure the computation of all the applications while respecting latency and memory constraints.**

Mobile devices paradigm has been reversed from communication to computing. Mobile handsets battery life is today limited by computation energy consumption requirements. Handing the computation to the cloud via mobile computation offloading is an emerging solution to limit computation energy consumption while accessing greater computation capacity. Nevertheless, computation offloading comes at the expense of generating extra communication traffic. Therefore, a decision process is needed for deciding between mobile computation offloading and local computation at the mobile handset. This decision depends on a large set of parameters such as, for example, energy consumption, memory, latency constraints, and available computational resources. Incorporating a larger number of parameters into the decision process increases the complexity of computing an optimal decision. Traditional mobile computation offloading algorithms are based on the sole energy consumption comparison between local computation and computation offloading.

We proposed a sequential algorithm where offloading decisions are made according to a decision tree and based on a multi-parameters optimization with a multi-fold task classification. The novelty of this work is twofold. First, the offloading decision process complexity is reduced while dependency on a variety of parameters is considered through successive and nested tasks classifications. Second, mobile energy consumption is reduced by offloading tasks depending on time criticality, handset available resources, and channel conditions. The algorithm can be described by five successive steps (Fig. 1):

1. Classify tasks as offloadable (Off) and not offloadable (NOff) according to technical and hardware requirements.
2. Classify Off and NOff tasks according to the time urgency of the tasks to compute. A task is tagged as urgent (OffUrg, NOffUrg) if more than a certain percentage of latency limits of the tasks have passed, and non-urgent (OffNUrg, NOffNUrg) otherwise.
3. OffUrg tasks needing more computation, memory, and energy than available at the mobile handset are offloaded and tagged as SOffUrg and others are tagged as COffUrg.
4. COffUrg tasks are offloaded or computed locally depending on the strategy that consumes less energy.
5. Non-urgent offloadable tasks (OffNUrg) are only offloaded if the channel conditions are better than the average previous channel conditions. Non-urgent non-offloadable tasks are then computed locally, if any local resources are available.

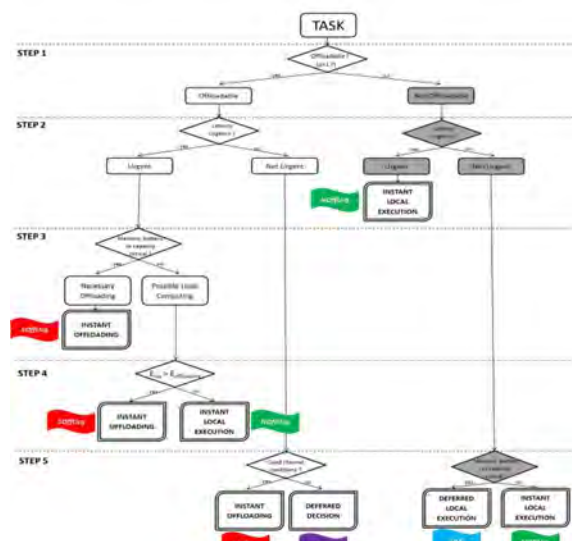


Figure 1: Classification steps of the proposed algorithm.

The efficiency of the proposed algorithm considering a scenario of tasks offloading to a serving small cell through a Rayleigh channel is investigated by evaluating the mobile handset battery discharge in case of random computation load and using the power consumption model from A.R. Jensen *et al.* (2012). The proposed algorithm is compared to the cases where no offloading is done, offloading decision is only based on energy consumption and total offloading. Simulation results showed that it achieves the best performance and can extend battery life up to x1.45 times even in random scenarios.

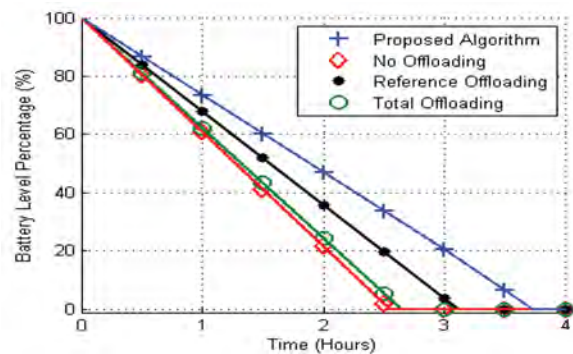


Figure 2: Mobile battery discharge due to tasks offloading.

**Related Publications:**

[1] J. Oueis, E. Calvanese-Strinati, S. Barbarossa, "Multi-parameter decision algorithm for mobile computation offloading," 2014 IEEE Wireless Communications and Networking Conference (WCNC), Istanbul, Turkey, 6-9 April 2014.

## Multiband CSMA/CA with RTS/CTS for M2M Communications

Research topics: machine-to-machine communications, random access protocols

B. Mawlawi, J-B. Doré

**ABSTRACT:** Machine to machine communications based on cellular networks are severely disrupted when an extremely large number of devices in the service coverage is considered. Collisions between the senders due to the large number of devices lead to communication problems. For that purpose, we proposed an opportunistic MAC based on multiband CSMA/CA with RTS/CTS technique and proved that an important gain can be achieved in terms of system performance particularly when the network is heavily loaded.

The emergence of machine-to-machine communications associated with their sporadic access has led to reconsider contention-based access algorithms. A new protocol called multiband CSMA/CA with RTS/CTS is proposed. This protocol is designed to operate in an environment with any number of devices (large or small), operates in distributed manner and is simple to deploy as it doesn't require much planning, interoperability or management [1].

The newly proposed protocol [2] is designed to avoid collisions between multiple users (source nodes) which are willing to access at the same time to a common access point (destination node). A single channel is divided into  $N$  sub-channels during RTS transmission (Figure 1). Because the RTS channel is divided into multiple sub-channels, the required time duration of the RTS message will be multiplied by the number of sub-channels ( $N$ ). A source node willing to transmit data should first listen to all sub-channels simultaneously.

If a signal is detected on one sub-channel, the channel is declared busy. Then, a waiting period (expressed in number of time slots) represented by a "backoff counter" is chosen randomly in the interval  $[0, CW-1]$ , where  $CW$  is called the contention window. The backoff counter is decremented each time the channel is detected to be available for a DIFS (Distributed Inter-Frame Space) duration. The wait counter freezes when the channel is busy, and resumes when the channel is available again for at least DIFS time. When the backoff counter reaches zero, the source randomly chooses one sub-channel over the  $N$  available sub-channels to send a request permission message (RTS "Request To Send") to the destination node. It waits for receiving an authorization message (CTS "Clear To Send") from the destination node (access point) before transmitting data. The access point (AP) listens simultaneously to sub-channels. If one or more RTS is detected, the AP broadcasts CTS over all the sub-channels indicating the authorized station to communicate. The chosen station sends its data and waits for Acknowledge (ACK) from the AP. Both data and ACK messages are sent over all the sub-channels. Upon receipt of all transmitted data (successful transmission), and immediately, after a SIFS (Short Inter-Frame Space) duration, the destination node sends an ACK (for "Acknowledgment").

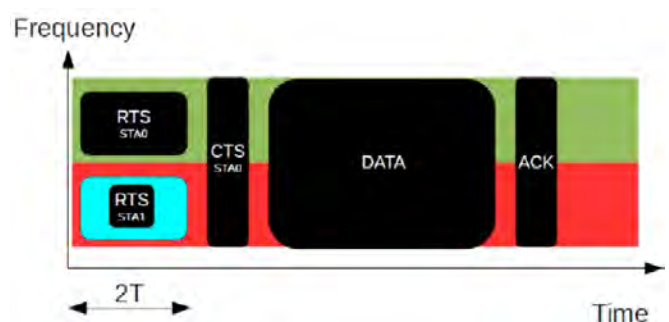


Figure 1: Multiband CSMA/CA - RTS/CTS scenario.

We demonstrated that the saturation throughput is improved using the proposed protocol [3]. It may be interesting to divide the RTS band into multiple bands when the number of users is larger than 10 (Figure 2). This improvement is due to the reduction of the RTS collision probability which becomes significant when the number of users becomes large.

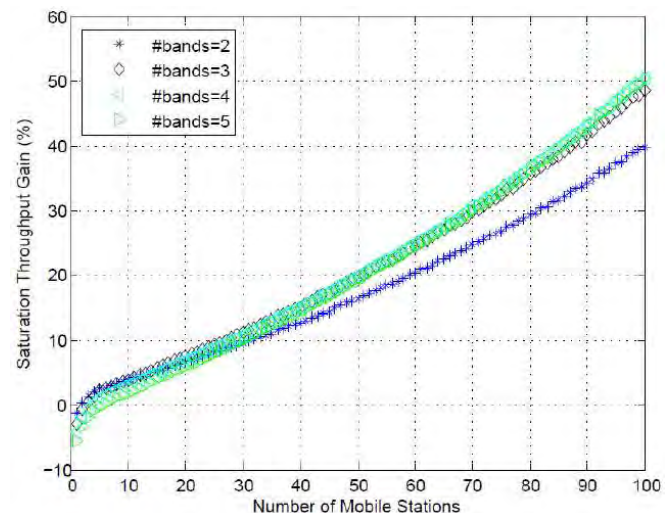


Figure 2: Saturation throughput gain (%) vs. number of stations for various number of RTS bands.

#### Related Publications:

- [1] B. Mawlawi, J.B. Doré, N. Lebedev and JM Gorce, "Multiband CSMA/CA with RTS-CTS strategy," *IEEE 10<sup>th</sup> Int. Conf. on Wireless and Mobile Computing, Networking and Communications (WiMob)*, Larnaca, Cyprus, 8-10 Oct. 2014.
- [2] B. Mawlawi, J.B. Doré, N. Lebedev and JM Gorce, "Analysis of frequency channel division strategy for CSMA/CA with RTS/CTS mechanism," *8<sup>th</sup> Int. Conf. on Sensing Technology (ICST)*, Liverpool, UK, 2-5 Sept. 2014.
- [3] B. Mawlawi, J.B. Doré, N. Lebedev and JM Gorce, "Performance evaluation of Multiband CSMA/CA with RTS/CTS for M2M communication with finite retransmission strategy," *Int. Conf. on Selected Topics in Mobile and Wireless Networking (MoWNet)*, Rome, Italy, 8-9 Sept. 2014.



## Analysis and design of LDPC decoders running on faulty devices

Research topics: mobile communications, error correcting codes

C. L. Kameni Ngassa, V. Savin

**ABSTRACT:** In this work, we investigated the behavior of LDPC decoders running on faulty logic devices in order to evaluate their robustness in the presence of errors induced in the processing units. The main objectives were (1) to develop a theoretical framework that allows understanding the limits of iterative LDPC decoding with faulty hardware, (2) to assess the error correction performance of practical LDPC codes under faulty hardware, and (3) to identify practical solutions capable of increasing the decoder robustness to hardware noise.

Error correction decoders built out of unreliable components have attracted an increasing interest over the last few years, as reliability issues emerged as a primary concern for future generations of integrated circuits. In this work, we focus on the class of Low-Density Parity-Check (LDPC) codes, decoded with iterative message-passing (MP) decoders running on faulty hardware.

We first focus on the theoretical analysis and understanding of the faulty Min-Sum (MS) decoder, by using a Density Evolution (DE) approach [1][3]. To this end, we introduce a new transient error model and carry out the DE analysis of the finite-precision MS decoder, deriving the limits of iterative MS decoding with faulty hardware. To evaluate the robustness of the MS decoder, we determine the maximum values of the hardware noise parameters allowing the decoder to achieve a target bit error probability (Figure 1). We further reveal the existence of a specific threshold phenomenon, referred to as functional threshold, separating the region where high-reliability decoding is possible from that where it is not. It corresponds to a sharp change in the decoder's behavior, similar to the change that occurs around the threshold of the noiseless decoder.

Our study also focuses on means to improve the decoder reliability, by protecting critical bits of the finite-precision computation flow within the decoding process. To this end, we investigate sign-preserving error models for arithmetic operations (e.g. adders), or for larger processing units of the decoder (e.g. variable-node or check-node processing units). For such models, the sign of the operation (or processing unit) result is always computed accurately. The benefits of sign-preserving computational models are assessed through the DE analysis. Finally, we also highlight some peculiar and very intriguing behaviors of the MS decoder under noisy hardware: in some particular cases, the noise introduced by the device can help the MS decoder to escape from fixed points attractors, and may actually result into an increased correction capacity with respect to the noiseless decoder.

Additionally, the practical performance of MS, Self-Corrected MS (SCMS) and Stochastic decoders is verified through Monte-Carlo simulation in the non-asymptotic case [2]. Unlike MS-based decoders, for which the exchanged messages are represented by a number of bits with different significance, for the Stochastic decoder the information is represented by stochastic bit streams, consisting of bits with

similar significance. Stochastic computing is by its nature very random, since it represents continuous values by streams of random bits. Consequently, hardware-induced errors are expected to have a reduced impact on the decoder performance. Our results show that the SCMS and the Stochastic decoders are very robust to transient errors, providing nearly the same performance as their noiseless counterparts (Figure 2). These results also reveal the significant role that memory mechanisms (e.g. the self-correction rule within SCMS, or edge-memories within Stochastic decoder) play in increasing the robustness to hardware noise. Although such memory mechanisms are themselves faulty, they allow detecting or correcting a number of errors that largely surpass the number of errors induced by their implementing circuits.

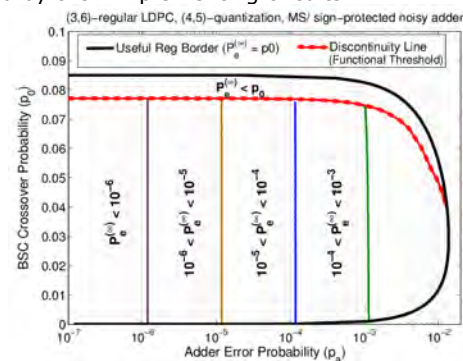


Figure 1: Useful and target-BER regions of the faulty MS decoder.

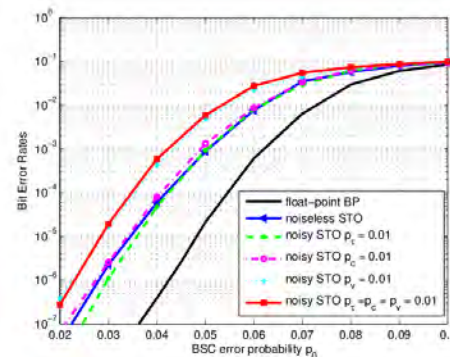


Figure 2: Bit error rate performance of the faulty Stochastic decoder.

### Related Publications:

- [1] C. L. Kameni Ngassa, V. Savin, and D. Declercq, "Unconventional Behavior of the Noisy Min-Sum Decoder over the Binary Symmetric Channel," *IEEE Information Theory and Applications Workshop (ITA)*, San Diego, CA, February 2014.
- [2] C. L. Kameni Ngassa, V. Savin, and D. Declercq, "Faulty Stochastic LDPC Decoders over the Binary Symmetric Channel," *IEEE Int. Symp. on Turbo Codes and Iterative Information Processing (ISTC)*, Bremen, Germany, August 2014.
- [3] C. L. Kameni Ngassa, V. Savin, E. Dupraz, D. Declercq, "Density Evolution and Functional Threshold for the Noisy Min-Sum Decoder," *accepted for publication in IEEE Trans. on Communications*, 2015.

## LDPC decoders: from algorithm to hardware implementation

Research topics: mobile communications, error correcting codes

V. Savin

**ABSTRACT:** Binary and non-binary LDPC decoders are widely used in practical applications. In this work, we investigated the hardware implementation of Min-Sum and Self-Corrected Min-Sum decoders and we proposed FPGA-based implementations featuring the following advantages: (1) efficient BRAM utilization, due to message packaging and compression, (2) reduced slice count due to the serial nature the processing, and (3) new approach for building the data path, which yields high working frequency.

It is widely recognized that one of the most significant contributions to coding theory is the invention of Low-Density Parity-Check (LDPC) codes by Gallager in the early 60's. But the outstanding success of these codes in providing practical constructions that closely approach the Shannon limit is rooted in the way there are decoded. Hence, rather than a family of codes, Gallager actually invented a new method of decoding linear codes, by using iterative Message-Passing (MP) decoders. In [1], we provide a thorough survey of LDPC decoders, with detailed insight into those most widely used in practical applications. The goal is to explain the whys and wherefores, while providing the reader with sufficient knowledge and details to allow implementing the presented decoders. Hence, we trace the evolution of LDPC decoding from Gallager's A, B, and probabilistic decoding to Belief-Propagation (BP), Generalized BP, Linear-Programming, Min-Sum (MS), MS-based, and stochastic decoding. We also address the case of non-binary LDPC decoding, for which we further present the Extended-MS and Min-Max (MM) decoding algorithms. Bibliographic references are also provided for the reader interested in deepening the understanding of specific topics discussed in the text.

Cost efficient FPGA implementations of MS and Self-Corrected-MS (SCMS) decoders for Quasi-Cyclic LDPC codes are investigated in [2], [3]. SCMS has shown to present quasi-optimal error-correction capability (very close to BP), while retaining the low complexity characteristic of the MS decoding. With respect to other MS-based decoders, like Normalized-MS and Offset-MS, the SCMS has been proven to provide better performance, especially in the error-floor region. The characteristic of the SCMS decoder is to erase (i.e. set to zero) any variable-node message that changes its sign with respect to the previous iteration. This comes with a price when implementing SCMS decoder architectures: the signs of variable node messages and the erasure bits have to be stored, thus increasing memory requirements. This also leads to additional overhead in terms of routing the messages to the appropriate processing units.

We address the problem of high memory overhead required by layered SCMS based decoders compared to conventional MS, by proposing two improvements. These require changes in the flow/rule of the conventional SCMS algorithm, in order to avoid storing the signs and the erasure bits of the variable node messages. Three layered LDPC decoders with serial a-posteriori log likelihood ratios (AP-LLR) processing are

implemented: conventional SCMS (SCMS-0), SCMS with no check node message signs storage (SCMS-1), and SCMS with neither check node message signs nor erasure bits storage (SCMS-2). FPGA implementation results for WiMAX (1152, 2304) code show that the third architecture has a resource utilization with 17% less with respect to the one implementing conventional SCMS, and with 11% less than the second architecture. Furthermore, it presents a similar cost to conventional MS, while having a 0.5 dB better error correction capability.

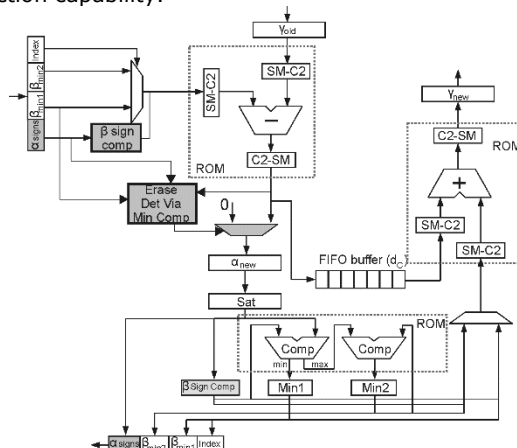


Figure 1: Variable and check node unit architecture for SCMS-2.

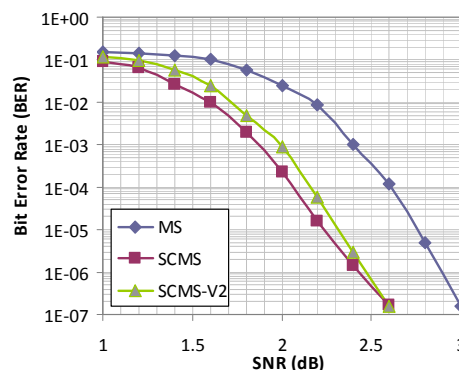


Figure 2: Bit error rate performance of MS and SCMS decoders.

### Related Publications:

- [1] V. Savin, "LDPC decoders", in "Channel coding: Theory, algorithms, and applications", D. Declercq, M. Fossorier, and E. Biglieri Ed., Academic Press Library in Mobile and Wireless Communications, Elsevier, June 2014.
- [2] O. Boncalo, A. Amaricai, A. Hera, and V. Savin, "Cost Efficient FPGA Layered LDPC Decoder with Serial AP-LLR Processing", *Int. Conf. on Field Programmable Logic and Applications (FPL)*, Munich, Germany, Sept. 2014.
- [3] O. Boncalo, A. Amaricai, and V. Savin, "Memory Efficient Implementation of Self-Corrected Min-Sum Decoder", *IEEE Int. Conf. on Electronics Circuits and Systems (ICECS)*, Marseille, France, Dec. 2014.

## System level evaluation of Filter Bank Multi-Carrier, a competitive waveform for the fifth generation of cellular communications

Research topics: mobile communications, new waveforms

N. Cassiau, D. Kténas

**ABSTRACT:** Particular challenges that need to be faced in 5G systems are fragmented spectrum and spectrum agility. It is unlikely that these challenges can be met using OFDM, therefore highly flexible and robust new waveforms are required. Filter Banks Multi-Carrier (FBMC) is one of these candidates. FBMC has been well studied on link level so far, however, simulations at system level are also needed to get further insight regarding the suitability of this particular waveforms for 5G systems and applications.

In [1] and [2], the performance of FBMC in a Multi-User Multiple Input Multiple Output (MU-MIMO) DownLink Cooperative MultiPoint (DL-CoMP) was assessed at the system level. The Signal on Interference plus Noise Ratio (SINR) measurement, which is usually applied in the evaluation of OFDMA systems, cannot capture the mutual dependencies between subcarriers of non-orthogonal multicarrier schemes. In our simulations, we used the SNIDR model, where the "D" stands for the residual distortion. The SNIDR on subcarrier  $k$  is defined as:

$$SNIDR_k = \frac{P_s}{P_i + P_n + P_d}$$

where  $P_s$ ,  $P_i$ , and  $P_n$  denote the signal power, interference power, and noise power, respectively. The residual distortion power  $P_d$  is:

$$P_d(k) = \frac{2P_s}{K^3} \left\| \frac{H'(w_k)}{H(w_k)} \right\|^2 C_f$$

with  $H(w_k)$  and  $H'(w_k)$  being the channel impulse response and its derivative, respectively, both evaluated at the  $k^{\text{th}}$  subcarrier,  $K$  the FBMC interleaving factor and  $C_f$  the first order derivative of the receiving prototype pulse.

The actual link-to-system interface is a mapping from an effective SNIDR to a corresponding packet error rate. This mapping has to be evaluated and fitted against measured packet error rates coming from link-level simulations in an equivalent AWGN channel. Figure 1 depicts the resulting curves generated with a link level simulator.

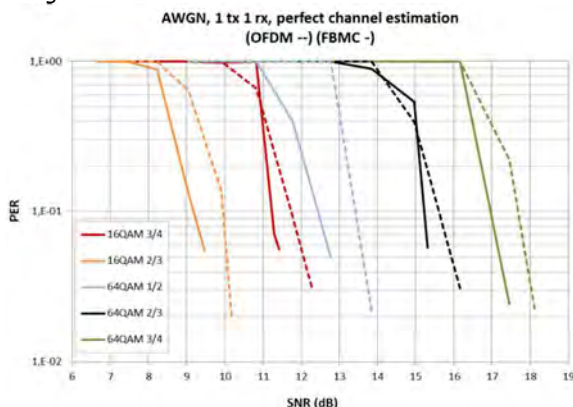


Figure 1: Packet Error Rate vs SNR in additive white Gaussian noise channel.

In this simulator, a convolutional encoder and Viterbi decoder was used. The gain in FBMC from abandoning the cyclic prefix can be clearly observed. Based on the generated results depicted in Figure 1, lookup tables were generated for usage in system level simulations.

We considered the following procedure for Channel State Information (CSI) feedback generation at the user side and corresponding scheduling at the base stations: for each Resource Block (RB), each user (UE) that is likely to be scheduled for MU transmission reports to the Base Stations (BS) the index of the precoder that maximizes its Signal on Interference Ratio (SIR) and a discretized value of this SIR. The BSs then choose the best pair of users on each RB.

The total throughput of the UEs vs. the feedback rate per UE is plotted in Figure 2 for two transmit antennas. It must be noted that FBMC outperforms OFDM. With a feedback rate of 20 kbps, FBMC UEs moving at 1 km/h allow a throughput of 24.7 Mbps whereas OFDM UEs only allow 23.6 Mbps. As intuitively expected, the speed of the UEs has a significant impact on the necessary amount of feedback: to ensure a throughput of 24.7 Mbps, 60 kbps are necessary at 3 km/h and more than 100 kbps at 10 km/h. Further, it can be observed, that the FBMC curves have a slope similar to the slope of the corresponding OFDM curves. Thus, FBMC shows a comparable robustness against limited feedback.

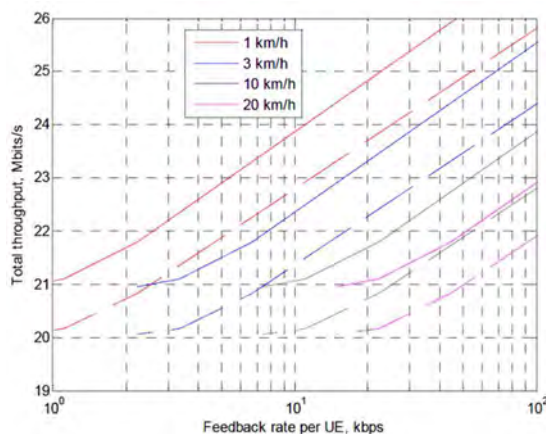


Figure 2: Total throughput as a function of the feedback rate. (OFDM: dashed lines, FBMC: continuous lines).

### Related Publications:

- [1] G. Wunder, M. Kasparick, S. Ten Brink, F. Schaich, T. Wild, Y. Chen, I. Gaspar, N. Michailow, G. Fettweis, D. Ktenas, N. Cassiau, M. Dryjanski, K. Sorokosz, S. Pietrzyk, and B. Eged, "System-level interfaces and performance evaluation methodology for 5G physical layer based on non-orthogonal waveforms," *2013 Asilomar Conference on Signals, Systems and Computers*, Pacific Grove, CA, 3-6 Nov. 2013.
- [2] N. Cassiau, D. Ktenas, G. Wunder, and M. Kasparick, "Feedback scaling for downlink comp with orthogonal and non-orthogonal waveforms," *2014 European Conference on Networks and Communications (EuCNC)*, Bologna, Italy, 23-26 June 2014.



## Capacity benefits of FBMC multiple access for relaxed synchronisation cellular networks

Research topics: mobile communications, new waveforms

J-B Doré, V. Berg, D. Noguét, D. Ktésas

**ABSTRACT:** Relaxed synchronization and access to fragmented spectrum are considered essential for future generations of wireless networks in order to reduce physical channel signaling. Frequency Division Multiple Access for Filter Bank Multicarrier (FBMC) modulation provides promising performance without strict synchronization requirements contrary to conventional Orthogonal Frequency Division Multiplexing (OFDM). The maximum achievable capacity of an asynchronous uplink transmission is analyzed when limited amount of feedback information on timing misalignment and power control is available.

Orthogonal Frequency Division Multiplexing (OFDM) has proven to be very effective for mobile wireless communications (WLAN, LTE). As the availability of large amount of contiguous spectrum is more and more difficult to guarantee, the aggregation of noncontiguous frequency bands is considered to reach higher data rates and/or improve access flexibility. This requirement of spectrum agility has encouraged the study for alternative multicarrier waveforms such as Filter Bank Multicarrier (FBMC).

Furthermore, sporadic access has been identified as another significant challenge faced by future mobile access networks. In order to reduce the battery power consumption, a mobile node may be configured to enter a dormant state as rapidly as possible after a data transaction. This is one of the root cause of significant signaling overhead on the cellular network. Every times a mobile node wakes-up from its dormant state to transmit information, a complete synchronization procedure is made between the node and the base station. Consequently, relaxed synchronization schemes have been considered to limit the amount of required signaling.

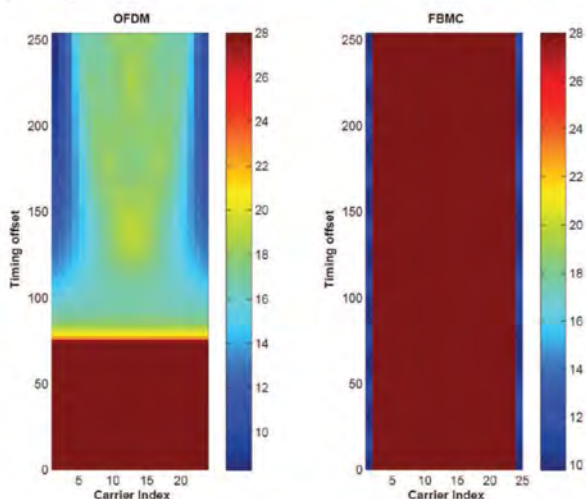


Figure 1: Signal to interference plus noise ratio in dB as a function of carrier index and timing offset for OFDM and FBMC waveforms.

The capacity of an uplink asynchronous transmission with limited feedback information has been compared between FBMC and OFDM [1]. Due to the fair frequency localization of FBMC, only the carriers located at the edges of the active spectrum are affected by interferences (Fig. 1), while interferences are spread over all the active carriers for OFDM.

FBMC waveforms allow for a simple way of sharing resources between cell-edge users without strict synchronization. This is a direct consequence of the low level of uplink interference generated by the built-in waveform filter of the FBMC prototype filter. We demonstrated the benefits of the FBMC waveform compared to the OFDM waveform in terms of capacity (Fig. 2), particularly for high order modulations [1] when limited amount of feedback information on timing misalignment and power control is available.

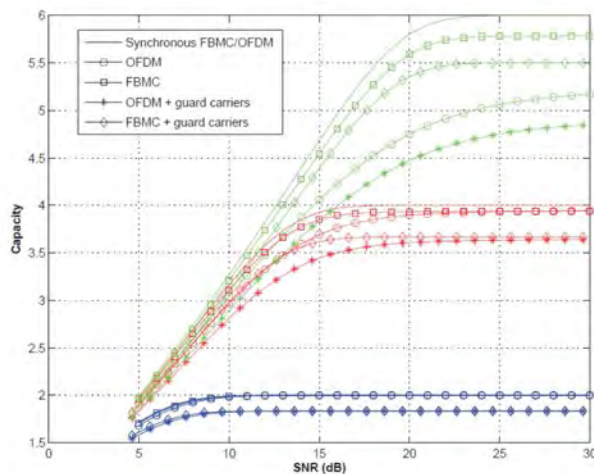


Figure 2: Capacity in bit/s/carrier for OFDM and FBMC waveforms. QPSK (blue), 16-QAM (red) and 64-QAM (green) modulations.

A frequency-domain receiver architecture combined with the high stop-band attenuation of the FBMC prototype filter provides a receiver architecture that allows for efficient multiuser asynchronous reception [2].

#### Related Publications:

- [1] J-B. Dore, V. Berg, and D. Ktésas, "Performance of FBMC Multiple Access for Relaxed Synchronization Cellular Networks," *Workshop on Broadband Wireless Access, IEEE Global Communications Conf. (Globecom)*, Austin, Tx, 8-12 Dec. 2014.
- [2] V. Berg, J-B. Dore, and D. Noguét, "A Multiuser FBMC Receiver Implementation for Asynchronous Frequency Division Multiple Access," *17th Euromicro Conference on Digital System Design (DSD)*, Verona, Italy, 27-29 Aug. 2014.

## Channel estimation techniques for 5G cellular networks

Research topics: mobile communications, channel estimation

J.-B Doré, V. Berg, D. Ktésas

**ABSTRACT:** In order to reduce the constant exchange of control signaling, relaxed synchronization is considered for the 5th generation of wireless cellular networks. This requirement combined with dynamic spectrum access has led to reconsider conventional orthogonal frequency division multiple access. Frequency division multiple access for filter bank multicarrier (FBMC) modulation has emerged as a serious contender for these asynchronous fragmented spectrum access scenarios. However, channel estimation has been only partially addressed in this context so far.

Single-carrier frequency division multiple access (SC-FDMA), which has been chosen for the uplink of the 3GPP long-term evolution (LTE), can be considered as an extension of orthogonal frequency division multiple access (OFDMA) designed to improve peak to average power ratio performance. This multiuser access technique provides flexible resource allocation and is spectrally efficient. However, frequency offsets between users should be strictly limited, and data signals should be synchronized at the receiver when considered in uplink mode. If not fulfilled, these synchronization requirements lead to inter-carrier and inter-symbol interferences, and performances are significantly degraded. To overcome these limitations, alternative multicarrier waveforms such as filter bank multicarrier (FBMC) have been considered for future cellular networks.

Channel estimation is an essential process before demodulation when the transmission channel is frequency selective. For multicarrier modulation systems, the estimation is usually performed by sending a training data sequence on a set of carrier frequencies known to the receiver.

Multicarrier symbols and adjacent carriers are non-orthogonal with FBMC, therefore the signal received from a known transmitted sequence contains interference from consecutive multicarrier symbols and adjacent carriers. As a result, classical estimation techniques used for OFDM cannot be simply applied and some adaptations should be made.

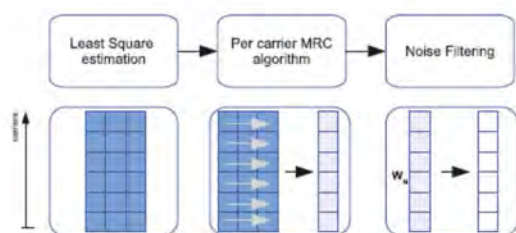


Figure 1: Schematic of the proposed algorithm for interference approximation method-based preamble.

A new channel estimation scheme has been proposed which combines flexibility for practical implementation and fair level

of performance [1]. The scheme estimates the channel on distributed pilot carriers and interpolates the channel over all the active carriers even when fragmented blocks of frequencies are considered.

A least-square estimate of the channel coefficients is computed after a carrier frequency offset phase correction on the received signal according to the location of the pilot symbol on the prototype filter. Then a maximum-ratio-combining algorithm is applied per carrier to mitigate the interference generated by the non-orthogonality of the carriers. Finally, an interpolation filter optimized to the expected channel statistics is applied (Fig 1).

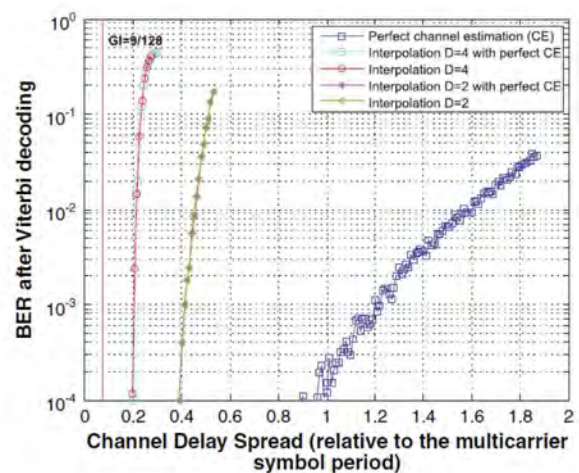


Figure 2: Performance of the proposed receiver as a function of the channel delay spread.

The structure easily scales when multiple users are considered. Besides, the proposed preamble is robust to channels exhibiting delay spread of almost 0.4, the multicarrier symbol duration. Using the LTE parameters, this corresponds to approximately 26.6  $\mu$ s and compares with the 4.69  $\mu$ s of the normal guard interval (Fig. 2). This suggests that the carrier spacing could be significantly reduced when FBMC is considered, giving this waveform a significant advantage for resilience to Doppler shift.

### Related Publications:

[1] J.-B. Dore, V. Berg, and D. Ktésas, "Channel estimation techniques for 5G cellular networks: FBMC and multiuser asynchronous fragmented spectrum scenario", *Transactions on Emerging Telecommunications Technologies*, vol. 26, no. 1, 2015, pp. 15-30.

## FBMC channel interpolation and equalization for multiuser asynchronous transmission on fragmented spectrum

Research topics: mobile communications, channel estimation

J.-B Doré, V. Berg, N. Cassiau, D. Ktésas

**ABSTRACT:** Relaxed synchronization and access to fragmented spectrum are considered for future generations of wireless networks. The architecture of a Filter Bank Multicarrier (FBMC) receiver suitable for this scenario is considered. Carrier frequency offset compensation is combined with inter-carrier interference cancellation and performs well under very large frequency offsets. Channel estimation and interpolation had to be adapted and proved effective even for heavily fragmented spectrum usage. Channel equalization can sustain large delay spread.

A flexible architecture for multiuser asynchronous reception on fragmented spectrum will be able to exploit the advantages of FBMC if the signal is efficiently demodulated in the frequency domain without a-priori knowledge of the FFT timing alignment (i.e. the location of the FFT block, this property is called asynchronous FFT).

A receiver architecture based on this assumption was studied [1]. Conventional equalization techniques for FBMC are not suitable for multiuser asynchronous reception. Good spectral containment introduced by the matched filter of the receiver helps to avoid distortion from non-synchronous adjacent users. Channel equalization may therefore be independently processed per user. A new frequency-spreading FBMC architecture should be considered: at the cost of a significantly larger FFT, equalization may be efficiently done using a one-tap complex coefficient per subcarrier (Fig 1).

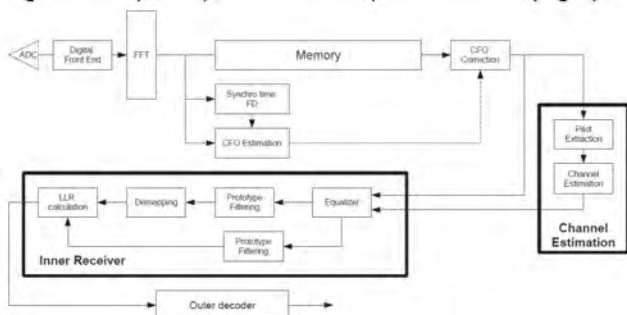


Figure 1: Block diagram of the proposed receiver.

The entire baseband signal processing functions may be implemented in the frequency domain and no strict synchronization requirement on the FFT, the first element of the receiver chain, is necessary.

Channel interpolation has to be carefully considered. As multiuser asynchronous Frequency Division Multiple Access generates heavily fragmented spectrum blocks, channel estimation should be further optimized for the edges of the

receiver active carrier bands than state-of-the-art systems. A performance improvement of up to 7 dB on the Mean Square Error (MSE) of the estimated channel is observed in the simulated scenarios [1] (Fig 2).

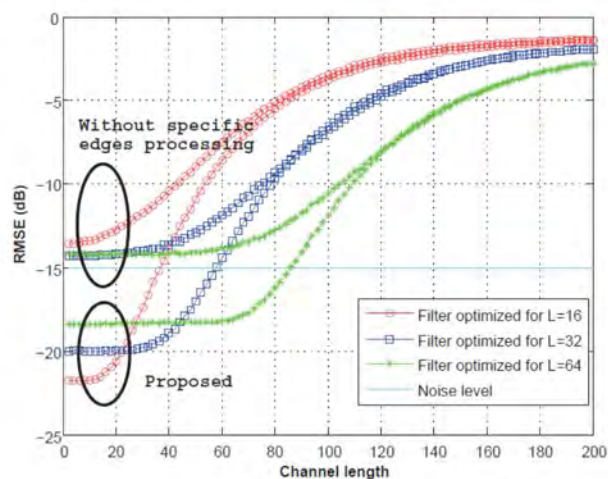


Figure 2: Mean Square Error versus channel delay spread for a SNR of 15 dB assuming 10 coefficients per filter. The filter blocks were designed for a channel delay spread of length 16/32 and 64 time domain samples.

The channel estimation combined with a new FS-FBMC equalization technique [2] is contained in complexity but achieves good performance for channels exhibiting large delay spread. As a comparison, using the 10-MHz LTE parameters, the receiver performs well for channels with delay spread of up to 8.3  $\mu$ s. This compares with standard LTE that has been designed for channels with delay spread of up to 4.7  $\mu$ s. Moreover, we have demonstrated that the proposed equalizer does not require FFT synchronization and is therefore adapted to asynchronous multiuser reception.

#### Related Publications:

- [1] J.-B. Dore, V. Berg, and D. Ktésas, "Spectrum Fragmentation and Efficient Channel Interpolation: Applications to FBMC," *20th European Wireless Conference*, 14-16 May 2014, Barcelona, Spain.
- [2] J.-B. Dore, V. Berg, N. Cassiau, and D. Ktésas, "FBMC receiver for multi-user asynchronous transmission on fragmented spectrum", *EURASIP Journal on Advances in Signal Processing*, 2014.



## A multiuser FBMC receiver hardware implementation for future 5G cellular communications

Research topics: mobile communications, digital hardware architectures

V. Berg, J. B. Doré, D. Noguet, N. Cassiau, D. Kténas

**ABSTRACT:** Relaxed synchronization is considered essential for future generations of wireless networks in order to reduce the signaling overhead. Filterbank Multicarrier (FBMC) modulation receivers may be implemented in the frequency domain as synchronization and equalization may be performed jointly. The FPGA implementation of a flexible multiuser FBMC receiver in this context is then described. Its complexity is finally analyzed. The proposed multiuser architecture complexity scales reasonably with the number of addressed users in parallel.

The generalization of smartphone usage has seen a significant increase of signaling due to sporadic data traffic. In order to save battery power, smartphones can disconnect from the network as soon as the state of the mobile phone is idle. Consequently, when the mobile phone restarts a data transaction, a complete resynchronization procedure is required. The growth of machine-type communications will further exacerbate the issue as machines rely on the same mechanism to save power. Consequently, relaxed synchronization schemes have been considered to limit the amount of signaling for these types of traffic. These requirements have led to study non-orthogonal multicarrier waveforms that provide an alternative to Orthogonal Frequency Division Multiplexing (OFDM) for future wireless networks. Amongst these non-orthogonal waveforms, Filterbank Multicarrier (FBMC) is considered as one of the most relevant approaches. A new FBMC receiver architecture called frequency spreading FBMC (FS-FBMC) has been studied. The results demonstrated that channel equalization and timing synchronization could be jointly processed without any requirement of time alignment of the FFT receiver [1].

A multiuser FBMC receiver architecture that does not require a-priori knowledge of the FFT timing alignment (i.e. the location of the FFT block, this property is called asynchronous FFT) is depicted in Figure 1. This receiver based on the FS-FBMC architecture has been implemented on a Xilinx Kintex-7 XC7K325T FPGA on the T-Flex platform [2]. Resource utilization on the T-Flex platform is given in Table 1 for a two user receiver.

Function	Resource Utilization			
	Slice Regs	LUTs	DSP48E1	RAM Blks
Digital Front End	11340	9041	46	0
FFT	6610	4481	19	35
Memory	594	628	2	100
FD Synchro.	10527	14437	60	6
Channel Est.	16125	12352	53	12
Channel Resp. Mem.	182	96	0	4
Inner Receiver	13195	11946	46	7
Outer Decoder	4878	10968	2	16
Control	35193	17210	0	3
<b>Total</b>	<b>98644</b>	<b>81159</b>	<b>228</b>	<b>183</b>

Table 1: Hardware resource utilization: multiuser FS-FBMC receiver.

The memory block accounts for more than half of the memory in the receiver design (55%) while the FFT is the second largest function in terms of memory requirement (15% of the memory). The blocks that are duplicated to be able to address more than one user at the same time (FD synchronization, channel response memory and outer decoder) only account for 16% of the slice registers, 31% of the LUTs and 14% of the memory blocks.

This shows that the receiver complexity smoothly scales with the number of users, as only a limited number of building blocks need to be duplicated when multi-user reception is considered. Therefore, the receiver can be easily extended to handle multiple users (e.g. in a cellular base station). Then, it can be concluded that the presented FS-FBMC architecture is a valid approach for asynchronous multiple access communications required by future 5G cellular systems.

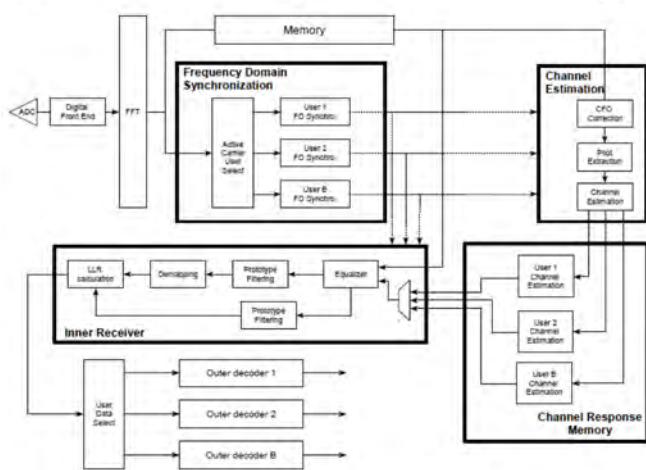


Figure 1: Block diagram of the proposed multiuser asynchronous receiver architecture.

### Related Publications:

- [1] J.-B. Doré, V. Berg, N. Cassiau, and D. Kténas, "FBMC receiver for multi-user asynchronous transmission on fragmented spectrum," *EURASIP Journal on Advances in Signal Processing*, Special Issue on Advances in Flexible Multicarrier Waveform for Future Wireless Communications, 2014:41.
- [2] V. Berg, J.-B. Dore, and D. Noguet, "A Multiuser FBMC Receiver Implementation for Asynchronous Frequency Division Multiple Access," *17th Euromicro Conference on Digital System Design (DSD)*, Verona, Italy, 27-29 Aug. 2014.

## A flexible radio receiver for TVWS based on FBMC

Research topics: mobile communications, digital hardware architectures

V. Berg, J. B. Doré, D. Noguet

**ABSTRACT:** Filterbank multicarrier modulation (FBMC) has been identified as a strong contender for dynamic spectrum access in the TV White Space, as FBMC transceivers are able to control out-of-band interference level without compromising their flexibility. The frequency spreading (FS-) FBMC receiver architecture performance and complexity are analyzed and compared with a polyphase network (PPN-) implementation of FBMC and with OFDM. It is shown that the implementation complexity overhead of FS-FBMC is limited when hardware resource sharing techniques are exploited.

In 2009, the US radio regulator authorized opportunistic unlicensed operation in the TV bands. Such systems have to coexist with TV broadcast signals and wireless microphones. In this context, co-channel communication is prohibited and adjacent channel leakage ratio (ACLR) is very limited in order to prevent an opportunistic system from interfering with an incumbent operating in an adjacent channel. From these requirements, it can be concluded that an opportunistic system must be agile in frequency and ACLR must be larger than 55 dB. The ACLR performance of the FBMC transmitter significantly outperforms the ACLR performance of the CP-OFDM such that the coexistence with incumbent TV signal is improved by an additional 9 dB with the FBMC modulator [1] in comparison to CP-OFDM.

Several architectures of FBMC receivers have been studied in the literature. The polyphase network (PPN-)FBMC architecture limits the complexity while the frequency spreading (FS-)FBMC considers reception in the frequency domain and seems more suited to the flexibility requirements of TVWS.

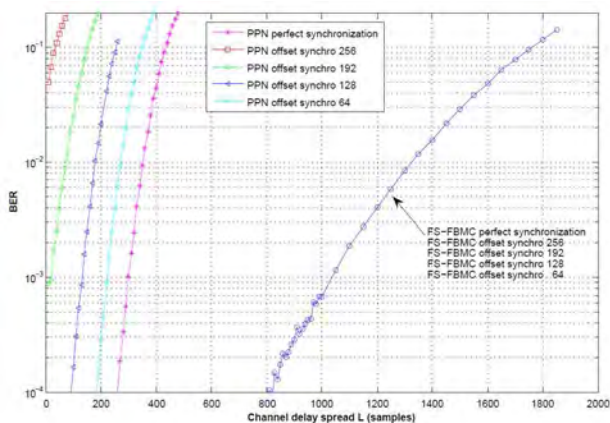


Figure 1: Performance comparison PPN-FBMC vs FS-FBMC.

The performances of both PPN- and FS-FBMC architectures against channel delay spread have been evaluated by simulation using a set of parameters derived from LTE [2].

The bit-error-rate (BER) performances have then been evaluated in the absence of thermal Gaussian noise assuming a perfect channel estimation. FS-FBMC performs on channels exhibiting much larger delay spread levels than PPN-FBMC. In the simulated scenario, the performance is available up to 18- $\mu$ s for PPN-FBMC and 65 $\mu$ s for FS-FBMC. Furthermore, when the FFT block at the receiver is not well aligned in the time domain, the performance of the PPN-FBMC receiver collapses while performance of the FS-FBMC remains unaffected [2] (Figure 1).

A flexible FBMC receiver based on the FS-FBMC architecture has been implemented on a Xilinx Kintex-7 XC7K325T FPGA on the T-Flex platform [1]. Resource usage of the FS-FBMC receiver is given in terms of Slice Registers (Slice Regs), Look-Up Tables (LUTs), DSP blocks (DSP48E1) and memory banks (RAM BLKs) used by the different blocks of the design and compared to an equivalent OFDM receiver.

Table 1 compares the resource utilization of FS-FBMC and OFDM receiver. In terms of digital logic, FBMC takes around 30% extra area in comparison to OFDM. However, memory usage is almost multiplied by a factor of 4. This is due to the fact that computational complexity was limited thanks to a resource sharing strategy, which comes at the cost of storage. However, it is worth mentioning that memory cost in submicron technology is limited and can be easily traded against the benefits of FBMC in terms of dynamic spectrum access flexibility.

Receiver Architecture	Resource utilization			
	Slice Regs	LUTs	DSP48E1	RAM BLKs
OFDM	42574	39600	97	49
FS-FBMC	54970	50096	155	171
<b>FS-FBMC / OFDM resource usage ratio</b>	1.29	1.27	1.60	3.49

Table 1: Hardware resource utilization: OFDM vs FS-FBMC Receiver.

FS-FBMC can withstand large channel delay spreads and is suitable for fragmented spectrum access. These scenarios have particular significance in the TVWS context.

#### Related Publications:

- [1] V. Berg, J. B. Doré, and D. Noguet, "A flexible radio transceiver for TVWS based on FBMC," *Elsevier journal on Microprocessors and Microsystems*, vol. 38, issue 8, Part A, Nov. 2014, pp. 743-753.
- [2] V. Berg, J.-B. Dore, and D. Noguet, "A flexible FS-FBMC receiver for dynamic access in the TVWS," *9th Int. Conf. on Cognitive Radio Oriented Wireless Networks and Communications (CROWNCOM 2014)*, Oulu, Finland, 2-4 June 2014.

## Wearable wideband exposimeter design for electromagnetic field exposure measurements

**Research topics: electromagnetic field exposure, flexible RF architectures**

**S. Bories, D. Dassonville**

**ABSTRACT:** A novel architecture is proposed for the design and implementation of a wideband RF exposimeter covering the telecommunication standard in the 700 MHz–6 GHz frequency band. The design consists of a tunable band-pass filter and Low Noise Amplifier associated with a simplified direct-down conversion receiver. Thanks to its reconfigurable RF architecture, flexibility and selectivity are the main advantages compared to existing products.

This study is carried out in collaboration with Satimo industries and TTI in the frame of the European FP7 project LEXNET (Low Exposure NETWORKS) [1]. One of the LEXNET objectives is to propose a methodology to assess the global exposure of a population in a given area from all the transmitting telecommunication standards. For that purpose, the down-link exposure statistics are measured by deploying wearable RF exposimeters.

The proposed system outperforms existing products (exposimeter and smartphone application) performances (isotropy, sensitivity, frequency selectivity) while targeting lower cost than typical laboratory EMF instrumentation (spectrum analyzer). Main specifications are reminded in Table 1. The two main specificities of the proposed instrument are its flexibility and selectivity. The former is provided by the reconfigurable RF architecture, which can be reconfigured through software to address future bands. The frequency selectivity delivered by the direct conversion receiver allows to distinguish the different service providers. This latter feature is essential for coupling the measurements with network simulations. Moreover, a correction scheme is also demonstrated to statistically compensate human body impact on EMF measurements [3].

The tunable band pass filter is detailed hereafter. This pre-selection filter is used to reject spurious signals and relax constraints on the direct conversion receiver. It splits the total band into four sub-bands, which results in a trade-off between the number of filters, tuning range and flexibility (Fig. 2). The tuning filters are implemented on the two first bands F1 (791 to 960 MHz (tuning ratio 1.2)) and F2 (1710 to 2690 MHz (tuning ratio 1.6)). The two last bands are covered by fixed filters for F3 (Wimax 3.5GHz) and F4 (Wifi 5.5 GHz). The F1 tunable filter topology is an L coupled shunt resonator with an order 2.

The tunable filters use digital tunable capacitors (DTC) as the tunable element. These give a better linearity performance than traditional varactor diodes.

Each resonator is composed of: a fixed inductor (discrete type), a fixed capacitor and a DTC in parallel. Most of the insertion loss is caused by the parasitic of the DTC.

Figure 3 shows the measurement results for most significant states of the tunable filter from 806 MHz to 5.490 MHz center frequency. A complete integration of the wearable RF exposimeter is planned for the year 2015. This work is partially funded by the EC in the FP7 LEXNET project.

Characteristics	Description
Measurement capabilities	Measurement differentiation by application (GSM, DCS, UMTS, LTE, WiFi etc.) and also by service provider
User profile	Service providers / operators
Frequency bands	Research organizations/Regulatory bodies
Polarization	0.7 GHz – 6 GHz
Interface	Tri axial probes
Probe sensitivity	Bluetooth / USB
Dynamic range	5 mV/m
Dimensions	60 dB (5 mV/m to 5 V/m)
Weight	Smartphone form factor
	< 400 g

Table 1: LEXNET wearable RF exposimeter main specifications.

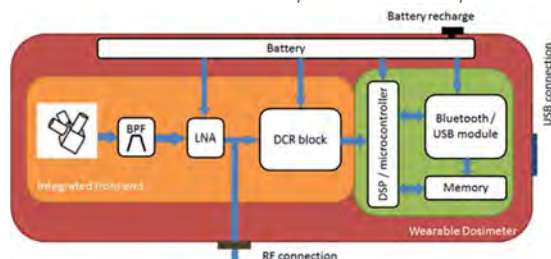


Figure 1: LEXNET RF exposimeter block diagram.

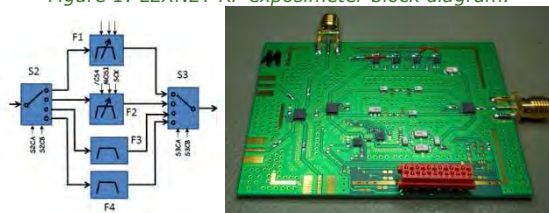


Figure 2: Reconfigurable pre-filter scheme and prototype.

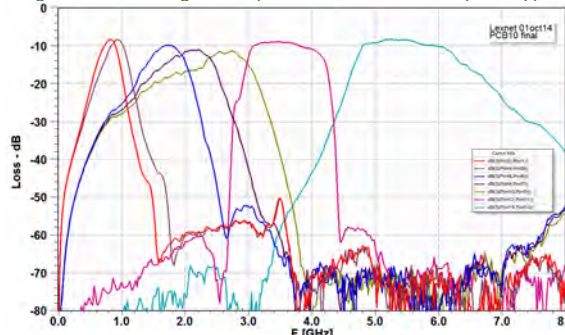


Figure 3: Measurement results of the tunable filter alone.

**Related Publications:**

- [1] M. Tesanovic, E. Conil, A. De Domenico, R. Agüero, F. Freudenstein, L. M. Correia, S. Bories, L. Martens, P. W. Wiedemann, and J. Wiart "Wireless networks and EMF—paving the way for low-EMF networks of the future: the LEXNET project," *IEEE Vehicular Tech. Magazine*, vol. 9, no. 2, Jun. 2014.
- [2] M.S. Anwar, Y. Toutain, A. Sanchez, D. Dassonville, Y. Fernandez, and S. Bories, "Wearable wideband exposimeter EM field exposimeter for electromagnetic field mobile communications", *44th European Microwave Conference (EuMC)*, Rome, Italy, 6-9 Oct. 2014, pp. 703-706.
- [3] LEXNET project public deliverable D3.2, "Wideband dosimeter design study & performances characterization, Release 2", 2014.



## Super directive antennas for low electromagnetic field mobile communications

Research topics: electromagnetic field exposure, miniature antennas

A. Clemente, A. De Domenico, S. Bories, C. Delaveaud, D. Ktésas

**ABSTRACT:** This paper investigates the electromagnetic field (EMF) exposure in heterogeneous cellular networks, where clusters of small cells are deployed to create local hotspots inside the macro cell. In this work, we propose to integrate small cells equipped with directive and compact antennas to reduce the required uplink power transmission at end users and to limit the associated EMF exposure. A preliminary performance evaluation quantifies the benefits of our solution.

Dense deployment of small cells is one of the main topics of investigation in 3GPP LTE release 12, which aims to meet the ever-increasing data rate requirements of future generations of wireless communications. In this Heterogeneous Network (HetNet) architecture, classical Macro base stations (MeNBs) are complemented with low-power low-cost small cell eNBs (SCeNBs) to extend the cellular network coverage (both in indoor and outdoor environment) and improve the performance experienced at end users by shortening the distance between user equipments (UEs) and access nodes. Nevertheless, the density of deployed small cells and their proximity to users reinforce the public concern about Electromagnetic Field (EMF) exposure.

Classical antenna solutions with beam-forming capabilities, implemented at the MeNB, cannot be integrated at small cell level due to the size constraints. In this paper, we investigate HetNet operating at 2 GHz, and we propose the use of super directive compact parasitic antenna array with real-time beam-steering capability in small cells to enable low EMF wireless communications [1]. In order to assess the impact of the EMF radiation in HetNets, we use a simplified version of the Exposure Index (EI) metric presented in [2]. In our analysis, four different antenna radiation patterns have been considered: i) the omnidirectional pattern with 5 dBi of directivity, ii) the 10-dBi directivity ideal pattern with 100% of efficiency (gain 10 dBi), iii) the 10-dBi directivity ideal pattern with 15% of efficiency (Gain 2 dBi), and iv) the radiation pattern obtained by full-wave electromagnetic simulation of the three-dipole super-directive compact antenna arrays optimized at 2 GHz [1] (directivity 9.1 dBi, gain -2.46 dBi). In this preliminary investigation, we assumed that our antennas could steer the beam in any possible direction with the same maximum gain. The proposed solution offers two major advantages as compared to the classical approach. First, in the downlink, the narrower beam avoids illuminating people that are not located in the considered angular sector. Second, in the uplink, the proposed solution can be used to mitigate the inter-cells interference as in the case of digital beam-forming. It is important to notice, that, due to low antenna efficiency (which results in low antenna gain), this solution is not relevant in the case of MeNBs.

The performance evaluation of electrically-small super-directive antennas only focuses on the uplink analysis since the major contribution to EMF exposure is due to transmission

originated at the UEs. Our approach consists in keeping the same QoS as a classical network architecture while reducing the UE transmitted power level thanks to the higher antenna angular selectivity. This power reduction will lead to an efficient decrease of the electromagnetic exposure experienced by end-users.

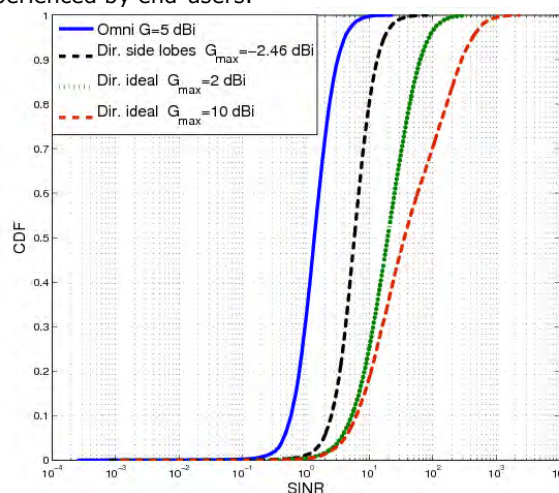


Figure 1: Cumulative distribution functions of the average uplink SINR at small cells with respect to different antenna patterns and a REB equals to 3dBi.

Our system level simulations of SCeNBs deployment show that the small cells achieve a 25x gain factor and 13x gain factor with respect to the standard omnidirectional antennas when using ideal directive antennas with  $G_{max}$  equals to 10dBi and 2dBi, respectively. Finally, when considering realistic directive antennas, most of the interference is only mitigated and not completely cancelled at the receiver. However, this solution achieves notable improvements with respect to the classic omnidirectional antenna and lead to a 3.3x factor gain.

It is important to note that the investigated antenna patterns do not directly limit the EMF exposure at the end user; nevertheless, the improvements in terms of SINR may enable a straightforward reduction of the uplink power required to operate at the target QoS. Therefore, HetNets with range-expanded small cells equipped with directive antennas may enable high data rate low EMF wireless communications.

### Related Publications:

- [1] A. Clemente, M. Pigeon, L. Rudant, and C. Delaveaud, "Super directive compact antenna design using spherical wave expansion," *IEEE International Symposium on Antenna and Propag. (APS-URSI)*, Memphis, TE, 6-11 July 2014.
- [2] M. Tesanovic, E. Conil, A. De Domenico, R. Agüero, F. Freudenstein, L. M. Correia, S. Bories, L. Martens, P. W. Wiedemann, and J. Wiart "Wireless networks and EMF—paving the way for low-EMF networks of the future: the LEXNET project," *IEEE Vehicular Tech. Magazine*, vol. 9, no. 2, June 2014.
- [3] A. Clemente, A. De Domenico, S. Bories, C. Delaveaud, and D. Ktésas, "Super directive antennas for low electromagnetic field mobile communications," *11th Int. Symp. on Wireless Communication Systems (ISWCS)*, Barcelona, Spain, 26-29 Aug. 2014.





# ②

# Wireless short-range communications

*Visible Light Communications*

*Wireless Body Area Networks*

*Secure wireless communications*

*Secure devices*

## High data rate LiFi product integration

**Research topics: smart lighting, optical wireless communication**

**L. Maret, D. Kténas, A. Lagrange, X. Popon, M. Laugeois, D. Miras, V. Berg**

**ABSTRACT: CEA-Leti reached a new step towards LiFi innovative technology transfer into an integrated commercial product. In collaboration with the French start-up LUCIOM, the previous LiFi prototype has been optimized in terms of cost, energy consumption and performance. A new waveform and PHY layer were designed, with a complete IP bidirectional optical link, using infrared spectrum for the upstream. Next steps will be the form factor reduction into a USB dongle and the multi-user access feature.**

LiFi, for Light Fidelity - aka Visible Light Communications (VLC) -, is getting a huge and recent interest since LED technology will become dominant in the lighting market in the coming years. LED lamps can be used as a network of access points for high data rate indoor mobile wireless communications [1]. They can be modulated at very high frequencies, above human visual persistence, and offer many advantages: new available bandwidth to face the conventional RF spectrum congestion, safe wireless communications without any EMF exposure issue, robustness to EMI (e.g. aeronautics, hospitals, nuclear areas), security, etc.

With expertise in both digital communications and solid state lighting, CEA-Leti developed in 2013 one of the first real-time LiFi hardware prototype, shown at the Consumer Electronics Show (CES 2014, Las Vegas (NE)) (Fig. 1) [2].

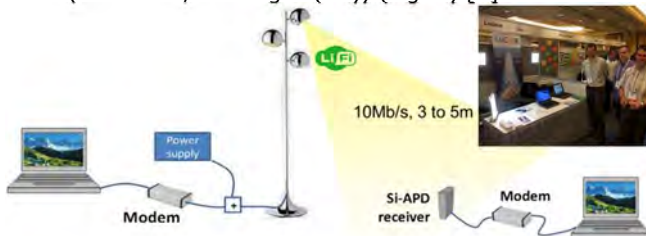


Figure 1: First CEA-Leti high data rate LiFi prototype at CES 2014.

This prototype was offering a 10 Mb/s IP link at a range of 3 meters, with good mobility but no optical uplink since either Ethernet or WiFi were used for the reverse link. Also, it was based on expensive components such as avalanche photodiodes and a hardware digital platform with a high-end FPGA.

In 2014, CEA-Leti started a collaboration with the French LiFi startup LUCIOM in order to go further into the integration of this prototype, towards a cost-efficient and smaller product. Objectives in 2014 were to reduce drastically the Bill-of-Material for a competitive product, to enhance performances while using cheaper components, to reduce the energy consumption for compatibility with a USB power supply and to integrate an infrared uplink for a 100% optical system.

The optimized PHY layer based on OFDM was investigated and the embedded software has been designed, so that all objectives have been reached in time, and different luminaires can be supported (Fig. 2). The performances of the prototype exhibit achieved bit rates versus the distance up to 30 Mbps.

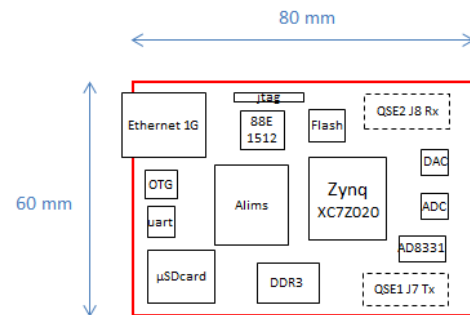


Figure 2: Schematic of the USB LiFi dongle targeted for 2015.

The next objective is to provide a small device to be plugged to any portable device in order to enable a new high data rate indoor wireless access system using the lighting network (Fig. 3). The final step will be the introduction of multi-user functionalities by supporting several devices under the coverage of a single lighting point.

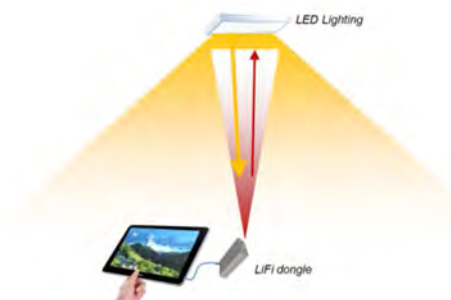


Figure 3: A possible Internet wireless indoor access scenario.

**Related Publications:**

- [1] A. Lagrange, and L. Maret, "From indoor GPS to high speed internet: Light becomes a communications medium", *Smart Lighting*, Barcelona, Spain, 7-8 May 2014.
- [2] <http://www-leti.cea.fr/en/Latest-news/Leti-Startups-Demonstrate-Innovative-Products-at-CES-2014>.



## Research trends in Wireless Body Area Networks from on-body to body-to-body cooperation

Research topics: Body Area Networks, Channel Models, MAC protocol

M. Maman, B. Denis, R. D'Errico

**ABSTRACT:** BAN researches include a wide range of multidisciplinary topics like antennas and propagation close to the body, Medium Access Control and networking protocols, security and localization. Short-term solutions for BANs so far were based on already existing communication standards, but they partially meet the specific needs and hardly communicate with the outside world. In this work, we presented possible BAN extensions from On-Body to Body-to-Body cooperative networks at different levels: propagation, protocols and wireless localization.

Body Area Networks (BANs) have recently emerged as a key enabling technology for many applications, including critical and rescue operations, remote monitoring, mobile healthcare, sports and entertainment. In these applications, mobile-to-mobile cooperation in BAN can be beneficial, either within one single network (i.e. On-Body cooperation), between distinct networks at reasonably short ranges (i.e. Body-to-Body cooperation), or with respect to fixed elements of infrastructure (i.e. Off-Body cooperation) (Fig. 1). Whereas most of research works have focused on close-to-the-body communications (e.g. IEEE 802.15.6 task group), new requirements imposed by coexistence and collective mobility suggest the exploitation of Body-to-Body cooperation.

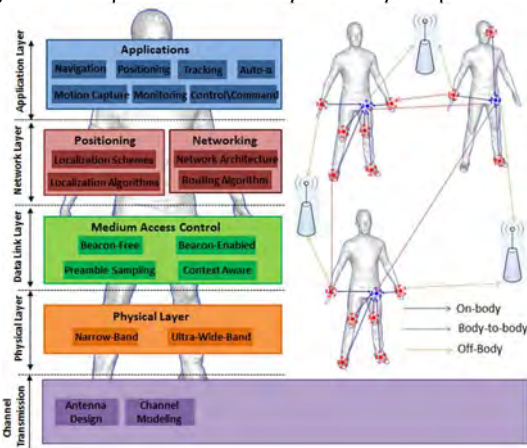


Figure 1: From Body Area Networks to Body-to-Body networks.

Human mobility, antenna locations and population variability have a strong impact on channel characteristics, which can be investigated with a scenario-based approach considering specific TX and RX antenna locations on the body, an environment and particular human body mobility conditions. The shadowing effects result into a long-term fading component according to the antenna location and mobility, while diffractions and reflections on the body or from the surrounding environment cause a short-term fading. With respect to the On-Body channel, Body-to-Body and Off-Body channels have been less investigated. Their mean channel gain is strictly related to the specific node location and the antenna type. In particular, normally-polarized antennas yield to higher channel gain than tangentially-polarized antennas in Non-Line of Sight (NLOS) scenarios because of the higher diffraction around the body (Fig. 2).

To cope with erratic on-body connectivity caused by both slow and fast fading, several solutions have been proposed for intra-WBAN communications such as BATMAC, a self-organizing, adaptive and flexible protocol that automatically detects shadowing effects, adjusts its protocols and the parameters of the IEEE 802.15.4 superframe accordingly, and quickly adapts the relaying scheduling to BAN changes. But how multiple BANs can coexist or even cooperate is still hardly evaluated. When multiple BANs are co-located and interfere with each other, coexistence algorithms (e.g. time resource sharing, time offset) should ensure a proper functionality of multiple co-located BANs and carry out, either independently or cooperatively, their own communications without severe interference. Independent BANs have the advantage to be easier to implement but cooperative BANs should be more robust by sharing the radio resources.

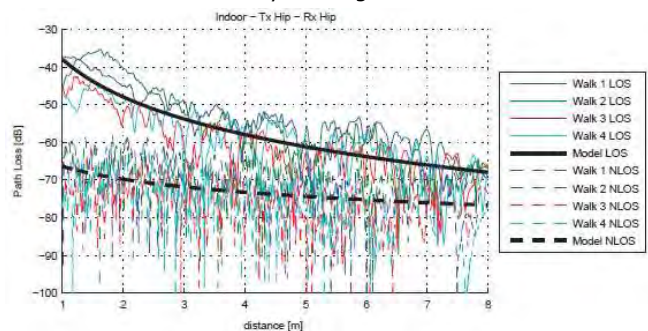


Figure 2: Body-to-Body channel with one subject walking, LOS and NLOS conditions.

Finally, future e-Health or e-Sports management systems should support unprecedented localization functionalities. The capability of provisioning accurate, reliable, long-term and privacy-aware location information could indeed favor the development of ergonomic, less intrusive and more reactive monitoring, prevention or emergency systems, as well as relevant tools to optimize the user's performance or to allow a self-learning of the good practices with quantified feedback. Exploiting opportunistically cooperative Body-to-Body communications could be beneficial for such systems. Recently, research efforts concern BAN-based group navigation, and more particularly the selection of additional cooperative Body-to-Body links in heterogeneous BAN contexts so as to improve tracking performances, from precision, energy consumption and computational complexity points of view.

#### Related Publications:

- [1] M. Maman, B. Denis, and R. D'Errico, "Research Trends in Wireless Body Area Networks: From On-Body to Body-to-Body Cooperation", *Workshop on Sensor Communications & Technologies, Body Area Networks, e-health Services and Standardization, 8<sup>th</sup> IEEE Int. Symp. on Medical Information and Communication Technology*, Florence, Italy, 2-4 April, 2014.
- [2] E. Ben Hamida, M. Mahtab Alam, M. Maman, B. Denis, R. D'Errico, "Wearable Body-to-Body Networks for Critical and Rescue Operations - The CROW<sup>2</sup> Project", *Workshop on the Convergence of Wireless Technologies for Personalized HealthCare, 25<sup>th</sup> IEEE Int. Symp. on Personal, Indoor and Mobile Radio communications (PIMRC)*, Washington, DC, 2-5 Sept. 2014.

## Cooperative wireless Body Area Networks for radio-based activity monitoring, posture detection and mobility learning

Research topics: Body Area Networks, radiolocation

B. Denis, M. Maman, L. Biard

**ABSTRACT:** Wireless Body Area Networks (WBAN) provide cooperative radiolocation means at the body scale between equipped users and/or with respect to fixed elements of infrastructure. Opportunistic, stand-alone and geographically unrestricted mobility learning and posture detection are thus feasible, beyond improved indoor navigation capabilities. Our investigations aim at demonstrating this potential based on integrated ultra-low power radio technologies and address several open issues from algorithms design to real-life experiments.

Wireless Body Area Networks (WBANs) have been fulfilling demanding needs in various user-centric application domains (e.g., e-health and silver economy, personal e-sports and e-fitness, security/coordination of soldiers and firefighters on the field, smart/connected clothing...). In this WBAN context, cooperative radiolocation schemes have been considered even more recently. The idea consists in determining the locations of on-body nodes (i.e., at the body scale and/or at the building scale) so as i) to re-inforce pedestrian navigation capabilities in indoor environments [1], ii) to learn, classify and detect daily-life mobility patterns, and finally iii) to perform coarse motion capture or posture detection (e.g., for physical activity monitoring). Such opportunistic functionalities rely on the measured Round Trip - Time of Flight (RT-ToF) or Received Signal Strength Indicator (RSSI) of data packets over on-body, body-to-body and off-body (i.e., w.r.t infrastructure) radio links. In the frame of the ANR-funded CORMORAN project (<http://pylayers.github.io/pylayers/cormoran.html>), various aspects of this problem have been investigated.

First of all, one decentralized cooperative positioning algorithm had been proposed, which asynchronously estimates the unknown coordinates of on-body nodes relatively to a body-strapped local system under geometric constraints (i.e., time-invariant fixed-length links under mobility). This algorithm has been improved through packets scheduling and censoring [2] to limit error propagation (i.e., when on-body nodes share information within their 1-hop neighborhood) but also harmful effects due to speed/connectivity disparities (e.g., peripheral on-body nodes are usually penalized). Forcing pair-wise measurements symmetry is also expected to mitigate outliers and packet losses. Preliminary simulation-based evaluations assuming realistic medium access control (MAC) constraints and packet error rates (PER) showed the resilience of the proposed solution against acquisition latency in comparison with conventional centralized or decentralized approaches like Multi-Dimensional Scaling (MDS) (Fig. 1). Our solution has also been experimentally tested based on a first generation of Impulse Radio - Ultra Wideband (IR-UWB) devices developed at CEA-Leti [3], demonstrating the feasibility of applications that would require reasonable location accuracy on the order of 20 cm (e.g., gesture-based remote control, rough attitude detection). More extensive experiments have been carried with various kinds of integrated IR-UWB and IEEE802.15.4 devices (incl. commercialized nodes) in a

heterogeneous and mesh scenario mixing on-body and off-body links [4].

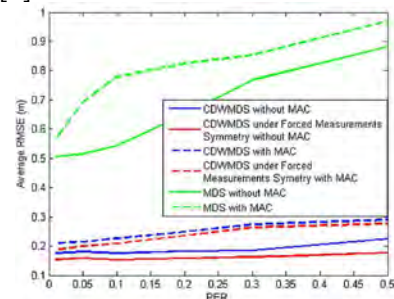


Figure 1: Relative location RMSE of 10 on-body nodes under realistic MAC and PER constraints (ranging standard deviation of 10 cm).

A first quantitative analysis of the acquired data shows for instance that the relative RSSI variations jointly observed in adequate groups of on-body links can indicate the mobility status and pattern (Fig. 2). Accordingly, it could be beneficial to human activity and body posture detection (e.g., through machine learning). Exploitable correlations between dynamic RSSIs and inter-node distances have been pointed out as well, along with typical RSSI ratios between back- and front-to-infrastructure links, caused by body shadowing as a function of the subject orientation. In turn, these properties should be advantageously exploited over body-to-body and off-body links to improve also single-user or group navigation [1] (i.e., instead of simply exploiting absolute Rx power measurements as explicit distance-dependent metrics, regardless of the obstruction regime).

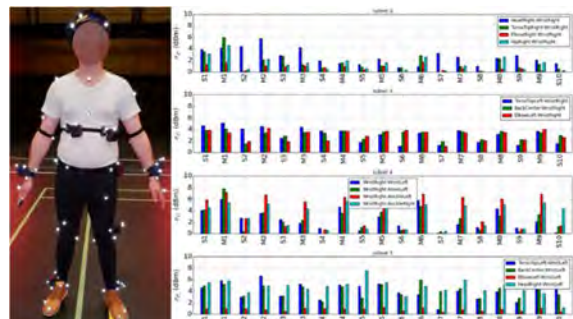


Figure 2: RSSI standard deviations at IEEE802.15.4 nodes in distinct groups of on-body links, indicating stance ( $S_x$ ) & mobility ( $M_y$ ).

#### Related Publications:

- [1] J. Hamie, C. Chaudet, and B. Denis, "Improved Navigation Capabilities in Groups of Cooperative Wireless Body Area Networks", *Int. Conf. on Body Area Networks (BodyNets'14)*, London, UK, 29 Sept.-1 Oct. 2014.
- [2] J. Hamie, B. Denis, and C. Richard, "Decentralized Positioning Algorithm for Relative Nodes Localization in Wireless Body Area Networks", *Mobile Networks and Applications Journal (MONET)*, Springer, vol. 19, no. 6, Nov. 2014.
- [3] J. Hamie, B. Denis, and M. Maman, "On-Body Localization Experiments using Real IR-UWB Devices", *IEEE Int. Conf. on Ultra Wideband 2014 (ICUWB'14)*, Paris, 1-3 Sept. 2014.
- [4] B. Denis, N. Amiot, B. Uguen, A. Guizar, et al. "Qualitative Analysis of RSSI Behavior in Cooperative Wireless Body Area Networks for Mobility Detection and Navigation Applications", *IEEE Int. Conf. on Electronics Circuits and Systems (IEEE ICECS'14)*, Marseille, Dec. 2014.



## Use of non-regenerative relays for localization performance enhancement

Research topics: wireless sensor networks, radiolocation

N. Decarli, A. Guerra, A. Conti, R. D'Errico, A. Sibille, D. Dardari

**ABSTRACT:** Network localization enables a variety of new applications that rely on the positional information of nodes. High-accuracy network localization is challenging in harsh propagation environments (such as indoor) and is limited by power emission constraints. We devise non-regenerative ultra-wideband relaying to improve the performance of network localization in terms of coverage and accuracy.

High accuracy network localization is essential for various emerging wireless applications. Network localization is typically based on an infrastructure including tags attached to or embedded in objects (agents), and reference nodes (anchors) placed in known positions. Tags' positions are inferred based on prior knowledge and measurements on signals exchanged between tags and anchors. Non line-of-sight (NLOS) conditions generated by the presence of obstacles in real environments may drastically limit the area covered by the localization system. In such severe propagation conditions, a typical approach to improve the performance and coverage of localization systems consists in increasing the number of anchors at the expense of higher infrastructure and deployment costs.

The concept of non-regenerative relaying for network localization is here introduced as a low complexity approach to increase the service coverage in localization systems operating in severe NLOS propagation conditions or when the reduction of the number of anchors is desirable to simplify the network infrastructure. Specifically, we provide the basis for the design and analysis of localization systems with Ultra-Wide-band (UWB) non-regenerative relaying.

The adoption of UWB just forward (JF) or amplify & forward (AF) relays, acting as virtual anchors, increases the number of received signal components that, thanks to a prior knowledge of relays' position, contribute in improving the localization capability in shadowed areas. Different Maximum likelihood (ML) position estimators, accounting for the knowledge of relays' position and complete or partial channel state information (CSI), have been derived together with an outliers reduction algorithm to make the ML estimation process more robust to ambiguities.

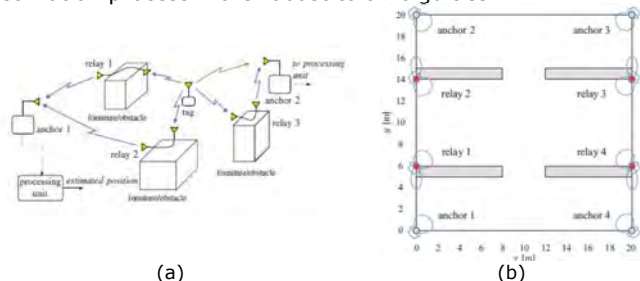


Figure 1: Example of localization system with non-regenerative relays (a), case-study (b).

Figure 1b shows the scenario considered for the case study, which is a square cell of  $20 \times 20$  meters with 4 obstacles of 1 meter width and 8 meters length. As worst-case assumption, obstacles block completely the signal

propagation and create extended shadowed areas. Anchors are placed at the 4 corners of the square cell and 4 non-regenerative relays are present in the environment, placed at the corners of the blocking obstacles (i.e., at the corners of the area partially shadowed). Each relay points its directional antenna (antenna B) towards the closest anchor and its weak directional antenna (antenna A) towards the shadowed area. Realistic UWB antennas are considered, by including in the simulation the measured antenna radiation patterns in the main polarization: an UWB Vivaldi antenna with a peak gain of 5dBi is used for anchors and relay's antenna A (tag-relay links); a four-patch array antenna with peak gain of 12 dBi is used as relay's antenna B (relay-anchor links).

As depicted in Figure 2, results have shown the effectiveness of the relaying technique for network localization, even using simple passive JF relays and low-complexity energy-based position estimators. Localization coverage enhancement through UWB non-regenerative relays is particularly attractive thanks to relays transparency to signals format, which allows the coexistence of different localization systems, and to the use of extremely low cost devices that do not require neither a communication infrastructure nor a power supply (in case of JF relays). This opens the way to a new design methodology for localization systems in severe propagation conditions, a methodology that facilitates the deployment and reduces cost and complexity of the network infrastructure.

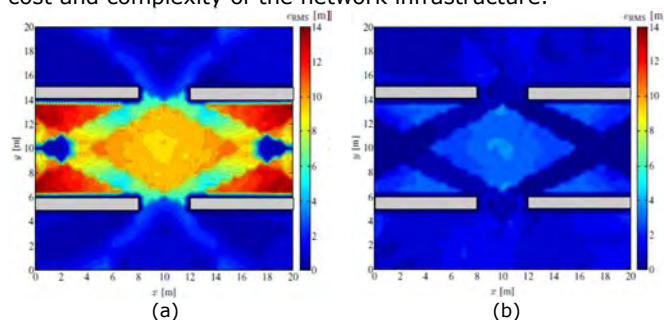


Figure 2: Localization root mean square error contour map in the 2D environment: without relay (a) and with JF relays.

This research was supported by the European Commission through the FP7 project SELECT (Grant agreement n. 257544) and by the Italian Ministerial PRIN project GRETA (Grant2010WHY5PR).

### Related Publications:

- [1] N. Decarli, A. Guerra, A. Conti, R. D'Errico, A. Sibille, and D. Dardari, "Non-Regenerative Relaying for Network Localization", *IEEE Trans. on Wireless Communications*, vol. 13, no. 1, Jan. 2014, pp. 174-185.
- [2] R. D'Errico, D. Dardari, A. Conti, and A. Sibille, "Localization method and system using non-regenerative UWB relays", Application patent EP2605032, US2013154836.

## Improved symmetric key generation from IR-UWB signals

Research topics: IR-UWB communications, security

I. Tunaru, B. Denis, B. Uguen

**ABSTRACT:** The generation of cryptographic symmetric keys using measurements of the reciprocal physical layer (e.g. received signal strength, channel responses, etc.) is an alternative to centralized key distribution techniques. Based on a previous proof of concept exploiting oversampled ultra wideband signals to generate secret keys with practical lengths, this work aims to improve the random character of such keys as well as to increase the advantage of legitimate users in comparison to eavesdroppers through range-based key reconciliation.

Contemporary wired and wireless security architectures rely mainly on high-level symmetric cryptography for data encryption as well as on public key cryptography for authentication/symmetric key distribution. In wireless decentralized networks, symmetric key distribution with classical methods becomes challenging. In this context, close nodes could take advantage of sharing a physical link to generate common secrets without additional inputs. Such schemes are possible due to the theoretical reciprocity of the propagation channel between two points (i.e., legitimate users) and due to the spatial decorrelation of wireless channels, which ensures secrecy with respect to a distant attacker. The typical phases of a physical layer key generation procedure are depicted in Figure 1.

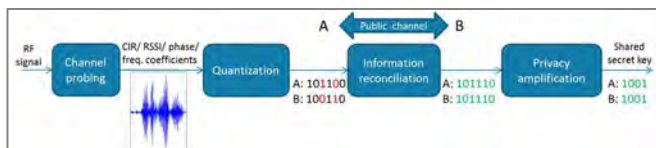


Figure 1: Typical steps in a physical layer key generation protocol.

The Impulse Radio Ultra Wideband technology (IR-UWB), one of the candidate technologies in low data rate (LDR) Wireless Sensor Networks (WSN), is particularly suitable for physical layer key generation due to its multipath resolution capabilities, which give access to entropy-rich signals. Relatively long key lengths can be obtained when using an IR-UWB metrological test-bed and applying a one-bit quantization rule with variable thresholds [1].

These results have motivated the evaluation of such keys generated from typical indoor channels [2]. Our main aim was to understand the effects of the deterministic pulse waveform and of the quantization scheme on the random nature of the extracted bits. The bit sequences generated with the initial quantization algorithm [1] failed the NIST oscillations and pattern statistical tests, which led to the proposal of an improved quantization algorithm [2]. In order to break the repeated patterns induced by the deterministic IR-UWB waveform, the new quantization algorithm varies the bit mapping rule across different thresholds depending on the multipath component dynamics, thus providing better bit diversity. The quantization is still done on one bit but the random pattern of the keys is improved while maintaining an acceptable bit agreement ratio in noisy cases.

After the individual quantization phases, the two legitimate users must agree on a common key by correcting the bit mismatches due to noise or other link asymmetries. This is done in the information reconciliation phase when the users exchange information about their quantized signals or bit sequences on the public channel. Consequently, a passive attacker placed close to one of the users could measure an approximated legitimate channel, use the reconciliation information and infer the key.

In the initial key generation protocol, POS [1], the first part of the reconciliation procedure consists in exchanging the tables of the quantized positions in clear over the public channel. We propose two improvements to this method: *BIN* (with several variants indexed by the parameter  $\Delta_{bin}$ ) based on reducing the public information and  $POS_{ToF}$  based on masking the public information with an additional reciprocal feature of the channel, the Round-Trip Time of Flight, which cannot be perfectly known by the attacker. The gains in terms of secrecy are measured by the mean illegal bit agreement ratio between the legitimate bit sequence and the one inferred by the attacker (Figure 2).

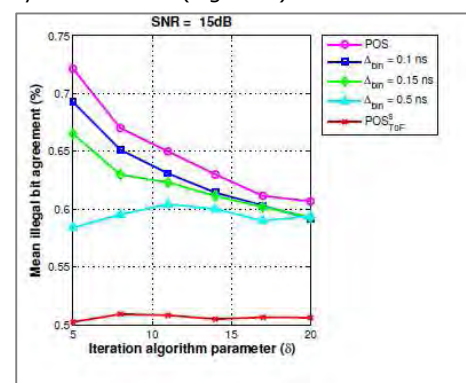


Figure 2: Secrecy evaluation of public discussion strategies.

In conclusion, we have proposed two improvements of an existing key generation procedure using directly sampled IR-UWB signals. Other parallel studies concern the reciprocity-randomness trade-off when using noisy channel estimates and multibit non-uniform quantization as well as the optimization of the quantization thresholds as a function of the signal-to-noise ratio and/or excess delay [4].

### Related Publications:

- [1] S. Tmar-Ben Hamida, J.-B. Pierrot, and C. Castelluccia, "An Adaptive Quantization Algorithm for Secret Key Generation Using Radio Channel Measurements," *Int. Conf. on New Technologies, Mobility and Security (NTMS)*, Cairo, Egypt, 20-23 Dec. 2009.
- [2] I. Tunaru, B. Denis, and B. Uguen, "Random Patterns of Secret Keys from Sampled IR-UWB Channel Responses", *IEEE Int. Conf. on Ultra Wideband 2014 (IEEE ICUWB'14)*, Paris, France, 1-3 Sept. 2014.
- [3] I. Tunaru, B. Denis, and B. Uguen, "Public Discussion Strategies for Secret Key Generation from Sampled IR-UWB Channel Responses", *IEEE Conf. on Communications 2014 (IEEE COMM'14)*, Bucharest, Romania, May 2014.
- [4] I. Tunaru, B. Denis, and B. Uguen, "Reciprocity-Diversity Trade-off in Quantization for Secret Key Generation", *IEEE Int. Symp. on Personal Indoor, and Mobile Radio Communications 2014 (IEEE PIMRC'14)*, Washington DC, Sept. 2014.

## Security protocols and privacy issues into 6LoWPAN stack: a synthesis

**Research topics: Internet of Things, wireless sensor networks, security**

C. Hennebert, J. Dos Santos

**ABSTRACT:** in this work, we synthesize the current protocols and security solutions that can be deployed in wireless networks made up of resource-constrained devices communicating on the Internet. The benefits and limitations of each scheme are explained considering the newer version of IEEE 802.15.4 standard published in 2011. Following the different levels of the 6LoWPAN stack, several security solutions like DTLS or compressed IPsec are described. Several use cases are studied to envisage the security integration. The privacy issues are also addressed and different ways to hide the device identity are discussed.

This work is intended to designers and developers of the Internet of Things to provide the technical and decision-making basis in order to integrate security into the system upon its conception [1].

To enable the development of the IoT and because the reference protocol IP is not suitable for constrained devices, 6LoWPAN (Figure 1) has been designed to provide an adaptation of the IP world to sensor networks and to achieve the suitability of IPv6 for IEEE 802.15.4 network.

Application	<i>Application</i>
UDP	<i>Transport</i>
IPv6	<i>Network</i>
6LoWPAN	<i>Adaptation</i>
MAC 802.15.4	<i>Link</i>
PHY 802.15.4	<i>Physical</i>

*Figure 1: 6LoWPAN Protocol Stack.*

An IPv6 address is 128-bits long represented in hexadecimal format. The 6LoWPAN adaptation layer supplies solution for fragmentation and reordering of IPv6 packets, and compression of the protocol stack headers.

However, it remains a key issue: ensuring security of data exchanged via 6LoWPAN. While IPsec and then TLS (Transport Layer security) become mature technologies in the world of the Internet, their adaptation in the LoWPAN world is still a challenge.

For many applications and services, the data exchanged over the network need to be cryptographically secured.

Link layer security ensures the security of the wireless medium whereas upper layer security is designed to achieve end-to-end security between two peers. It is essential to understand the security requirements and the threats to use against the right countermeasure. The security tools offer good security against attacks but they cannot be deployed at the same time because of the constraints of low-power devices.

Many challenges need to be solved to deploy and easily manage a secure network. It is important for a designer to

know the different security requirements like confidentiality or data integrity but also analyze the threats which the network has to face at each layer like Deny-of-service at physical layer or flooding at link layer. Different keys can be used following in which layer the security is applied. The key management is also an important issue of the security.

The security can be handled at the link layer thanks to the features specified in the IEEE 802.15.4-2011 standard. 7 levels of security are available of whom the AES-CCM\* provides data encryption and authentication. Nevertheless the standard doesn't specify how the key have to be exchanged and some attacks like fake packet injection can be launched if security is not used correctly.

At the network layer, compressed IPsec for 6LoWPAN can be used to insure security. IPsec is a protocol suite for securing Internet by authenticating and encrypting each IP packet of a communication session. The use of IPsec into a LoWPAN is possible but the encryption takes many resources and leads to a significant overhead.

At the application layer, DTLS is a protocol used to secure network traffic. It is based on TLS and usable with UDP datagram. DTLS manages the UDP packet loss, the packet reordering at reception and operates on smaller frames. Moreover, it is not optimal for constrained resources and trade-off solutions are proposed in the literature.

Among the security services, the encryption ensures the confidentiality of the data exchanged over the network. The integrity and the authentication of the whole frame can be guaranteed, but the confidentiality of information included in the header remains unprotected. This causes a problem for privacy. To protect them, the use of temporary stateless addresses auto configuration can be envisaged. Another solution is the Cryptographically Generated Address (CGA). Nevertheless, these two solutions don't provide a complete solution for privacy preserving.

Several end-to-end security use cases have been studied to highlight how the security schemes described previously could be used in a real system and what are the challenges to be addressed in the future work.

#### Related Publications:

[1] C. Hennebert, J. Dos Santos, "Security protocols and privacy issues into 6LoWPAN stack : a synthesis", *IEEE Internet of Things Journal*, vol. 1, no. 5, Oct. 2014, pp. 384-398.

## Security of spread spectrum communications

Research topics: wireless communications, security

M. des Noes, V. Savin

**ABSTRACT:** Gold sequences are widely used in communications and positioning systems for synchronization purposes or spread spectrum transmissions. This paper addresses the decoding of the initial state of a Gold sequence. This can be used to detect spread spectrum communications if the sequence generator is known. The decoder implements an iterative message-passing algorithm which is built upon a parity-check matrix. Thus, it depends on the coding properties of Gold codes. In this work, we synthesize the coding properties of Gold codes and use them to compute the number of parity check equations of weight  $t=3$ ,  $4$  or  $5$ . Eventually, the impact of the parity check equations used for decoding is highlighted.

Gold sequences form a family of binary sequences with excellent correlation properties. Hence, they are widely used for synchronization purpose in wireless communications and positioning systems, and also for spread spectrum communications. A Gold sequence  $z(k)$  is generated with a preferred pair of  $m$ -sequences  $x(k)$  and  $y(k)$ :  $z(k) = x(k) \oplus y(k)$ .

The conventional method to synchronize with a Gold sequence is to correlate the received signal with a replica of the searched sequence. If a correlation peak is observed and is above a given threshold, the synchronization is declared. An alternative method consists in performing detection through a decoding of the received sequence. In fact, a  $m$ -sequence generator can be regarded as a linear code generator (Figure 1). It is thus possible to detect a transmitted sequence with a suitable decoder. Exploiting the unique properties of these sequences, an iterative message-passing algorithm can be implemented to decode the received signal.

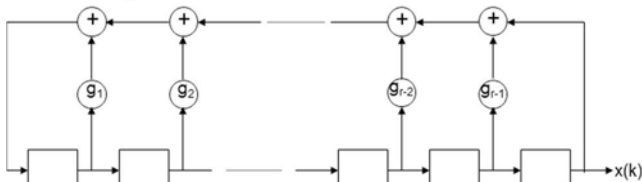


Figure 1:  $M$ -sequence generator (Fibonacci representation).

The decoding procedure is known to be sensitive to the weight of the parity check equations. It is given by the number of non-zero coefficients of the equation. It is thus fundamental to study these parity check equations for Gold sequences. In [1], we provided a synthesis of Gold sequence properties from the viewpoint of coding theory. A Gold sequence is a codeword of a cyclic linear code characterized by the generator polynomials of  $m$ -sequences  $x(k)$  and  $y(k)$ . For the decoding procedure, we are interested in the properties of the dual code, since it defines the parity check equations used for decoding. This work is helpful for evaluating the number of parity-check equations of weight  $t = 3, 4$  or  $5$ . This tells us, if these equations at least even

exist and if yes, how many can be used for decoding. The goal is to use parity-check equations having the smallest weight  $t$  for decoding.

The number of parity-check equations of weight  $t = 3$  and  $4$  has already been computed by Kasami. In [1], we provided an analytical expression for the number of parity check equations of weight  $t = 5$  when the degree of the generator polynomial  $r$  is odd:

$$N_5 = \frac{(2^{r-1} - 1)(2^{r-1} - 4)}{6}$$

This ensures there will be a sufficiently large amount of parity check equations of weight 5 for practical implementation.

Then, we have measured the probability of missed detection as a function of  $t$ . Figure 2 shows the probability of missed detection as a function of the input SNR for 2 Gold sequences. The sequences are identified with the octal representation of their  $m$ -sequences. The case ' $t = 5$ ' corresponds to the Gold sequence 4005-4445 of odd degree  $r = 11$  and ' $t = 4$ ' to 2157-3515 of even degree  $r = 10$ . We observe a degradation of 2 dB when the weight of parity-check equations increases from  $t = 4$  to 5. As a result, a spread spectrum communication system employing Gold sequences of even degree are easier to detect and identify.

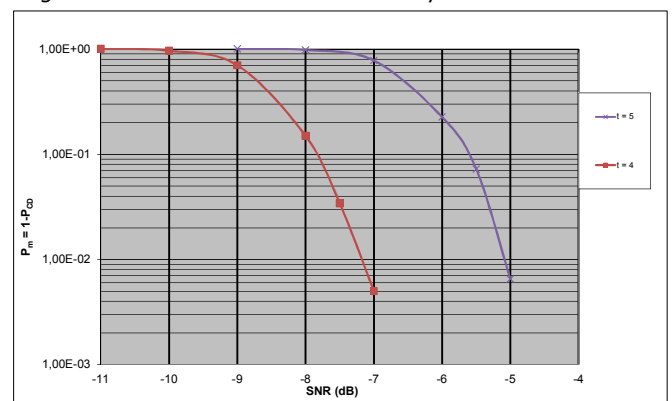


Figure 2: Probability of missed detection.

#### Related Publications:

[1] M. des Noes, V. Savin, L. Ros and J.M. Brossier, "Sécurité des communications par étalement de spectre", *Journées Codage et Cryptographie*, Les 7 Laux, France, 24-28 Mars 2014.



## Using the joint distributions of a cryptographic function in side channel analysis

Research topics: smart-card, security, side-channel attacks

Y. Linge, C. Dumas, S. Lambert-Lacroix

**ABSTRACT:** The Side Channel Analysis is now a classic way to retrieve a secret key in the smart-card world. Unfortunately, most of the ensuing attacks require the plaintext or the ciphertext used by the embedded algorithm. We present a new method for exploiting the leakage of a device without this constraint. Our attack is based on a study of the leakage distribution of internal data of a cryptographic function and can be performed not only at the beginning or the end of the algorithm, but also at every instant that involves the secret key. We also propose a way to proceed in a noisy context using smart distances.

Side Channel Attacks are generally based on statistical properties and tend to compare two random variable groups. The first one is represented by all the points of the acquired traces, while the second one depends on the underlying cryptographic function. For example, the Correlation Power Analysis (CPA) consists in the correlation between the device leakage at one instant and the possible value of one intermediate data. For the attack achievement, this value must be computable, i.e. it only depends on some few key bits and it is obtained from the plaintext (or the ciphertext). When neither is known, the acquired trace cannot be connected to any cryptographic algorithm data. The two random variable groups may only be studied independently. It was interesting to us to assume that we do not have any prior knowledge of the plaintext and the ciphertext. In fact, many smart-card applications use cryptographic functions without outputting the plaintext and ciphertext. In this case no internal data can be guessed, even partially, and a classic attack like CPA is not conceivable.

Nevertheless, the acquired traces contain some leakage information and we presume that it is correlated to the data computed by the device. Failing to associate one trace to its corresponding algorithm guessing value, we can still study separately the various instants and the different algorithm values that involve a part of the key. This forms the main idea of our proposition [1].

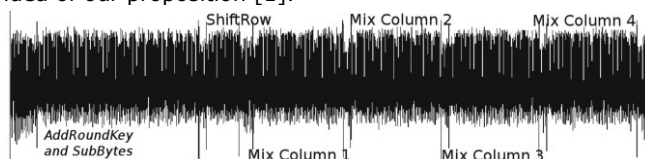


Figure 1: Electromagnetic emanation signal during the execution of the first round of an AES128 software implementation.

An algorithm may be decomposed in small functions that mostly use a part of the secret key. We will denote by  $g$  one of these functions and by  $k$  the involved part of the secret key, named subkey. We propose to study how the output  $b = g(a, k)$  varies when the input  $a$  is uniformly distributed in  $A$ . More precisely, we are interested in the leakage caused by  $a$  and  $b$ . Let's denote by  $L(z)$  the leakage induced by the handling of the data  $z$ .  $L(z)$  is comprised of the leakage function  $\phi$  and the leakage noise  $B$ . We consider the random variables  $\phi(a)$  and  $\phi(g(a, k))$  for all possible  $k$  and the joint probability distributions  $(\phi(a), \phi(g(a, k)))$  for all  $k$ . We denote for each subkey  $k$  the joint probability distribution by

$S(g, k) = \{p_{i,j}\}$  where  $p_{i,j}$  is the probability that  $\phi(a) = i$  and  $\phi(g(a, k)) = j$ . As  $\phi(g(a, k))$  depends on  $k$ , each distribution also depends on the subkey value  $k$ . If we get the distribution for an unknown subkey  $k$  and if each subkey  $k$  matches with a unique distribution, we are able to guess the value of  $k$  by comparing the distributions. However, an attacker will face two problems.

First, he must be able to get a distribution that will be compared to the theoretical ones, knowing he has access only to some traces. As the traces contain some information but also noise, he will only be able to estimate the frequency of the couple  $(\phi(a) = i, \phi(b) = j)$  denoted  $f_{i,j}$ . We name  $Sd = \{f_{i,j}\}$  the estimated distribution of the device. We have proposed to deduce this distribution from the acquired traces thanks to a simple Hamming weight estimator based on the statistical variance and the particular repartition of random variables.

The second problem the attacker faces is the need for a method to compare two distributions  $S(g, k)$  and  $Sd$ . Other groups proposed a comprehensive study of different distances between two distributions. When trying to match a distribution that is well estimated to the theoretical ones, most distances give similar results and return the good subkey with few samples. But if the device distribution is not well estimated because of the presence of errors for some samples, some distances give better results than others. We simulated 50% erroneous samples to obtain biased device distributions and tried all the distances to compare each estimated distribution to the theoretical ones. We kept the best distances, that are those that on average lead to a successful attack.

In the ideal case where the Hamming weight estimation is always correct, our proposed attack is very effective and the true key is found with fewer than 30 samples. In the real world, the acquired signals are noisy and the estimator is not perfect. But, with more samples the attack still remains successful, even with 50% of estimation error.

Indeed, we have validated both the estimation method and the key recovery by applying our attack on two sets of acquisition. The first one contains 1,000 traces issued from an AES128 software implementation into an ATMega2561. The results show that 10 disordered key bytes can be retrieved without any knowledge of the plaintext or the ciphertext. The second one comes from the DPAContest v4. Here we found 7 ordered bytes of the key.

### Related Publications:

[1] Y. Linge, C. Dumas, and S. Lambert-Lacroix, "Using the joint Distributions of a Cryptographic Function in side Channel Analysis", *COSADE 2014*, Paris, France, 14-15 April 2014.





# 3

## Antennas and propagation

*Miniature antennas*  
*WBAN propagation channel*  
*Millimeter-wave antennas*

## Super directive compact antenna design using spherical wave expansion

Research topics: miniature antennas, super directivity

A. Clemente, M. Pigeon, L. Rudant, C. Delaveaud

**ABSTRACT:** This contribution presents a method for the synthesis of super-directive compact antenna arrays based on spherical wave expansion. The optimization procedure has been derived from the maximum normal directivity defined by Harrington and applied for the optimization of a three- and a five-element compact antenna array of  $0.4\lambda \times 0.25\lambda$  constant maximum size. A maximum directivity of 10.4 and 14.5 dBi has been obtained by full-wave simulations.

Compact antennas have long been studied and their theoretical limitations in terms of maximum directivity, quality factor and efficiency are the topic of several works. The maximum attainable directivity ( $D = N^2 + 2N$ ) in a given direction as a function of the order of spherical modes associated to the antenna radiation ( $N$ ) has been derived by Harrington. Due to Harrington's definition of  $N$ ,  $N = kr$  with  $r$  is the radius of the minimum sphere circumscribing the antenna and  $k$  is the wavenumber, this limit does not respect the directivity of the Huygens source (4.8 dBi) in the case of infinitesimal antennas and does not respect the directivity definition in the case of  $2\pi/\lambda < 0.13$  (Fig. 1). A renormalization of the Harrington limit has been proposed in our recent paper [1,2]. The proposed renormalization respects the directivity limit calculated by Geyi in the case of infinitesimal antennas and converges to the Harrington limit and the uniform circular aperture directivity for antennas larger than  $2\pi/\lambda$ . An antenna is called super-directive if its directivity is higher than that obtained with the same antenna size in the case of the theoretical normal directivity.

A method to design super-directive compact antenna arrays (phased and parasitic arrays) is presented and validated by full-wave simulations. The method is based on the spherical wave expansion of radiated fields.

An electric field  $\vec{E}$  at large distance ( $kr \rightarrow \infty$ ) outside an enclosing spherical surface including all the field sources can be represented as a linear combination of far-field spherical wave pattern functions  $\vec{K}_{smn}(\theta, \varphi)$ :

$$\vec{E}(r, \theta, \varphi) = \sqrt{\eta} \frac{k}{\sqrt{4\pi}} \frac{e^{ikr}}{kr} \sum_{s=1}^2 \sum_{n=1}^N \sum_{m=-n}^n Q_{smn} \vec{K}_{smn}(\theta, \varphi) \quad (1)$$

where  $\eta$  is the specific impedance of the medium assumed complex and  $Q_{smn}$  are the spherical wave coefficients. In 1958, Harrington established a limit on the maximum attainable directivity in a given direction ( $\theta_0, \varphi_0$ ) depending on the number of spherical modes associated to the antenna radiation when wave functions up to  $n = N$  are included:

$$D_{\max}(\theta_0, \varphi_0) = \sum_{n=1}^N (2n+1) = N^2 + 2N \quad (2)$$

In the case of an antenna array, composed of  $p$  elements, the maximum directivity can be obtained by combining the modes associated to the radiation of each array element:

$$Q_{smn}^{\max} = c \cdot \vec{K}_{smn}^*(\theta_0, \varphi_0) = \sum_{p=1}^p \alpha_p \cdot Q_{smnp} \quad (3)$$

where  $c$  is an arbitrary constant, the symbol  $*$  represents the complex conjugate operation,  $\alpha_p$  is the excitation coefficient applied on each element, and  $Q_{smnp}$  are the spherical wave coefficients associated to the  $p$  element.

The proposed optimization procedure has been used to optimize two compact array antennas of size  $0.4\lambda \times 0.25\lambda$  ( $2\pi/\lambda = 0.47$ , equivalent effective size of a dipole) at 1.36 GHz. The two arrays are composed of three and five closely-spaced half-wave electric dipoles, respectively. Starting from full-wave electromagnetic simulations to compute the electric field of each elementary dipole when the impedance of the other array elements is fixed to  $50 \Omega$ , the proposed synthesis procedure is used to calculate the optimal excitation coefficients in terms of maximum directivity. The optimal coefficients are used to calculate the theoretical and simulated field. A maximum directivity of 10.4 and 14.5 dBi has been obtained in the case of three- and five-element array, respectively. The maximum directivity of the two compact arrays is compared with the theoretical limits in Fig. 1 where the Harrington limit, the Geyi limit, and the renormalized Harrington limit are plotted.

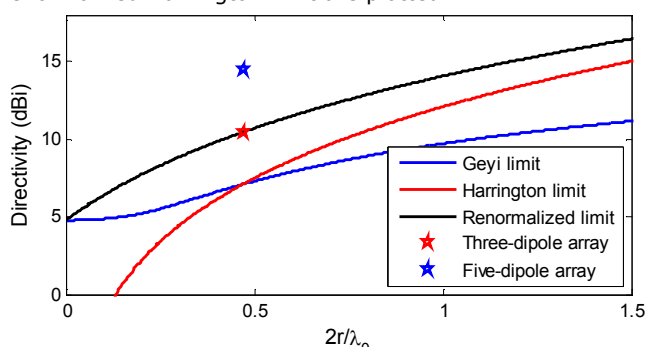


Figure 1: Directivity of the two compact arrays compared to the theoretical limits (★ Full-wave electromagnetic simulation).

### Related Publications:

- [1] M. Pigeon, A. Clemente, C. Delaveaud, and L. Rudant, "Analysis of Harrington limit for electrically small antenna directivity," *8<sup>th</sup> European Conf. on Antennas and Propag (EuCAP)*, The Hague, The Netherlands, 6-11 April 2014.
- [2] A. Clemente, M. Pigeon, L. Rudant, and C. Delaveaud, "Super directive compact antenna design using spherical wave expansion," *IEEE Int. Symp. on Antenna and Propag. (APS-URSI)*, Memphis, TE, 6-11 July 2014.



## Single and differential miniature UWB antennas on chip packaging

Research topics: miniature antennas, UWB antennas

O. Clauzier, S. Bories, C. Delaveaud

**ABSTRACT:** A comparison study between single and differential feeding of UWB antennas for body area network (BAN) applications is presented. The antennas are integrated on a chip packaging (QFN64 package) for compactness and their main polarization is normal to the main plane of the package to satisfy BAN propagation constraints. Both of the antennas provide broadband characteristics and omnidirectional radiation patterns over the whole 7–9 GHz frequency band.

In wireless devices, the area and volume dedicated to the antenna become increasingly constraint. To meet this compactness challenge, antennas can be directly integrated on a chip packaging such as a Quad Flat No-leads (QFN) package. As a proof of concept, a classical Printed Circuit Board technology is used to fabricate the radiating part of the antenna which covers the package like a dome lid (Fig. 1). Thus, the proposed antenna doesn't require any additional area since it reuses the existing PCB as a ground plane. The antenna/chip connections are set regarding the RF I/O pins placement.

In this work, the antennas should be placed on smart glasses. Thus, to limit propagation losses, the antenna design is chosen in order that the main polarization is orthogonal to the body surface [1]. Two UWB antennas on package aiming wideband performances (7–9 GHz) and omnidirectional radiation patterns are developed.

The first one is a 50- $\Omega$  single-fed antenna detailed in [1]. This antenna is based on a half-wavelength thick half loop antenna (Fig. 1). A large ground plane (40x40 mm<sup>2</sup>) is used to halve the structure of the loop thanks to the image theory principle. The multi-resonator technique is used to enhance the frequency bandwidth of this low-profile antenna (11x11x4 mm<sup>3</sup>).

The second antenna is a 100- $\Omega$  differential-fed antenna inspired from a monopolar wire-plate antenna [2]. A good trade-off between the thickness of the substrate and the reflection coefficient is acquired for a 5-mm height, which represents a thickness of  $\lambda_{LF}/8.6$ , where  $\lambda_{LF}$  is the wavelength at the lowest frequency of the operating band (7 GHz).

The two antennas exhibit similar performances and broadband characteristics [2]: a reflection coefficient lower than -9.5 dB between 7 GHz and 9 GHz, a similar monopolar-type radiation patterns, and a total efficiency higher than 60% over the specified frequency band. The differential antenna can be directly connected to active components of the RF integrated transceiver in the future and is known to be less sensitive to environment. At last, an additional advantage of the differential antenna is the reduced near-field radiation level that may alters the chip performance.

Moreover, the proposed on package design technique allows also to reach directive radiation pattern [3]. This study is partially funded by the ANR in the framework of the RUBY project.

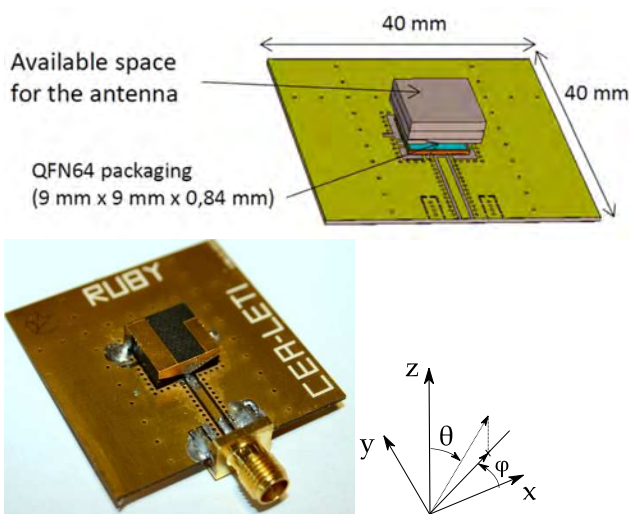


Figure 1: Single fed UWB antenna on package description and prototype.

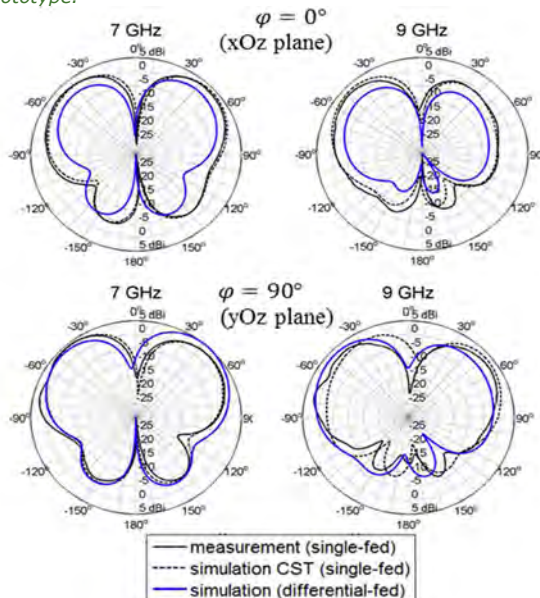


Figure 2: Gain pattern comparison between single and differential fed antennas for 7 and 9 GHz.

### Related Publications:

- [1] O. Clauzier, S. Bories, C. Delaveaud, "UWB antenna on chip packaging for BAN applications," *8<sup>th</sup> European Conference on Antennas and Propagation (EuCAP)*, The Hague, The Netherlands, 6-11 April 2014.
- [2] O. Clauzier, S. Bories, C. Delaveaud, "Comparison study between single and differential miniature UWB antenna," *21<sup>st</sup> IEEE Int. Conf. on Electronics, Circuits and Systems (ICECS)*, Marseille, France, 7-10 Dec. 2014.
- [3] O. Clauzier, S. Bories, C. Delaveaud, "Low-profile directional UWB antenna on chip packaging," *IEEE Int. Conf. on Ultra-WideBand (ICUWB)*, Paris, France, 1-3 Sept. 2014.

## Miniaturized notch antenna based on lanthanum titanium perovskite oxide thin films

Research topics: miniature antennas, materials for RF applications

H. Nguyen, R. Benzerga, Y. Lu, C. Delaveaud, C. Le Paven, A. Sharaiha, L. Legendre, F. Tessier, C.

**ABSTRACT:** This work describes the first integration of a dielectric lanthanum titanium oxide compound as thin film in a discrete capacitive component operating at microwaves. The integration in a notch antenna of a MIM (Metal/Insulator/ Metal) structure based on this oxide material is numerically and experimentally studied. Inserting this original MIM capacitor in the antenna structure results in a shift to a lower value of its operating frequency, this corresponds to a significant antenna size reduction of 64.2%.

The generalization of wireless communicating objects has intensified the need for miniaturization of integrated devices, in particular antennas. Many techniques have been developed, including the use of localized capacitive loading based on a dielectric thin film that can be used in different antenna topologies.

In this work, we developed a capacitor based on perovskite type oxide La<sub>2</sub>Ti<sub>2</sub>O<sub>7</sub> (LTO) dielectric thin films and studied its integration in a slot antenna. Previous studies on thin film deposition and dielectric characterization [1] of La<sub>2</sub>Ti<sub>2</sub>O<sub>7</sub> oxide and LaTiO<sub>2</sub>N oxynitride compounds have shown that the oxide films present losses lower than 0.02 at 10 GHz. A particular capacitor design is carried out to integrate the LTO based MIM (Metal/Insulator/Metal) components in a slot antenna structure. Special attention is given to the miniaturization ratio and to the loss introduced by the LTO based component.

The MIM (Metal/Insulator/Metal) structure is made of two concentric metallic discs deposited on the dielectric LTO layer (Figure 1a), that is itself deposited on conductive substrates, such as platinized substrates (silicon or SrTiO<sub>3</sub>). With this configuration, the value of the total capacitance is adjusted towards the small value of the central disc capacitance. The value of the MIM capacitance can be controlled by the following parameters: thin film thickness, central disc diameter and dielectric constant of the thin film [2].

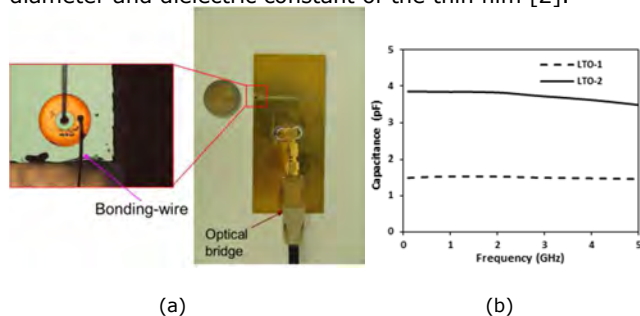


Figure 1: (a) La<sub>2</sub>Ti<sub>2</sub>O<sub>7</sub> based MIM structures and antenna prototype and (b) frequency variation of capacitance for LTO-1 and LTO-2 thin film samples.

The antenna structure consists of a notch cut from the edge of the ground plane [3]; it is the complementary structure of a conventional quarter wavelength monopole. The antenna is loaded with the MIM capacitor at the open end of the slot (Figure 1a). For prototyping, the notch antenna is printed on a standard FR4 substrate chosen for low cost. The

connections between concentric electrodes and the ground plane are made by 25- $\mu$ m diameter gold bond wires (Figure 1a).

The LTO thin films are deposited by RF magnetron sputtering (Plassys MP4505S) on conducting substrates (Pt/Si and Pt/SrTiO<sub>3</sub> substrates) from a homemade La<sub>2</sub>Ti<sub>2</sub>O<sub>7</sub> oxide target. For this study, two different thicknesses of films (470 nm for LTO-1/Pt/Si sample and 1200 nm for LTO-2/Pt/SrTiO<sub>3</sub> sample) are tested. The LTO films are identified by X-ray diffraction as the La<sub>2</sub>Ti<sub>2</sub>O<sub>7</sub> compound with an orthorhombic crystalline cell. In order to produce the MIM structure, concentric metallic discs making the upper electrodes are realized by standard photolithography and wet-etching methods of a metallic bilayer. This metallization is realized by magnetron sputtering deposition. Concerning the intrinsic properties of La<sub>2</sub>Ti<sub>2</sub>O<sub>7</sub> films, measurements of MIM structures (Figure 1b) give capacitance values of 1.5 and 3.8 pF at 1 GHz for LTO-1 and LTO-2 samples, respectively. The experimental central disc radii are 33 and 32  $\mu$ m; the dielectric constant values are 64 and 61, with loss tangent of 0.004 and 0.003 at 1 GHz for LTO-1 and LTO-2, respectively.

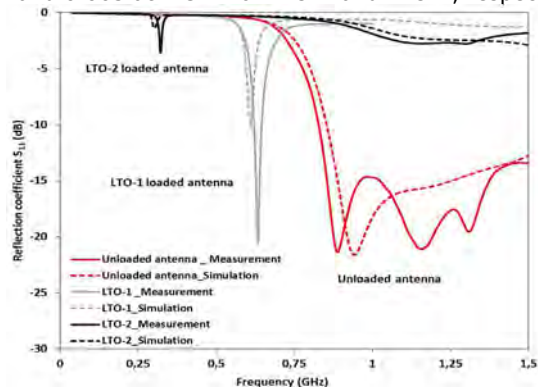


Figure 2: Comparison of measured and simulated reflection coefficient of antennas based on La<sub>2</sub>Ti<sub>2</sub>O<sub>7</sub> dielectric oxide films.

The measured reflection coefficients of the antennas based on LTO-1 and LTO-2 films (Figure 2) show that the operating frequency of the antenna shifts to lower values after integration of MIM capacitors. The experimental results are consistent with those of simulation. The impedance mismatch is due to the impedance locus variation with frequency. The study of the reduction in radiation efficiency has proven to be more related to antenna miniaturization than losses introduced by the MIM capacitors.

### Related Publications:

- [1] H. Nguyen, R. Benzerga, Y. Lu, C. Delaveaud, C. Le Paven-Thivet, A. Sharaiha, L. Le Gendre, F. Tessier, F. Cheviré, X. Castel, "New La-Ti-O perovskite oxide thin films for miniaturized notch antenna", *European Material Research Society Spring Meeting (E-MRS 2013)*, 2013.
- [2] H. Nguyen, R. Benzerga, Y. Lu, C. Delaveaud, C. Le Paven, A. Sharaiha, L. Le Gendre, F. Tessier, F. Cheviré, X. Castel, "Miniaturized notch antenna based on lanthanum titanium perovskite oxide thin films", *Thin Solid Films*, vol. 563, 31 July 2014, pp. 36–39.
- [3] H. Nguyen, R. Benzerga, C. Delaveaud, A. Sharaiha, Y. Lu, C. Le Paven, L. Le Gendre, X. Castel, "New Thin Film Varactor for Frequency Tunable Slot Antenna," *European conf. on Antennas and Propagation (EuCAP)*, 2012.

## Cable-less broadband impedance measurement technique for miniature antenna using optical/RF transceivers

Research topics: miniature antennas, antenna characterization

J-F. Pintos, C. Jouanlanne, S. Bories

**ABSTRACT:** Antenna impedance measurements are usually performed with a coaxial cable connected to the RF input port. For miniature or very integrated antennas, the presence of a coaxial cable can alter drastically the impedance and radiation behaviors. A new broadband measurement method, based on a RF/optical transceiver avoiding the coaxial cable disturbance, is presented. A validation based on an arbitrary load and a canonical antenna measurement is proposed as well as a practical use case for a TETRA Pager.

Handsets and more generally nomad/portable devices have multiple antennas to communicate according to different standards. To measure their performances (reflection coefficient, radiation patterns) a RF probe is often necessary. If the size of the antenna structure (radiator + metallic chassis) is large enough compared to its operating wavelength, a simple coaxial cable can be used. In the case of miniature or very integrated antennas, this method can lead to inaccurate measurement results due to the perturbation introduced by the measurement device. To overcome this issue, some methods have already been proposed (RCS measurements [1], Fiber-Optic Link (FOL) [2]). This work proposes an alternative cable-less broadband method to measure the complex input impedance of an Electrically Small Antenna (ESA) using a RF splitter and two FOLs [3].

In this method, the coaxial cable is replaced by a splitter, whose sum port is connected to the Antenna Under Test (AUT) and the two other ports are connected to the two FOLs (Fig. 1). One FOL, called "Uplink FOL", carries the RF signal from the port 1 of the VNA to the AUT into the anechoic chamber while the second FOL, "Downlink FOL", carries two signal components back to the port 2 of the VNA. The first component is the direct transmission due to a non-ideal isolation of the splitter, while the second component contains the AUT complex impedance information since it has reached the AUT port and has been reflected back.



Figure 1: Picture of the test bench.

The test bench can be modeled as a three ports flow graph with the AUT port and the two VNA ports (Fig. 2). Solving this flow graph, assuming that the VNA ports are perfectly matched to  $50 \Omega$ , yields to a simple relationship between the AUT reflection coefficient ( $\Gamma_{AUT}$ ) and measured transmission coefficient ( $T = b_3/a_2$ ).

Like in the one port 3-term error model, only 3 independent unknowns remain ( $S_{11}$ ,  $S_{32}$ ,  $S_{12}S_{31} - S_{12}S_{31}$ ) which are respectively port 1 match, transmission isolation and transmission tracking.

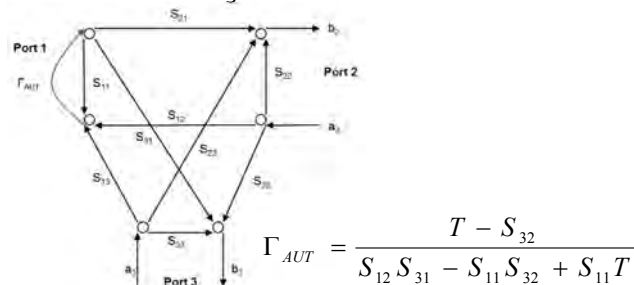


Figure 2: 3 ports flow graph with AUT connected to the port 1.

The S-parameter measurement of a highly integrated TETRA ESA in a Pager has been carried out using the optical measurement setup. The measured antenna is a miniature reconfigurable antenna presenting a dipole-like radiation pattern along the longest dimension. It is considered as an ESA since its dimensions are  $\lambda_0/9 \times \lambda_0/34 \times \lambda_0/12$  (including the pager chassis).

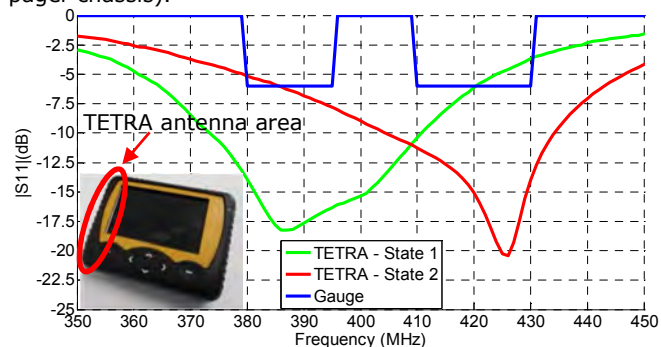


Figure 3: TETRA Antenna matching.

This antenna has been designed to address the TETRA band from 380 MHz to 430 MHz subdivided into two sub-bands 380-395 MHz and 405-430 MHz, thanks to an active matching network.

A very good matching level ( $S_{11} < -11$  dB) is obtained for the full TETRA band (Fig. 3). The impact of the measurement system on the antenna impedance is minimized and the S-parameters measurement leads to realistic results.

### Related Publications:

- [1] S. Bories, M. Hachemi, K.H. Khelifa, C. Delaveaud, "Small antennas impedance and gain characterization using backscattering measurements," 4<sup>th</sup> European Conference on Antennas and Propagation (EuCAP), 12-16 April 2010.
- [2] S. Bories, G. Le Fur, L. Cannavo, C. Lach and C. Delaveaud, "NonInvasive Radiation Patterns Measurement of Electrically Small Antenna using Fiber Optic Link", AMTA 33rd Annual Symposium, Denver, Colorado, 16-20 Oct. 2011.
- [3] J-F. Pintos, C. Jouanlanne and S. Bories, "Cable-Less Broadband Impedance Measurement Technique for Miniature Antenna Using Optical/RF Transceivers," IEEE Conference on Antenna Measurements & Applications (CAMA), Antibes, France, Nov. 2014.



## Impedance and radiation measurement methodology for ultra miniature antennas

Research topics: miniature antennas, antenna characterization

L. Huitema, C. Delaveaud, R. D'Errico

**ABSTRACT:** Conventional measurement setups can affect the properties of small antennas (impedance, radiation) and these effects have been investigated by simulation and prototype measurements. Two new characterization methodologies for ultra-miniature antennas have been developed: a first one is dedicated to the impedance measurement and the second one to the radiation measurement. These techniques rely on the use of electromagnetic simulations to compensate the perturbations and extract the isolated antenna properties.

The miniaturization of electronic devices requires the size reduction of the radiating element, which is a significant challenge for antenna designers. Furthermore, it is well-known that small antennas are limited by fundamental physical limits, generally in terms of radiation performances (efficiency) and bandwidth (quality factor). In addition to the challenge of designing ultra-compact antennas, their accurate characterization is an issue rarely discussed in detail in the literature. More specifically, the use of a feeding cable becomes quite problematic for a miniature antenna over a small-size ground plane. Indeed, with the cable in the reactive-field of the antenna, the near field and current distribution can be modified, resulting into a disturbance of both radiation and impedance characteristics.

Rather than removing this measurement cable [1], a technique based on the characterization of the perturbation has been developed for the accurate measurement of electrically-small antenna impedance and radiation [2].

The antenna impedance measurement is performed in an anechoic chamber with a measurement cable several meters long covered by RF absorbers. This measurement set-up can be considered equivalent as an infinitely long cable supporting propagating currents. With 3D electromagnetic simulations, this cable configuration can be simulated with absorbing boundary conditions at the extremity of the cable to simulate an infinite cable without a standing waves. Once the measurement context is properly taken into account in the electromagnetic simulation tool, we can use the simulation results to characterize the measurement cable alteration. We propose to model the effect of the cable through a complex transfer function,  $H_{imp}(f)$ , defined as the ratio between the antenna impedance  $Z_{ca}(f)$  including an infinitely long feeding cable and the isolated antenna impedance only  $Z_a(f)$ :

$$H_{imp}(f) = \frac{Z_{ca}(f)}{Z_a(f)} \quad (1)$$

The transfer function (1) can be determined from the simulated single antenna impedance and "antenna + infinite coaxial cable" results, the latter being in agreement with measurements. Thus, by using the inverse transfer function with measurement results, we are able to retrieve the properties of the antenna prototype without the disturbances introduced by the measuring cable.

A similar methodology has been developed for accurate measurement of small antenna radiation properties. However, it was identified that the condition of infinite length

cable can be hardly handled in both measurement and simulation radiation results. Consequently, instead of using a feeding cable, we considered a small autonomous signal generator directly connected to the antenna port, whose effect on antenna properties has been characterized by simulation. The simulation results have been then used to extract a 3D transfer function from radiated far fields. The transfer function ( $F_{AO,AD}(\theta, \varphi, f)$ ) modulus can be expressed from radiation intensity  $U(\theta, \varphi, f)$ :

$$|F_{AD,AO}(\theta, \varphi, f)|^2 = \frac{U_{AD}(\theta, \varphi, f)}{U_{AO}(\theta, \varphi, f)} \quad (2)$$

where the subscript AO denotes the antenna alone and subscript AD denotes "antenna + measurement device" configuration.

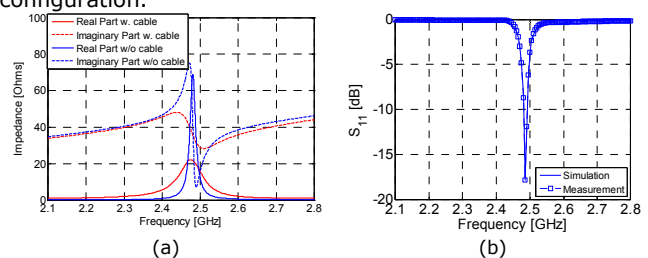


Figure 1: comparison of antenna input impedances with and without cable (a); corrected reflection coefficient measurement with predicted simulation (b).

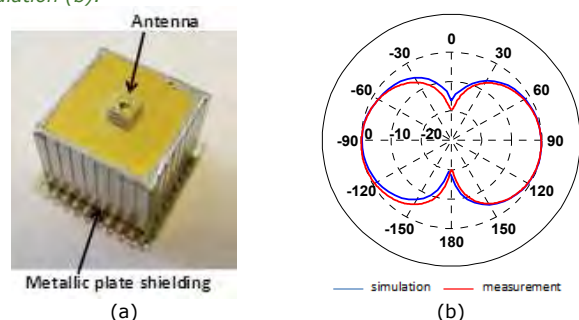


Figure 2: Ultra miniature antenna over the shielded signal generator (a) Comparison of the simulated and measured radiation patterns.

These methods have been firstly tested on a sub-miniature antenna (max dimensions lower than  $\lambda/18$ ) [2], then successfully applied to a different compact antenna [3] revealing some aspects of the alteration phenomena of miniature antennas.

### Related Publications:

- [1] M. Hachemi, S. Bories, K.H. Khelifa, and C. Delaveaud, "Miniature antenna radiation pattern measurement using fiber-optic link," *4<sup>th</sup> European Conference on Antennas and Propagation (EuCAP)*, pp.1-5, 12-16 April 2010.
- [2] L. Huitema, C. Delaveaud, and R. D'Errico, "Impedance and Radiation Measurement Methodology for Ultra Miniature Antennas," *IEEE Trans. on Antennas and Propagation*, vol. 62, no. 7, July 2014, pp.3463-3473.
- [3] L. Huitema, C. Delaveaud, and R. D'Errico, "Impedance measurement methodology for small antennas: Application to two different designs," *IEEE Conf. on Antenna Measurements & Applications (CAMA)*, Antibes, France, 16-19 Nov. 2014.



## A non-stationary channel model for on-body communications

**Research topics: propagation, channel modeling, body area networks**

**R. D'Errico, O.P. Pasquero, R. Rosini, M. Arnesano, C. Oestges**

**ABSTRACT:** The temporal variation of spatial correlation between on-body radio links are empirically characterized for different walking scenarios. Non-stationary behaviors are highlighted and a model is proposed for the long-term fading correlation. Finally, a channel model implementation has been developed.

Body Area Networks (BANs) consist of different wireless nodes placed on or in the proximity of the human body. BAN applications encompass various domains such as medicine, surveillance, sport and entertainment. In the last years, significant efforts have been made in BAN radio channel modeling. In particular, the first- and second- order characteristics were investigated in static and dynamic conditions in previous works [1].

In order to characterize the On-body channel, two measurement campaigns were performed at CEA-LETI and at UCL with different human subjects in indoor environments, for various mobility scenarios, antenna locations and polarizations. In [2], we first focused on the signal measured at 4.2 GHz, the center frequency of the UWB lower band, on common radio links between the CEA and the UCL measurement campaigns. Only the measurements performed in walking scenarios with antennas characterized by a normal polarization are investigated.

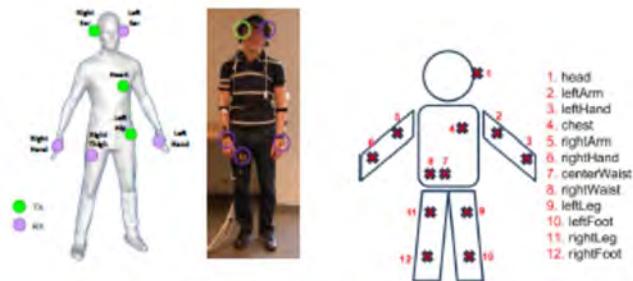


Figure 1: On-body nodes emplacements in measurement campaigns at CEA (left) and UCL (right).

It is well-known that in the power transfer function, one can distinguish slow and fast fading. In BAN communication systems, the long-term fading is mainly due to the movement of the human body that dynamically shadows the communication while moving. This effect is particularly evident when one of the antenna is placed on a limb and can affect the communication reliability.

It has been observed that for walking scenarios for which the subjects walked regularly along a straight line, due to the opposite oscillating movements of the arms, the two radio links are highly anti-correlated. Furthermore, the correlation characteristics are stationary in time.

On the contrary, in the case the subjects followed a random trajectory when walking, the correlation characteristics are non-stationary in time and the correlation value can vary from strong negative to strong positive values.

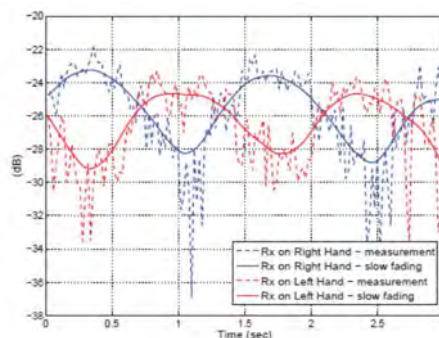


Figure 2: Example of long-term fading in On-body channels (regular walk).

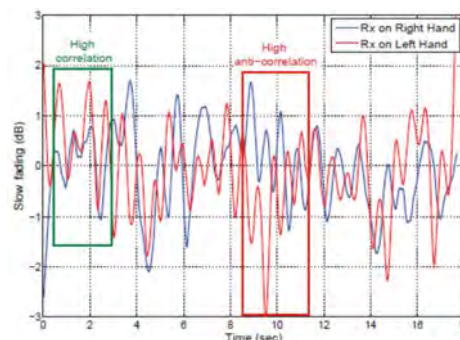


Figure 3: Example of long-term fading non-stationary behavior in On-body channel (random walk).

Being the correlation properties dependent on the observation time and regularity of walk, in [3] a Markov chain model has been proposed to reproduce the variation over time of the space-time correlation. This model can be exploited for cooperative approaches using on-body nodes as relays.

The correlation analysis has been also extended to the 2.4 GHz band based on CEA measurement campaign [4].

An auto-regressive model for long-term was proposed to reproduce the dynamic channel characteristics preserving both the temporal and inter-link correlation. Finally, a Matlab® implementation has been presented [4].

This work by CEA has been partially funded by the French ANR project CORMORAN, the FP7 European Project WiserBAN and the NPRP grant from the Qatar National Research Fund. The collaboration with Prof. C. Oestges is in the framework of the COST IC1004 action.

### Related Publications:

- [1] R. Rosini, "From radio channel modeling to a system level perspective in body-centric communications," PhD thesis, University of Bologna, Italy, May 2014.
- [2] O. Pasquero, R. Rosini, R. D'Errico, C. Oestges, "On-Body Channel Correlation in Various Walking Scenarios", *8th European Conference on Antennas and Propagation (EuCAP)*, pp. 840-844, 6-11 April 2014.
- [3] O.P Pasquero, R. Rosini, R. D'Errico, C. Oestges, "A Correlation Model for Non-Stationary Time-Variant On-Body Channels", accepted for publication in *IEEE Antenna Wireless Propagation Letters*.
- [4] M. Arnesano, R. Rosini, R. D'Errico, "Study and Implementation of Space-Time Correlation for a Dynamic On-Body Channel Model" *IC1004 TD(14)11040*, Krakow, Poland, 24-26 September 2014.

## Radio channel modeling for inter-bodies communications

Research topics: propagation, channel modeling, inter-body communications

R. Rosini, R. Verdone, R. D'Errico

**ABSTRACT:** An indoor Body-to-Body narrowband channel model has been proposed based on experimental data acquired through a real-time dynamic measurement campaign at 2.45 GHz. The radio channel was investigated under different communication conditions, according to the movement performed by some human subjects and to their mutual position.

Body Area Networks (BANs) are a new emerging technology intended to revolutionize peoples' everyday life by offering new services in heal monitoring, sport, leisure, gaming and social networks. Regardless of the application category for which BANs are devised, body communications are evolving from centric approach to networking topologies. BANs would be integrated in the larger context of the Internet of Things (IoT) where devices are directly held by the users.

In this work, we focus on Body-to-Body (B2B) communications, which is the case where at least one node is placed on a human body (possibly being part of a BAN) communicating with one or more nodes located on another body. A narrowband radio channel model for B2B communications at 2.45 GHz is presented. The power transfer function is composed by a channel gain and a small-scale fading contribution, the latter accounting for multi-paths coming from the moving body and the environment. Considering that the body itself can act as an obstacle to the communication, a large-scale fading or body shadowing effect is also defined according to the users' mutual position and orientation. Four scenarios were investigated in order to account for different communication conditions, according to the subjects' mutual position and the movement they performed, as shown in Figure 1. To account for the antenna impact on channel characteristics, all the acquisitions are repeated with two sets of antennas with different radiation properties.

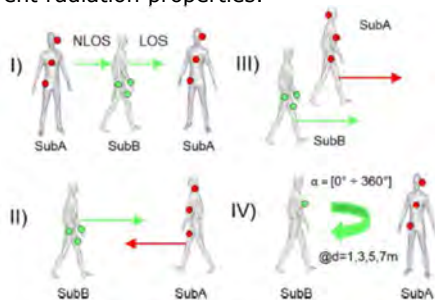


Figure 1: Scenarios for the inter-bodies communications.

According to the movement considered, different channel models have been proposed. For instance, in opposite walks (scenario II), three different distance-dependent path loss models have been identified for Line-Of-Sight (LOS), Non-Line-of-Sight (NLOS) and Transition zones (Figure 2). On the contrary for parallel walks (scenario III), the channel gain along time can be described through its average along time plus the long-term fading.

Experimental results show that the channel gain strongly depends on the specific on-body node location and on the

antenna type. In particular, normally polarized antennas yield to smaller attenuation in NLOS as compared to tangentially oriented ones, because of the higher diffraction around the body. The small-scale fading component is modeled by a Rice distribution, which can be approximated by a Rayleigh one when in NLOS, the latter case being characterized by a more significant multipath contribution. Finally, the large-scale fading is statistically described by a mixture distribution composed of two normal distributions (Figure 3). Results point out that normally polarized antennas are generally less affected by the body presence, showing a less evident two-lobe configuration in the distribution of the body shadowing values.

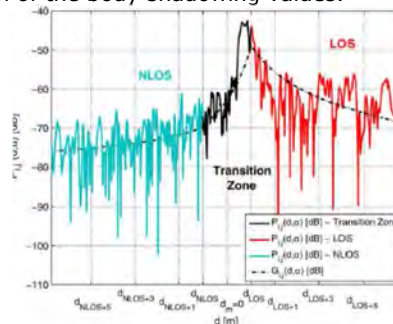


Figure 2: Channel gain extraction for the hip/chest link, opposite walk (scenario II).

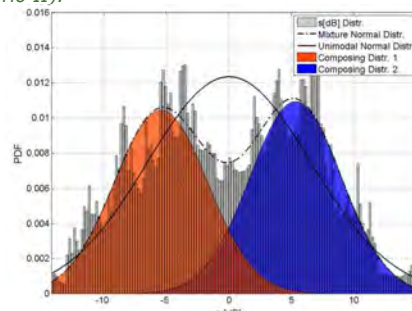


Figure 3: Shadowing probability density function of for the chest/chest link. (scenario IV).

In order to realize PHY Layer solutions, MAC and Network Layers protocols optimized for B2B communications can take advantage of the implementation of the proposed model, which can pave the way to the evaluation of system performance considering realistic radio channel conditions.

This work has been partially funded by the FP7 European Project WisERBAN.

### Related Publications:

- [1] R. Rosini, "From radio channel modeling to a system level perspective in body-centric communications," PhD thesis, May 2014.
- [2] R. Rosini, R. Verdone, and R. D'Errico "Body-to-Body Indoor Channel Modelling at 2.45 GHz", *IEEE Trans. on Antennas and Propagation*, vol.62, no.11, Nov. 2014, pp.5807-5819.

## A V-band switched-beam transmit-array antenna

Research topics: millimeter-waves, integrated antennas, reconfigurable antennas

J. A. Zevallos Luna, L. Dussopt

**ABSTRACT:** A high-directivity switched-beam antenna in V-band is presented and includes a circularly-polarized transmit-array realized in a low-cost printed technology associated with a focal source array integrated on high-resistivity silicon. The measurements show a maximum gain of 12.1 dBi, a 3-dB gain-bandwidth of 57.8–70 GHz and an axial ratio below 5 dB. The antenna exhibits five beams pointing from  $-22^\circ$  to  $+23^\circ$  in one plane, its size of  $25 \times 25 \times 10 \text{ mm}^3$  is compatible with the integration in different multimedia communication devices.

The development of millimeter-wave radio and antenna systems has been very significant recently in perspective of future applications such as wireless communications for high-data rate local area networks, radio access to mobile networks (5G), point-to-point communications, or automotive radars. The 57–66 GHz ISM band attracted most of the attention with the demonstration of fully integrated transceiver systems achieving data rates of several Gigabit-per-second. Due to the high propagation loss occurring in this frequency range, most applications require the design of antenna systems with a high gain and electronic beam steering.

As an alternative to expensive phased-array antennas or bulky dielectric lenses, passive transmit-array antennas associated with in-package integrated focal sources may provide a competitive solution with a good trade-off in terms of reconfigurability, power consumption, efficiency and cost (Fig. 1) [1].

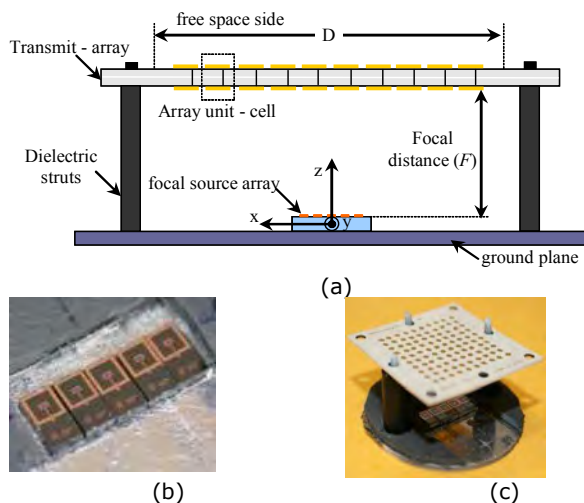


Figure 1: Cross section of a transmit-array fed by a focal source array (a); focal source array (b); photo of the antenna (c).

In this work, the design of the transmit-array builds upon our previous work [2,3] with an improvement of the phase quantization to 3 bits instead of 2 bits to achieve higher directivity and gain. It is made of three metal layers, two low-loss dielectric substrates and a bond ply. It is composed

of  $10 \times 10$  unit-cells ( $25 \times 25 \text{ mm}^2$ ) whose phase distribution is optimized for a maximum gain of 17.1 dBi in the broadside direction when the central element of the focal array is selected. The focal distance is 10 mm only.

The focal array consists of five identical folded-dipole antennas integrated on high-resistivity silicon, each antenna exhibits a gain of 4–7.9 dBi and a return loss below  $-14 \text{ dB}$  over the 57–66 GHz frequency band.

The radiation patterns were measured in an anechoic chamber with a dedicated set-up allowing RF probe feeding of integrated antennas. The measurements are performed by placing the RF probe successively on the input pads of each antenna of the focal array. An excellent agreement between simulations and measurements was obtained. The experimental results show five beams with right-hand circular polarization and a 3-dB beamwidth of  $10^\circ$  to  $16^\circ$  (Fig. 2). Overall, the five beams achieve a coverage of  $65^\circ$  with a minimum gain of 10 dBi. The 3-dB gain bandwidth is 56.6–66.3 GHz (15.9%).

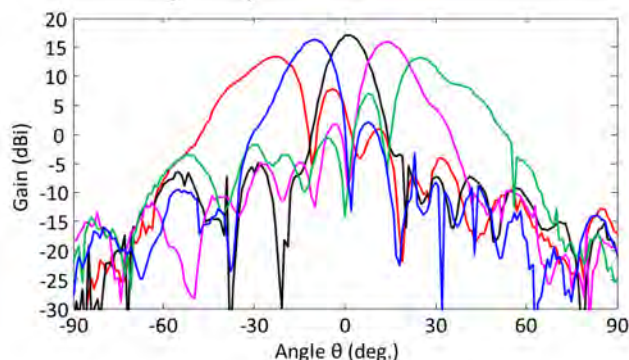


Figure 2: Radiation patterns at 60 GHz with five beams pointing at  $-24^\circ$ ,  $-10^\circ$ ,  $0^\circ$ ,  $+14^\circ$ ,  $+25^\circ$ , with a gain of 13.4, 16.3, 17.1, 15.9, 13.2 dBi, respectively.

The perspectives for this work are the design of fully integrated active focal arrays including a radio transceiver, a beam-switching network, and multiple antenna elements ( $4 \times 4$  or more) in order to achieve 2D beam-steering systems. Another perspective is to scale the system to much higher gain levels, 30 dBi or more to address long range radar or communications applications.

### Related Publications:

- [1] J.A. Zevallos Luna, L. Dussopt, "A V-band Switched-Beam Transmit-array antenna," *Int. Journal on Microwave and Wireless Technologies*, vol. 6, Issue 1, Feb. 2014, pp. 51–56.
- [2] J.A. Zevallos Luna, L. Dussopt, A. Siligaris, "Packaged Transceiver with On-Chip Integrated Antenna and Planar Discrete Lens for UWB Millimeter-Wave Communications," *IEEE Int. Conf. on Ultra-Wideband (ICUWB 2014)*, 1–3 Sept. 2014, Paris, France.
- [3] H. Kaouach, L. Dussopt, J. Lantéri, T. Koleck, R. Sauleau., "Wideband low-loss linear and circular polarization transmit-arrays in V-band," *IEEE Trans. Antennas and Propagation*, vol. 59, no. 7, July 2011, pp. 2513–2523.



## Circularly-polarized transmitarray antenna with sequentially-rotated elements in Ka band

Research topics: millimeter-waves, high-gain antennas

L. Di Palma, A. Clemente, L. Dussopt, R. Sauleau, P. Potier, and P. Pouliguen

**ABSTRACT:** A new design of circularly-polarized (CP) transmitarray antenna for SATCOM applications is presented. The unit-cell is formed by a linearly-polarized (LP) rectangular patch antenna (receiving layer) connected to a CP patch antenna (transmitting layer). The full-wave simulations show an insertion loss level (IL) of 0.2 dB only at 30 GHz with a 1-dB bandwidth of about 9.4%. The sequential rotation of the CP patches has been implemented leading to a significant improvement of the cross-polarization discrimination (XPD) with gain, side-lobe level and efficiency close to the configuration without rotations.

In the last years, transmitarray antennas have been studied and proposed as alternative solutions to phased arrays and reflect-arrays in different fields of applications like SATCOM, point-to-point communications, automotive radars, or imaging systems.

A transmitarray antenna, whose general scheme is shown in Fig. 1, is formed by a receiving layer connected to a transmitting one with a phase shifter matrix. The receiving layer is illuminated by a focal source, a horn antenna for instance, placed at a distance  $F$  from the array surface. Each unit-cell provides the required phase shift compensating the path length between the array and the phase center of the focal source.

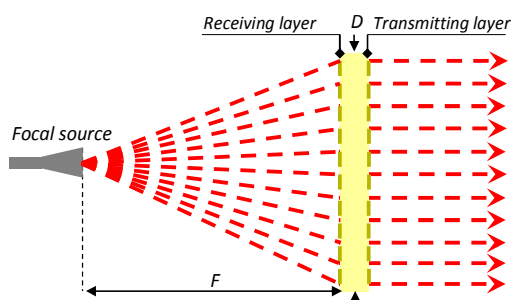


Figure 1: General scheme of a transmitarray antenna.

In this work, a unit-cell is designed to cover the up-link satellite Ka band dedicated to military and commercial applications (29-31 GHz). It is formed by a rectangular patch on the receiving layer and a square patch with truncated corners on the transmitting layer. The geometrical dimensions shown in the inset of Fig. 2a are (in mm):  $L = 5$ ,  $l = 2.6$ ,  $w = 2.9$ ,  $s = 2.7$  and  $t = 1.93$ . The full-wave simulations show an insertion loss of 0.2 dB at 30 GHz with a 1-dB bandwidth of 9.4% (Fig. 2a).

The unit-cell has been used as a building block of a  $20 \times 20$  transmitarray. The design has been carried out by using an in-house code and a proper set of full-wave simulations [1]-[2]. A 1-bit phase compensation of the different path lengths between the phase center of the focal source and each unit-cell is achieved by a  $180^\circ$  rotation of the patch in the receiving layer. The optimal focal distance is 60 mm ( $F/D = 0.6$ , where  $D = 100$  mm is the size of the antenna

panel), and the broadside gain is 24.7 dBi at 30 GHz with XPD of 20 dB (Fig. 2b). The performances of the array are improved by using the sequential rotation as in the case of traditional phased-array antennas. We have considered  $2 \times 2$  sub-arrays of unit-cells with  $0^\circ/90^\circ/180^\circ/270^\circ$  rotated patches [3]. Taking into account these rotations, the phase compensation algorithm gives the optimal phase distribution shown in the inset of Fig. 2b. The broadside gain is 24.4 dBi and the XPD reaches 55 dB at 30 GHz (Fig. 2b).

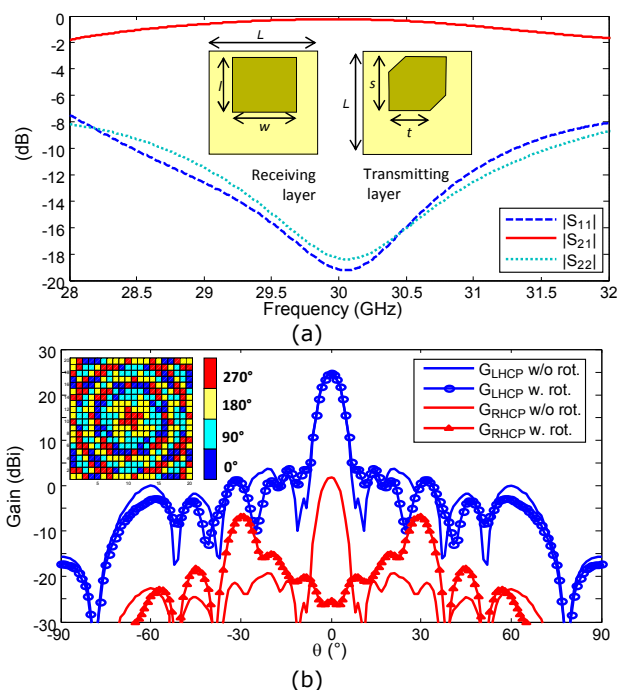


Figure 2: (a)  $S$ -parameters of the designed unit-cell computed with Ansoft HFSS and (b) simulated radiation patterns (realized gains) of a 400-element transmitarray based on this unit-cell without (solid lines) and with (marker lines) sequential rotations in the horizontal planes. Insets: (a) sketch of the unit-cell and (b) phase distribution on the transmitarray with sequential rotations.

### Related Publications:

- [1] H. Kaouach, L. Dussopt, J. Lantéri, T. Koleck, and R. Sauleau, "Wideband low-loss linear and circular polarization transmit-arrays in V-band," *IEEE Trans. Antennas Propag.*, vol. 59, no.7, pp. 2513-2523, Jul. 2011.
- [2] A. Clemente, L. Dussopt, R. Sauleau, P. Potier, and P. Pouliguen, "Focal distance reduction of transmit-array antennas using multiple feeds," *IEEE Antennas and Wireless Propag. Letters*, vol. 11, Nov. 2012.
- [3] L. Di Palma, A. Clemente, L. Dussopt, R. Sauleau, P. Potier, P. Pouliguen, "Circularly polarized transmit-array with sequentially rotated elements in Ka band," *European Conference on Antennas and Propagation (EuCAP)*, The Hague, The Netherlands, 6-11 April 2014.





# 4

## Sensors and systems

*Sensors*

*Signal processing*

## In-flight performance of the Absolute Scalar Magnetometer (ASM) of Swarm mission

Research topics: innovating sensors, 4He magnetometers

T. Jager, J.M. Léger, F. Bertrand, A. Boness, V. Cattin

**ABSTRACT:** The role of the Absolute Scalar Magnetometer (ASM) in the Swarm mission is to deliver absolute measurements of the magnetic field's strength for the in-flight calibration of the Vector Fluxgate Magnetometer (VFM). Vector measurements can be additionally delivered with no impact on the magnetometer's scalar performance and the ASMs have been continuously operated in that mode since the beginning of the mission. Their respective demonstrated performance characteristics during the first year of the Swarm mission are presented.

As the magnetic scalar reference of the ESA Swarm mission, the ASM developed by CEA-LETI with the support of CNES provides continuous absolute measurements of the Earth's magnetic field strength  $B_0$  for the in-flight VFM vector calibration. Given its key role for the mission and considering the required data availability, a cold redundancy of the ASM has been implemented: two complete and independent ASM instruments are flown onboard each of the three satellites of the Swarm constellation.

The ASM is a magnetic field to frequency converter based on atomic spectroscopy of 4He able to deliver scalar measurements with a resolution around 1 pT/ $\sqrt{\text{Hz}}$  independently of the ambient magnetic field amplitude in a 1 Hz sampling (bandwidth DC-0.4 Hz) scalar mode or a 250 Hz sampling (bandwidth DC-100 Hz) burst mode. The in-flight ASM's intrinsic scalar noise level has been confirmed close to 1 pT/ $\sqrt{\text{Hz}}$  in the DC-100 Hz band (Fig. 1), in agreement with on-ground characterizations. The maximum ASM accuracy error after the level 1b corrections is of 65 pT (1  $\sigma$ ) which is well below the 150 pT (1  $\sigma$ ) budget allocated to the instrument.

A vector measurement can be set-up in addition to the scalar one thanks to the superposition onto the ambient field  $B_0$  of three orthogonal vector modulations. A real-time analysis of the scalar field measurements at the modulation frequencies  $f_{mi}$  makes it then possible to derive the orientation of the ambient magnetic field in the vector coils frame. As no perturbation is shown in-flight in the vicinity of the vector modulation frequencies at 8, 11 and 13 Hz (Fig. 1), on-ground settings have been kept for in-flight operation. In this vector mode, the ASM thus delivers both scalar and vector data sampled at 1 Hz and low-pass filtered at 0.4 Hz, without any modification of the scalar data quality and characteristics (i.e. accuracy, resolution, timing) with respect to the one delivered in scalar mode. In addition, scalar and vector measurements are by design perfectly synchronized and correspond exactly to the same spatial location, thus ensuring their perfect coherence. This mode, first developed on an optional and experimental basis for the ASM instrument, has since then become the nominal one in flight.

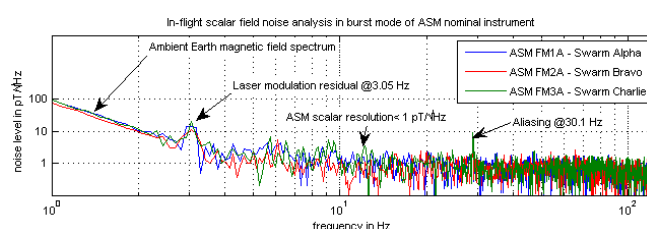


Figure 1: Scalar field noise analysis of the ASM instruments.

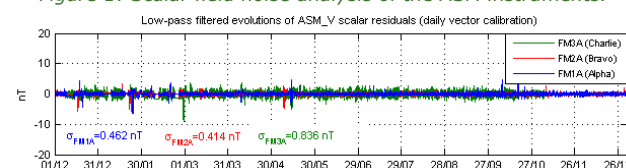


Figure 2: Low-pass filtered ASM scalar residuals obtained with the ASM-V product.

A daily vector calibrated ASM\_V product has been generated for scientific exploitation, and the long term vector measurement behavior has been investigated in relationship with both instrumental and satellite platform environment parameters evolutions. The ASM\_V long term stability illustrated on Figure 2 through the scalar residual evolutions (i.e. the difference between the measured scalar field intensity and the reconstructed vector field modulus), made it possible to evaluate the in-flight mechanical boom stability between the ASM and the VFM instruments. Given the encouraging results of this study, a geomagnetic field model relying only on ASM data has then been produced, a corresponding IGRF candidate model submitted and then integrated as a contributor to the final IGRF-12 model for 2015-2020 demonstrating the interest for the vector measurements provided by the ASM instruments.

Last but not least, for the first time in space, the three satellites of the Swarm mission offer the possibility to compare vector measurements delivered by two different types of instruments. This specific and unique capability can be used to directly cross-check, compare and assess the relative sensors' vector performance, and to build and validate geophysical models with different input datasets.

### Related Publications:

- [1] P. Vigneron et al., "Swarm's Absolute Scalar Magnetometers experimental vector field measurements: first conclusions from comparisons with preliminary nominal Swarm Level1b vector data", *European Geosciences Union General Assembly 2014*, Vienna, Austria, 27 April-2 May, 2014.
- [2] I. Fratter et al., "Swarm absolute scalar magnetometers first in-orbit results", *65th Int. Astronautical Congress 2014 (IAC)*, Toronto, Canada, 29 Sept.-3 Oct., 2014.
- [3] J-M. Léger et al., "In-flight calibration of the experimental Absolute Scalar Magnetometer vector mode on board the Swarm satellites", *47th annual Fall Meeting American Geophysical Union's (AGU)*, San Francisco, CA, 15-19 Dec. 2014.
- [4] G. Hulot et al., "Swarm's Absolute Magnetometer (ASM) experimental vector mode, a unique capability with considerable potential", *47th annual Fall Meeting American Geophysical Union's (AGU)*, San Francisco, CA, 15-19 Dec. 2014.
- [5] P. Coisson et al., "Swarm's Absolute Scalar Magnetometers Burst Mode Results", *47th annual Fall Meeting American Geophysical Union's (AGU)*, San Francisco, CA, 15-19 Dec. 2014.

## Detecting MCG signals from a phantom with a 4He magnetometer

Research topics: innovating sensors, 4He magnetometers

M.-C. Corsi, E. Labyt, W. Fourcault, C. Gobbo, F. Bertrand, F. Alcouffe, G. Cauffet, M. Le Prado, S. Morales

**ABSTRACT:** This paper presents the results obtained with two 4He magnetometers dedicated to magnetocardiography. Since the device operates at room temperature, the distance between the skin and the sensor can be reduced and the measured sensitivity with the gradiometer is compatible with this application. In this study, the possibility of measuring MCG signals with a 4He magnetometer is demonstrated by means of a phantom.

Magnetocardiography (MCG) is a non-invasive technique which consists in measuring the magnetic fields generated by the heart, about one million times smaller than the earth magnetic field. MCG is currently based on the use of Superconductive Quantum Interference Devices (SQUIDs), with a sensitivity of 1-10 fT/ $\sqrt{\text{Hz}}$  (1). Despite its clinical interest, MCG is not widespread in hospitals, because of its costs related to the need of a heavy Magnetic Shielding Room (MSR) and the use of a cryogenic cooling system. 4He magnetometer is a promising device to detect biomagnetic signals without heating or cooling system. Its principle of operation relies on three main physical phenomena: HF (High Frequency) discharge, optical pumping and parametric resonance. Two RFs (Radio-Frequency) fields are respectively applied along the X and Y axis, perpendicularly to the laser polarization, to induce the parametric resonances. The resonant signals obtained through the intensity of the laser crossing the gas cell are directly proportional to the three components of the magnetic field.

The aim of this study is to demonstrate that our device is able to record MCG signals. Here, a pseudo-MCG signal is simulated using a phantom consisting in a simple coil. The signal, injected by a generator, has been obtained from the Physionet Toolkit (2). The coil generates a magnetic field around 70 pT at 7 cm from the sensor along the vertical-Y-axis with a typical QRS shape. Our system, placed inside a 5 layer- $\mu$ -metal magnetic shield, is based on a first-order gradiometer configuration, with two miniaturized magnetometers (Fig.1).

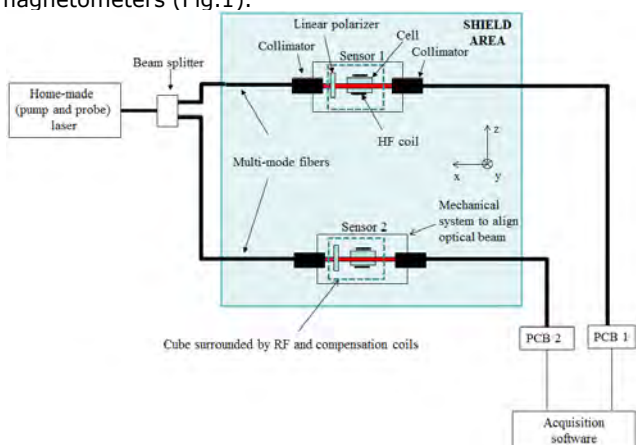


Figure 1: Schematic of the tested configuration.

Each sensor contains a 100-mm<sup>3</sup> cylindrical glass-blown cell filled with 4He. The first sensor, placed 7cm above the phantom, measures the pseudo-MCG signal and the residual magnetic field B, whereas the second one, several 10 cm away, records mainly B. The pseudo-MCG signal of interest is extracted as the difference signal.

Sensitivity of the first-order gradiometer developed is of 1 pT/ $\sqrt{\text{Hz}}$  at 1Hz and below 400 fT/ $\sqrt{\text{Hz}}$  between 10 and 300 Hz (Fig.2).

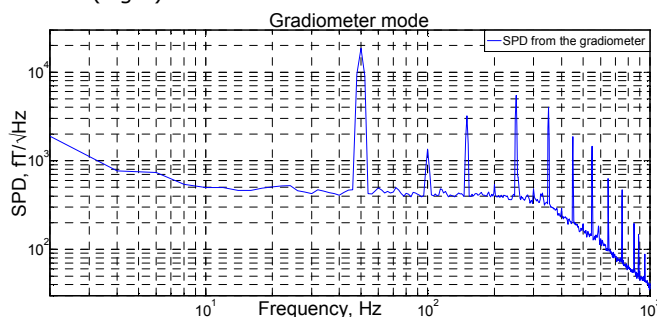


Figure 2: Sensitivity obtained with the gradiometer mode.

After applying notch and bandpass filters, the main components of the cardiac cycle (QRS complex, P and T waves) are clearly recorded, well resolved and exhibit a morphology similar to the simulated MCG signal (Fig.3.).

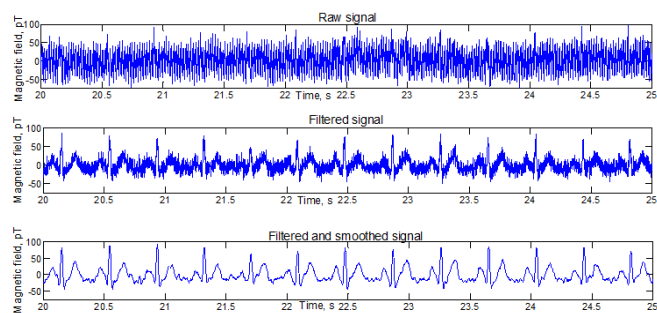


Figure 3: Raw and filtered signals recorded with the gradiometer mode.

A clinical trial has been allowed for MCG and MEG (magnetoencephalography) recordings in healthy subjects. Several improvements of the present gradiometer will be implemented to make it compatible with MEG recordings.

### Related Publications:

[1] M.C. Corsi, E. Labyt, W. Fourcault, C. Gobbo, F. Bertrand, F. Alcouffe, G. Cauffet, M. Le Prado, S. Morales, "Detecting MCG signals from a phantom with a 4He magnetometer", 19th Int. Conf. on Biomagnetism (BioMag 2014), Halifax, Canada, 24-28 Aug. 2014.

## Towards a fully integrated optical gyroscope using whispering gallery modes resonators

Research topics: innovating sensors, optical sensors

T. Amrane, J.-B. Jager, T. Jager, V. Calvo, J.M. Léger

**ABSTRACT:** we present our preliminary results towards using Whispering Gallery Modes Resonators (WGMR) as the sensitive part of an Integrated Optical Resonant Gyroscope (IORG). These resonators have been specifically designed and fabricated in order to achieve the highest possible  $Q \times D$  product ( $7 \times 10^4$ ) corresponding to a shot noise resolution of  $25^\circ/\text{h}$ . The first steps towards system-level characterization are also presented.

Since the developments of lasers and optical fibers in the 70s, the optical gyroscopes have been subject to an intensive research to improve both their resolution and stability performance [1]. However, the best optical gyroscopes currently on the market, the ring laser gyroscope and the interferometer fiber optic gyroscope, are still macroscopic devices and cannot address specific applications where size and weight constraints are critical. One solution to overcome these limitations could be using a WGMR as a sensitive part to build an IORG. To keep a high rotation sensitivity, which is usually degraded when downsizing this kind of optical sensors based on the Sagnac effect, the resonator has to exhibit a very high quality factor ( $Q$ ): as detailed in equation (1) where the minimum rotation rate resolution for an IORG is given as a function of the speed of light in vacuum ( $c$ ), the resonator characteristics ( $Q$  and diameter  $D$ ) and the global system characteristics (i.e. SNR and bandwidth  $B$ ), the higher the  $Q \times D$  product, the lower the resolution.

$$\delta\Omega_{min} = \frac{c\sqrt{2}}{Q \times D} \times \frac{\sqrt{B}}{SNR} \quad (1)$$

Our WGMR are silica disks fabricated on silicon substrate (Fig. 1a). To improve their  $Q$ -factors, the standard fabrication process flow has been modified with the addition of specific steps to decrease the surface roughness at the edge of the disk, and a dry oxidation step was also added to reduce optical losses in the silica layer [2].

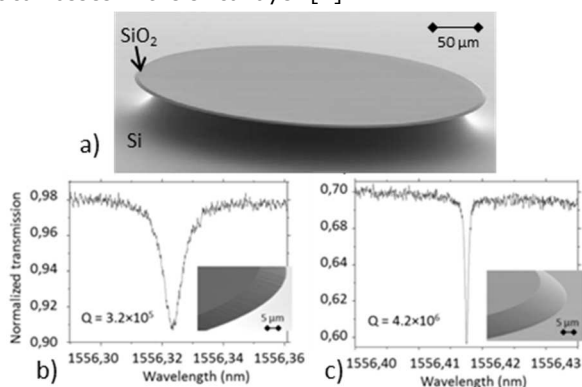


Figure 1: a) SEM picture of a 400- $\mu\text{m}$  diameter  $\text{SiO}_2$  disk. a) Transmission spectra across a resonance for the non-optimized process and b) roughness-optimized fabrication process.

On the fabricated sample shown in Fig.1, the resonance peak for an optimized  $\text{SiO}_2$  disk edge interface roughness (Fig. 1c) thus shows a  $Q$  factor 10 times higher than the one obtained on a standard  $\text{SiO}_2$  disk (Fig. 1b).

The highest  $Q \times D$  product obtained with these structures is currently of  $7 \times 10^4$  [3], which is in the range of the current state of the art for resonators used in IORG. With these characteristics and a SNR of 145 dB the current minimal rotation resolution is evaluated to  $25^\circ/\text{h}$ .

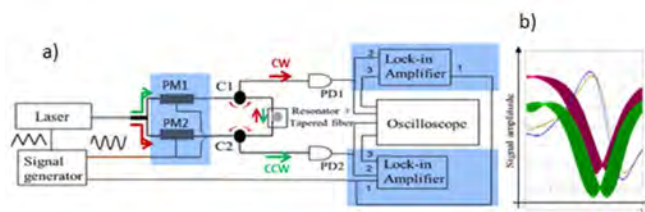


Figure 2: a) The first system test set-up (PM1,2: Phase Modulators. C1,2: circulators. PD1,2: Photodetectors). b) Resonant peaks (green and magenta) and their respective demodulated signals (blue and yellow).

In IORG, the rotation rate measurement is achieved through the measurement of the Sagnac frequency shift between Clock-Wise (CW) and Counter Clock Wise (CCW) resonator spectra characteristics [1]. To get first CW and CCW signal characterizations, we have built a test set-up around the  $\text{SiO}_2$  disks detailed in Fig. 2a. To ensure the mechanical stability of the optical coupling with the resonator, a low refractive index polymer is used to encapsulate both the optical fiber coupler and the  $\text{SiO}_2$  disk. The optical system can thus be rotated without modification of its optical properties and a mechanical protection is provided to the sensing part.

Figure 2b shows the intrinsic CW and CCW rotation sensitivity derived from a wavelength scan performed over 50  $\mu\text{m}$  around one resonance peak of a  $\text{SiO}_2$  resonator. Spectral responses are presented for wavelength-modulated CW (green) and CCW (magenta) input signals. The corresponding wavelength-demodulated signals are also given (CW (blue) and CCW (yellow)) from which a rotation rate sensitivity in the range of 5-60  $\text{Hz}/^\circ/\text{s}$  can be derived for WGMR with diameter from 500  $\mu\text{m}$  to 5 mm and a  $Q$  factor in the  $10^5 - 10^6$  range. These figures will be improved by several orders of magnitude with higher resonator quality factors currently under development.

#### Related Publications:

[1] T. Amrane J.-B. Jager T. Jager V. Calvo J.-M. Léger, "Towards a fully integrated optical gyroscope using whispering gallery modes resonators", *International Conference on Space Optics (ICSO)*, Tenerife, Spain, 7-10 Oct. 2014.



## Adaptable self-powered flexible force sensors

Research topics: innovating sensors, piezoelectric nanowires, system integration

E. Pauliac-Vaujour, S. Salomon, A. El Kacimi

**ABSTRACT:** Integration-driven approaches to the design of novel adaptable sensors and systems enable sensor performances to be optimized for the targeted applications and final integration configurations. We developed dedicated models, fabrication techniques and electronics for a highly flexible strain sensor which exploits the piezoelectric properties of Gallium Nitride (GaN) wires. With typical force sensitivities of 30 mV/N, our GaN-based device nears skin sensitivity to a light touch. By adjusting the sensor design and integration, we aim to demonstrate its capabilities for other application fields, such as structural health monitoring (SHM).

With sensor miniaturization and the fast-spreading of flexible electronics, challenges that lay ahead for future system integration are plethora. In addition to improving sensor performances, autonomy has become a major issue, tackled by the emergence of self-powered and wireless/contactless communication systems.

New forms of systems are required in order to implement such fundamental changes. Smart materials can be considered as a provider of new sensing functions, new physical characteristics (flexibility) and new energy management schemes. In the present work, we develop a force sensor based on very long, flexible, single crystal piezoelectric GaN nanowires for the self-activated dynamic detection of deformations.

Multi-scale multi-physics FEM models were used to design a capacitive unit sensor including the active piezoelectric material (GaN-wire/polymer composite). Analysis of the sensor piezoelectric response to deformation enabled to determine the optimum wire morphology and position within the cell, as well as the optimum material layer characteristics. Analytical models confirmed that, at small deformations, the figures of merits of such specific high quality materials compared well with concurrent technologies used, for example, in SHM (PVDF and metal gauges) or electronic skin (MEMS) applications.

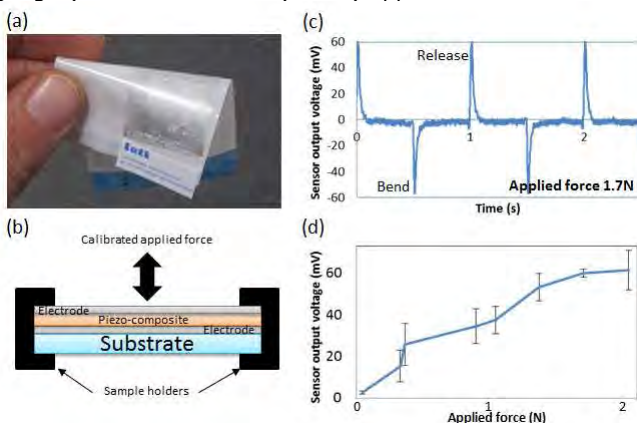


Figure 1: (a) photograph of the flexible sensor; (b) measurement setup; (c) bend and release signal generated upon a 1.7 N force; (d) measured outputs within the 46 mN to 2.3 N force range.

Our capacitive structures of a piezo-composite stacked between two thin-film electrodes was fabricated in CEA's cleanrooms using (i) standard thermal evaporation of metal and polymer on flexible substrates and (ii) a dedicated Langmuir-Blodgett deposition technique enabling a controlled assembly of the GaN wires to match the simulated sensor design [1].

Bending tests were carried out on a clamped substrate instrumented with our 6  $\mu\text{m}$ -thick sensor of active area 1.5  $\text{cm}^2$ , which corresponds to approximately 1.5 million wires. For curvature radii in the cm range (up to 0.02% strain) and applied forces ranging from 46 mN (2 kPa) to 2.3 N (100 kPa), piezoelectric potentials from 4 to 80 mV were measured, with an average sensitivity of 30 mV/N (Fig. 1).

Such results highlight the potential of this technology for electronic skin applications, for example. Additional FEM simulations may be carried out for the purpose of exploring the detection limits of several configurations of sensors. In the example below (Fig. 2), we aim to demonstrate the impact of the wire-sensor structure and integration position on measuring the deformation of a bent cantilever. This study highlights the importance of controlling the wire morphology and assembly within the sensor unit cell depending on the integration constraints [2].

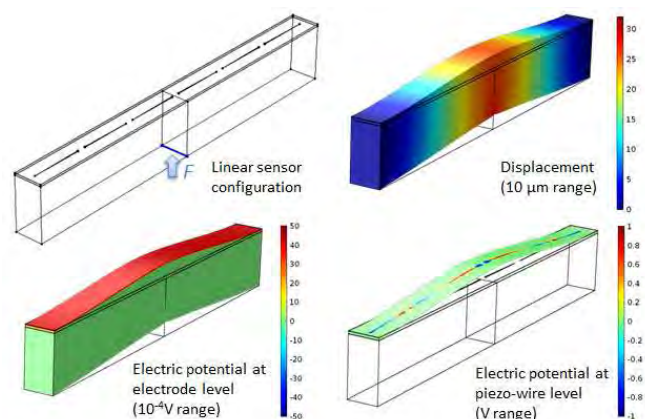


Figure 2: FEM model of the potential response of a simplified 6-wire linear sensor configuration.

### Related Publications:

- [1] S. Salomon, J. Eymery, E. Pauliac-Vaujour, "GaN wire-based Langmuir-Blodgett films for self-powered flexible strain sensors", *Nanotechnology* 25 (2014) 375502.
- [2] E. Pauliac-Vaujour, S. Salomon, J. Eymery, E. Leon Perez, "Self-powered conformable deformation sensor exploiting the collective piezoelectric effect of self-organized GaN nanowires", *7<sup>th</sup> European Workshop on Structural Health Monitoring (EWSHM 2014)*, Nantes, France, 8-11 July 2014.

## Unit cell design of a force sensing device based on vertical piezoelectric nanowires

Research topics: innovating sensors, piezoelectric nanowires

E. Pauliac-Vaujour, E. Leon Perez, J. Brivio

**ABSTRACT:** Multi-physics static finite-element (FEM) simulations of a piezoelectric force sensing device unit-cell (pixel) based on an individually-contacted vertical ZnO nanowire (NW) are performed to establish reliable guidelines for a better tolerance to micro-fabrication process variability. A parametric study of the pixel piezo-response as a function of the ZnO seed layer thickness and the topography of the electrode-NW contact shows that, for instance, the collection efficiency, i.e. the ratio of piezo-potentials in the electrodes and the NW, is higher for thin ZnO layers (up to 69% for a 5 nm thickness) but drops down to 33% for a small spacing between the NW and the electrode (3 nm).

In the past 10 years, interconnected arrays of ZnO piezoelectric nanowires (NWs) have been implemented as efficient energy harvesters for new generations of self-powered devices, mainly by Wang's team in Georgia Tech. Such systems may also be exploited to design high sensitivity and high resolution force sensors with pixels as small as a single NW. However, pixel fabrication raises the issues of (i) sub-100nm processing of specific materials (ZnO seed layer), (ii) controlled NW growth on processed chips and (iii) efficient local and remote charge collection.

We developed an FEM model which considers the full pixel architecture and evaluates both the generated piezo-potential profile within the NW ( $V_{nw}$ ) and the actual collected signal ( $V_{contact}$ ). The collection efficiency ( $V_{nw}/V_{contact}$ ) can be estimated as a function of actual fabrication variables such as, for example, the seed layer thickness ( $t$ ) or the NW-electrode spacing ( $d$ ).

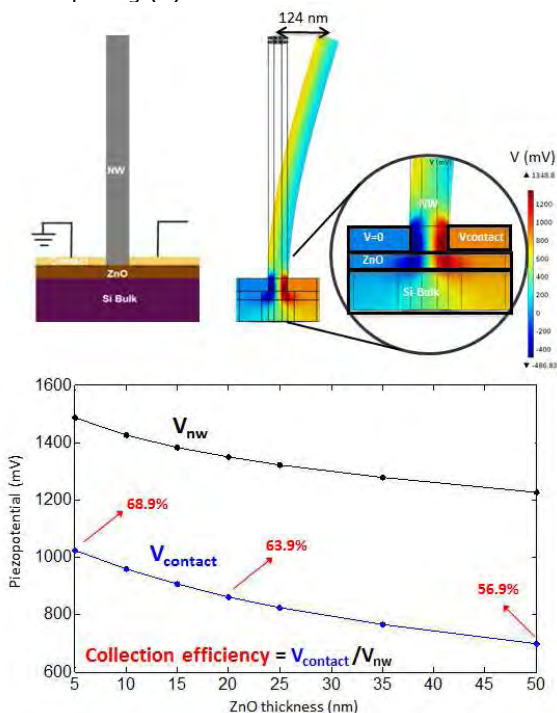


Figure 1: Parametric study of the piezo-response of a NW-pixel as a function of the ZnO seed layer thickness.

For deformations within the linear regime (deflection of the order of the NW diameter), maximal values of generated piezo-potential of 1.2 to 1.6 V were calculated at the base of the bent NW, where the contacts are preferably located. For a perfect NW-electrode contact ( $d = 0$ ), collection efficiencies of about 60% are obtained for realistic seed layer thicknesses ( $t \sim 20$  nm), with a slow decrease towards higher thicknesses. However, a 30% drop in efficiency is observed when the NW-electrode contact is discontinued by a few nm, highlighting the extremely small tolerance towards contact topography variability for such devices.

Other parameters such as the nature of the underlying material stack or the electrode characteristics were also investigated. In its primary version, the model takes into account the static electrical and morphological characteristics of the different materials within the pixel. Further studies are being conducted to include also crystallographic and charge transport considerations.

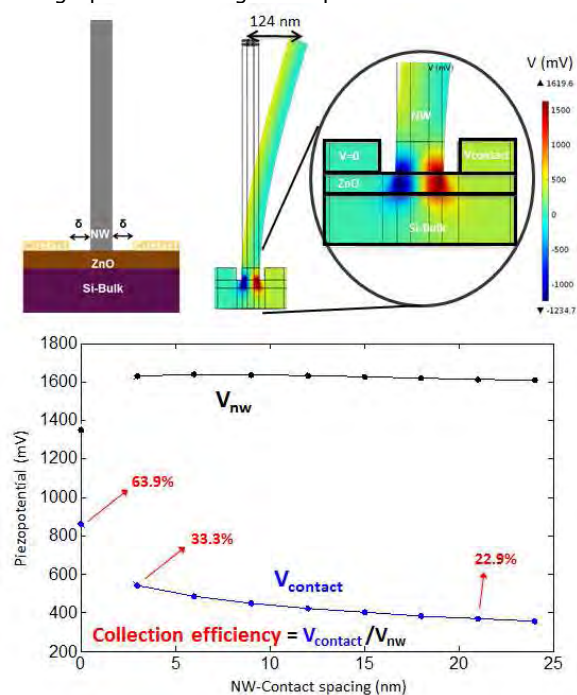


Figure 2: Parametric study of the piezo-response of a NW-pixel as a function of the spacing between the NW and the metallic contacts.

### Related Publications:

[1] E. Leon Perez, M. Mouis, S. Salomon, G. Ardila, E. Pauliac-Vaujour, "Unit-cell design of a force sensor device based on vertical piezoelectric nanowires", *NanoGenerators and PiezoTronics conference*, Atlanta, GA, 9-11 June 2014.

## Surface reconstruction via inertial sensors for monitoring

Research topics: sensor networks, shape capture, geometric modeling

N. Saguin-Sprynski, L. Jouanet

**ABSTRACT:** For several years, CEA-LETI developed Morphosense, a physical ribbon-like device instrumented with attitude sensors. The combined use of accelerometers and magnetometers allows Morphosense to provide its spatial orientation along the curve followed by the ribbon. Several methods of interpolation of these tangential data have been developed, with which one can reconstruct the shape of the ribbon. Here, we focus on a new demonstrator called MorphoShape, a smart textile equipped with inertial sensors and a set of algorithms allowing to reconstruct the shape of the textile along time.

The goal of this work is to introduce new kinds of instrumented materials. We consider for example plastic or textile surfaces, which will be equipped with arrays of sensors in order to provide new functionalities. The alliance between instrumented materials and mathematical algorithms will allow materials to get some knowledge about their own shape, introducing what we could call proprioceptive materials. These smart materials could then become useful for monitoring structures as bridges or dams.

In the following, we first describe the context of the shape capture and the interest for the Structural Health Monitoring (SHM).

Having a smart surface brings a huge set of capabilities in the domain of SHM. Indeed, the structural health monitoring consists in detecting evolutions or modifications of structures, and following their shape can then bring a new modality for monitoring these structures. This monitoring can be declined in two options: either as new monitoring tools, in deploying our smart system for special test sessions; or in integrating the sensors directly in the structures in order to have a permanent monitoring of the structure. Thereby, the methodology for using shape capture for SHM can be as following: for a defined structure, we first determine the required parameters to be monitored according to the shape we must follow in order to define the instrumentation needed (number of sensors and their modality, acquisition frequency, size of the system, integrated to the structure or specific external tool). Then, we can provide the shape or some specific parameters along time that may detect first signs of failure.

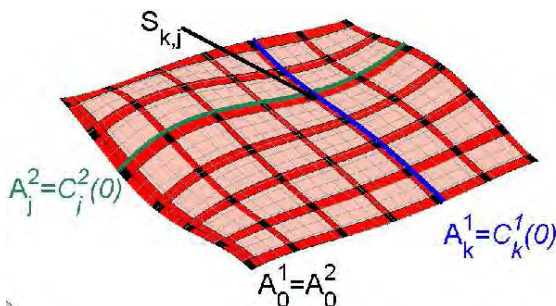


Figure 1: General description of the surface and sensors squared distributed.

Our first MorphoShape is composed of nine sensors 3A3M (three axes of accelerometers, and 3 axes of magnetometers), distributed in a squared mesh (3 by 3), and separated by about 125 mm. A linear circuit in "S" shape interconnects every node and is directly in the textile. The sensors are read via a SPI serial bus, which allows a lot of sensors. The serial bus is connected to a microcontroller controlled by a software driver, allowing to communicate with the surface, modifying some parameters and sequentially read all sensor values. The system sends the data to the host computer via a Bluetooth connection. In this version, the surface is connected to a power supply, but a battery could be used as well.

We have to acquire a surface via a set of sensors organized in a squared mesh laid on it. As it does not exist an intrinsic parameterization for surfaces (contrary to the curves with the arc-length parameter), we will keep the linear organization of sensors, thus the surface can be known by two families of curves in two complementary directions, where sensors are at the intersections, so that we have a tensorial topology of the surface. We consider the following reconstruction strategy. At each time position:

1. we reconstruct the 3D-curves from sensors data and length constraints,
2. these curves are adjusted according to the squared structure by translating their starting point,
3. then the curves are modified to create a closed mesh, because numerical computation and sensors errors make the mesh not strictly closed,
4. finally, the surface is filled by a standard cubic Coons process.

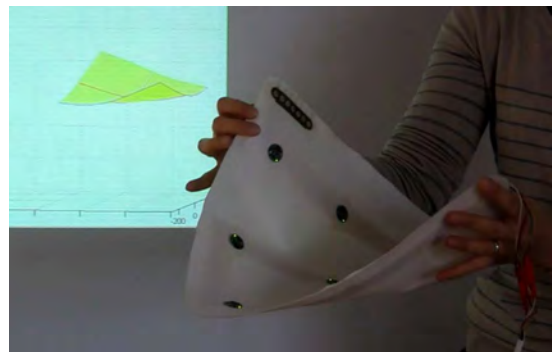


Figure 2: MorphoShape foreground and virtual surface background.

#### Related Publications:

[1] N. Saguin-Sprynski, L. Jouanet, B. Lacolle, L. Biard, "Surfaces reconstruction via inertial sensors for monitoring", 7<sup>th</sup> European Workshop on Structural Health Monitoring (EWSHM 2014), Nantes, France, 8-11 July 2014.



## Passive acoustic sensor network localization: Application to structural geometry monitoring

Research topics: sensor networks, passive identification, geometry monitoring

R. Vincent, M. Carmona, O. Michel, J-L. Lacoume

**ABSTRACT:** Passive acoustic sensor network localization can be applied to geometry structural monitoring by passive propagation delay estimation, defined here as the retrieval of an inter-sensor propagation delay, using uncontrolled ambient sources in a homogeneous acoustic propagation medium. Our approach relates to passive linear systems identification through the use of ambient noise correlations to form estimators. Practical performances of such estimators and two approaches for geometry monitoring of a steel beam are presented.

Propagation delay estimation is a fundamental topic for several applications such as Structural Health Monitoring (SHM) and Sensor Network Localization (SNL). Indeed, monitoring can be achieved by relating the variations of a single inter-sensor propagation delay to the variations of structural properties, via an adequate model of the structure. Secondly, provided that the propagation velocity of the wave is known, SNL can be achieved via an inversion of the model relating inter-elements distances to the sensor positions.

In this work, SNL in aerial acoustics has been used for SHM purposes: to retrieve the Young modulus, bending and shape of a beam. To this end, microphones are distributed at the surface of the structure. Identification of the beam was thus conducted by processing acoustic pressure fields that were propagating mostly around and outside the said structure, as opposed to mechanical displacements [1].

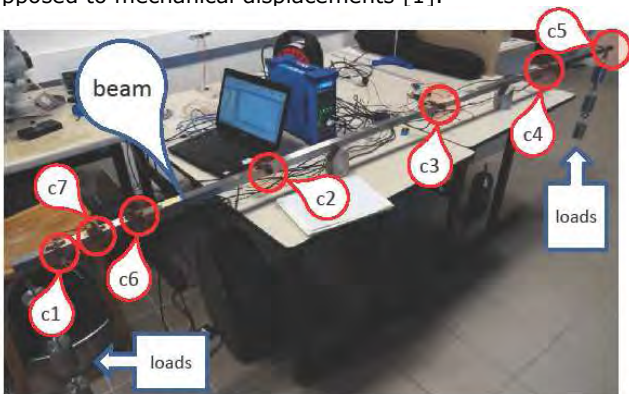


Figure 1: Experimental setup. Microphones along the beam are used to monitor the Young modulus as the beam is being loaded.

Additionally, this study was conducted using opportunity sources only. Such sources are defined as sources that are uncontrolled, thus preventing the direct estimation of the inter-sensor distance with classical approaches (TDOA, RSSI, AOA). Indeed, examples of fields that were used for passive identification purpose are micro seismic vibrations, thermal noise, coda waves. Exploiting opportunity sources to estimate parameters of a propagation medium is labeled passive identification, output-only identification or seismic interferometry, depending on the field of research. Unlike active methods (GPS, optical devices, marker based techniques), passive methods do not require any additional

equipment to the sensor network, nor the structure to be temporarily put out of order.

In order to perform inter-sensor distance estimation, our approach consists in estimating the Green's function between two sensors and extract the propagation delay. In the passive context, the Green's function is estimated from the correlation of propagating noises, that performs the estimation of the Green's correlation function.

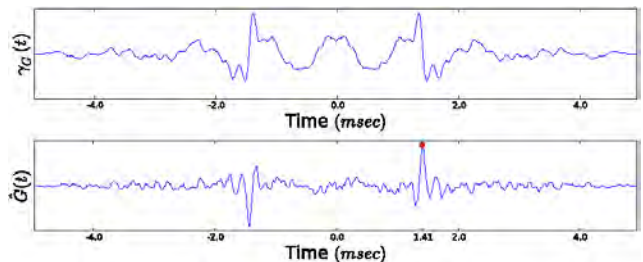


Figure 2: Results of passive Green's function retrieval. (top) Green's correlation function is estimated from the correlations of coda waves. (bottom) Green's function is retrieved from the Green's correlation function. The propagation delay between the two sensors is extracted (red dot) by locating the maximum amplitude.

It appears that passive propagation delay estimation in aerial acoustics is performed with a very good resolution ( $\sim 1\text{cm}$ ), which corresponds to the size of the sensors. Further work will investigate the passive localization of a buried/embedded sensor network.

	c1	c2	c3	c4	c5	c6	c7
c1	0	60+0.4	140-0.1	220-0.1		20+1.3	10+0.6
c2		0	80+1.6	160+0.2	220+0.5	40-0.6	50-0.3
c3			0	80+0.3	140+0.6	120+0.1	130+0.7
c4				0	60+0.7	200+0.4	210-1.1
c5					0	260-0.7	270-1.4
c6						0	10-0.1

Figure 2: Results of the passive inter-sensor distances estimation. All estimations are successful but one, which does not prevent the reconstruction of the sensor network geometry. The estimated distances display an error that is of the same order of magnitude than the dimensions of the sensors themselves ( $\sim 1\text{cm}$ ).

### Related Publications:

[1] R. Vincent, M. Carmona, O. Michel, J-L. Lacoume, "Passive acoustic sensor network localization; application to structural health Monitoring", *European Workshop on Structural Health Monitoring*, Nantes, France, 8-11 July 2014.



## A new approach for motion capture using magnetic field: models, algorithms and first results

Research topics: sensor networks, motion capture, sensor fusion

S. Aloui, C. Villien, S. Leseq

**ABSTRACT:** Indoor and outdoor applications such as sports and health monitoring as well as realistic 3D movie and game animations require low-cost light-weight wearable systems with ambulatory motion capture. We investigated a new approach for ambulatory human motion capture, featuring a body mounted magnetic field source and magnetic field sensors together with an estimation algorithm. A complete study of the model, the hardware, and the estimation algorithms are presented with experimental results in the context of motion capture of human upper limbs.

The human body is considered to be a very complex mobile structure whose precise model is too costly to be run online with low-cost computational platforms. In order to avoid this computational burden, the body is usually represented with a set of  $n$  rigid limbs connected with joints. This structure is an open-loop articulated chain and a specific mechanical representation has to be used. Furthermore, an appropriate indexing of the limbs allows a proper estimate of the pose for the whole articulated chain.

The articulated chain can be mathematically described using graph theory with a rooted tree of  $n + 1$  vertices.

Vertex  $V_0$  (root of the tree) represents a static reference that can be either a specific limb or an external reference. Vertices  $V_i$ ,  $i \in \{0 \dots n\}$  represent the limbs of the body. The choice of  $V_1$  is application-dependent but in full body motion capture, the hip is generally chosen. The joint  $J_i$  of vertex  $V_i$  is the articulation that links limb  $i$  to its parent.  $F_0$  is the reference frame assigned to  $V_0$ .  $F_i$ ,  $i \in \{0 \dots n\}$  is assigned to vertex  $V_i$  and its origin is located at  $J_i$ .

Let  $\mathbf{p} \in R^n$  be the vector of parents such that coefficient  $[\mathbf{p}]_j$  is the index of the parent of  $V_j$  where

$$\forall j \in \{0 \dots n\}, [\mathbf{p}]_j < j$$

An appropriate choice of the indexing of vertices provides a factorization of some calculations while dealing with the measurement model. In a rigid articulated chain, the origin of joints expressed in the reference frames of their parents are known. Thus, only the position of the root limb and the orientation of each limb against its parent are required to reconstruct the chain in 3D space. This hypothesis is not restrictive as the length of limbs can be either set manually or estimated in a calibration phase.

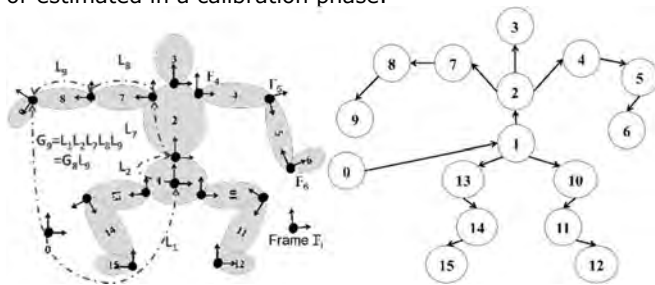


Figure 1: description of the human body model.

In this work, an algorithm derived from the Levenberg Marquardt optimization algorithm (LMA) is used and its results are compared with the ones obtained with an Extended Kalman Filter (EKF) and an Unscented Kalman Filter (UKF). These three algorithms are based on the Bayesian inference model for which two phases are required:

- A prediction phase using the state model;
- An update phase using the measurement model.

The model proposed in this paper is composed of a linear state function and a nonlinear measurement function. Assuming that at the end of step  $t$  the state vector  $\mathbf{x}_t$  is a Gaussian random variable with mean  $\mathbf{x}_{t|t}$  and covariance  $\mathbf{P}_t$ , the propagation of this variable through the linear state function produces a Gaussian variable with mean  $\mathbf{x}_{t+1|t} = \mathbf{F}\mathbf{x}_{t|t}$  and covariance matrix  $\mathbf{P}_{t+1|t} = \mathbf{F}\mathbf{P}_{t|t}\mathbf{F}^T + \mathbf{Q}$ .

The EKF, UKF and the LMA algorithms use this transformation to predict the state at time  $t + 1$  for given measurements up to time  $t$ .

The update step is used to estimate the posterior probability distribution of the state. This distribution is assumed to be Gaussian with mean  $\mathbf{x}_{t+1|t+1}$  and covariance matrix  $\mathbf{P}_{t+1|t+1}$ . The measurement at time  $t + 1$  is also assumed to be Gaussian, with mean  $\mathbf{z}_{t+1}$  and covariance matrix  $\mathbf{R}_{t+1}$ . The prior distribution is assumed to be non-correlated with the measurement distribution. From these assumptions, the mean of the posterior distribution can be estimated by minimizing the following cost function:

$$\mathbf{x}_{t+1|t+1} = \underset{\mathbf{x}_{t+1|t+1}}{\operatorname{argmin}} \left( \begin{bmatrix} h(\mathbf{x}_{t+1|t+1}) - \mathbf{z}_{t+1} \\ \mathbf{x}_{t+1|t+1} - \mathbf{x}_{t+1|t} \end{bmatrix}^T \begin{bmatrix} \mathbf{R}_{t+1}^{-1} & 0 \\ 0 & \mathbf{P}_{t+1|t}^{-1} \end{bmatrix} \begin{bmatrix} h(\mathbf{x}_{t+1|t+1}) - \mathbf{z}_{t+1} \\ \mathbf{x}_{t+1|t+1} - \mathbf{x}_{t+1|t} \end{bmatrix} \right)$$

The objective is to find  $\mathbf{x}_{t+1|t+1}$  that minimizes the square error with both prediction and measurement while using, respectively, the inverses of their covariance matrices as weights.

Tests have been conducted on the motion capture of upper limbs. The first results have shown that embedding both the magnetic source and the magnetic sensors on the body is a valuable motion capture solution even with low power emissions, since the distance between the source and the sensors is small enough to guarantee a good signal over noise ratio (where "good" depends on the application).

### Related Publications:

[1] S. Aloui, C. Villien, S. Leseq, "A new approach for motion capture using magnetic field: models, algorithms and first results", *Int. Journal of Adaptive Control and Signal Processing*, vol. 29, no. 4, March 2014, pp. 407-426.

## Optimal control and sensitivity analysis of a building using adjoint methods

**Research topics: sensor networks, building monitoring, optimal control**

**N. Artiges, F. Vial, A. Nassiopoulou, B. Delinchant**

**ABSTRACT:** Optimal control techniques can actively maximize buildings efficiency by a smarter HVAC systems operation. All these techniques involve a model of the controlled system and an optimization process based on a cost function. The main challenge is to find an accurate model of a system with the right data for training and on-line operation. This work focus on an adjoint-based method for the fast computation of an optimal predictive command law, using a descriptive thermal model of a test case. This method offers analysis opportunities (sensitivity analysis of optimal control) to identify most influential inputs and parameters in final performances, and specify instrumentation systems for model identification.

Recent evolutions in embedded informatics, sensor networks and wireless sensor networks, communication protocols dedicated to buildings applications (LonWorks, KNX, Zigbee...) have fostered the evolution of Building Management Systems (BMS). These techniques make buildings smarter, fully monitored and computer controlled. All these improvements open new ways to control HVAC equipments in buildings, such as Model Predictive Control (MPC).

A Model Predictive Control strategy can be formulated as an optimization problem that aims at reducing energetic consumption by anticipating thermal dynamics and energetic gains while preserving thermal comfort.

The main drawback of this method lies in the computational cost and need of an accurate model and accurate predictions of its solicitations. A standard way to solve this problem is to use model identification techniques, but they can be quite hard to implement when the number of parameters is high. Some sensitivity studies were performed by simulation and energetic models to identify what parameters are the most influential. However, identification techniques are not currently used to identify most critical parameters in an optimal control strategy.

In this work, we developed an optimal control strategy with a low computational cost using adjoint methods. This approach can lead to sensitivity indices related to the optimal control problem.

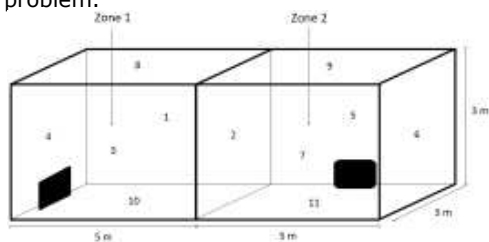


Figure 1: Two rooms test case.

Our test consists in a two rooms building, each room provided with an electric heater and a window (Fig. 1). Our numerical model is a Partial Differential Equations (PDE) system that comes from an application of the heat equation according to standard multi-zone assumptions.

The control strategy aims at minimizing a quadratic cost function modeling a tradeoff between future electric consumption and future comfort:

$$J(u) = \inf_{u \in U} J(u)$$

$$J = \frac{1}{2} \sum_{z=1}^{N_z} \int_0^{t_n} a_z(t) P_z^2 dt + \frac{1}{2} \sum_{z=1}^{N_z} \int_0^{t_n} b_z(t) (T_{op,z}(u) - T_{op,z}^c)^2 dt$$

The minimization of this cost function is performed by a gradient descent technique. The gradient is computed with the adjoint method. This method is the most efficient to compute such gradients since it requires the computational cost of two model simulations only.

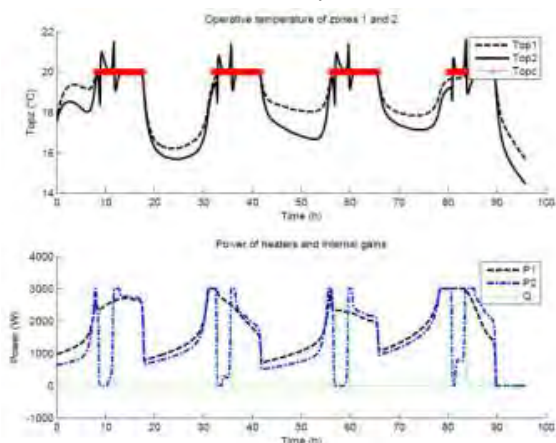


Figure 2: Anticipative optimal control.

Computed gradients can also be seen as sensitivity measures of model parameters. We can use them to compute sensitivity indices that represent their influence in the optimal control process. Knowing the most influent parameters is very helpful to design instrumentation systems for model calibration and monitoring.

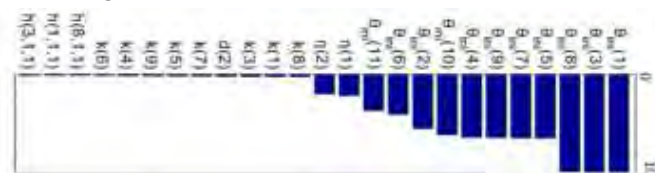


Figure 3: Sensitivity indices for optimal cost function.

**Related Publications:**

[1] N. Artiges, A. Nassiopoulou, F. Vial, B. Delinchant, "Optimal control and sensitivity analysis of a building using adjoint methods", *Building Simulation and Optimization (BSO 2014)*, London, UK, 23-24 June 2014.



# 5

# Energy

*Energy harvesting*  
*Battery Monitoring Systems*

## Electrostatic and piezoelectric bimetal-based thermal energy harvesters - power supply of battery-free wireless sensor nodes

Research topics: energy harvesting

S. Boisseau, A.B. Duret, S. Monfray (ST), J. Boughaleb (ST), A. Arnaud (ST), T. Skotnicki (ST)

**ABSTRACT:** In this work, we investigated innovative thermal energy harvesters turning thermal gradients into electricity in a two-step conversion involving (i) a curved bimetallic strip converting thermal gradients into mechanical oscillations and (ii) a piezoelectric or an electrostatic converter turning the resulting oscillations into electricity. The energy harvesters combined to a power management circuit have enabled to supply a wireless sensor node (GreenNet platform from STMicroelectronics) without battery.

Thermal energy is lost by many systems: motors, pumps, hot pipes, electrical distribution, electronic components, etc. This energy can be exploited to supply small and low-power devices such as Wireless Sensor Nodes (WSN) monitoring the devices on which they are installed. Yet, thermal energy conversion into electricity to supply WSN remains a challenge.

We introduce here new thermal energy harvesters turning heat fluxes into electricity in a two-step conversion involving a thermal-to-mechanical conversion (curved bimetallic strip) followed by a mechanical-to-electrical conversion (piezoelectric or electrostatic transducer).

Curved bimetallic strips are made of two metals with different coefficients of thermal expansion (CTE) joined together (Fig. 1a). Such bimetal strips have long been used as thermal actuators, i.e. to turn temperature changes into fast mechanical displacements (snapping) using buckling effects. Curved bimetallic strips are then capable of switching between two mechanical states according to the temperature and with a hysteretic behavior (snapping and snapping back). Then, when they are inserted in a cavity with a hot lower plate and a cold upper plate, curved bimetallic strips turn the thermal gradient into mechanical oscillations (Fig. 1a,b).

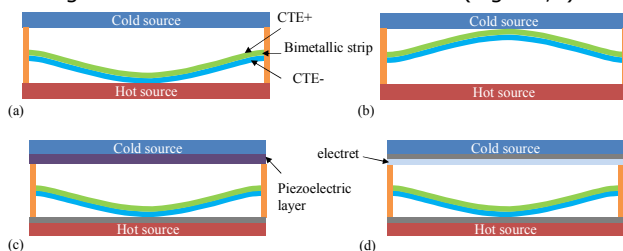


Figure 1: (a) bimetal-based heat engine - lower state, (b) bimetal-based heat engine - upper state, (c) piezoelectric conversion (d) electret-based electrostatic conversion.

Mechanical oscillations can finally be turned into electricity by a piezoelectric material (Fig. 1c) or an electret-based electrostatic converter (Fig. 1d). Both conversion processes have been implemented and have provided output powers in the  $\mu\text{W}/\text{cm}^2$  range (Fig. 2).

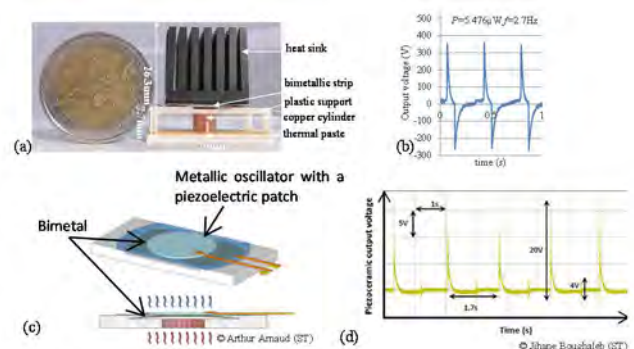


Figure 2: (a) electrostatic conversion and (b) output voltages; (c) piezoelectric conversion and (d) output voltages.

Thermal energy harvesters have been parallelized and connected to a power management circuit implementing a Synchronous Electric Charge Extraction (Fig. 3a): the energy stored in the thermal energy harvesters' capacitances is transferred to a buffer through coupled inductors when one of the Thermal Energy Harvesters reaches its maximum output voltage.

As for the WSN, a GreenNet node (platform developed by ST) has been programmed to work in an asynchronous operation mode to reduce its power consumption (Fig. 3b). The GreenNet emission circuit transmits 64 bits of data with IEEE 802-15-4 protocol toward a GreenNet reception module.

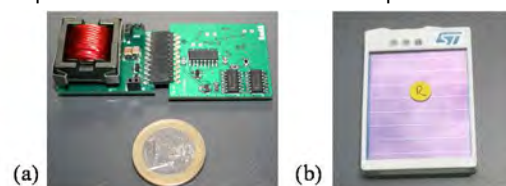


Figure 3: (a) discrete power management circuit and (b) Wireless Sensor Node (GreenNet).

The thermal energy harvesters combined to a power management circuit have enabled to supply a GreenNet temperature node and to transmit information to the reception module at least once every 30 s without battery, which is already compatible with many use cases and especially to monitor the temperature of industrial equipment.

### Related Publications:

[1] J. Boughaleb et al., "SPICE modelling of a coupled piezoelectric-bimetal heat engine for autonomous Wireless Sensor Nodes (WSN) power supply", 14<sup>th</sup> Int. Conf. on Micro and Nanotechnology for Power Generation and Energy Conversion Applications (PowerMEMS 2014), Boston, MA, 1-4 Dec. 2014.



## Power generation from liquid motion combined with electret-based converters

Research topics: energy harvesting, electrostatic conversion

M. Perez, S. Boisseau, J.-L. Reboud (G2ELab)

**ABSTRACT:** We report on a liquid-based electrostatic harvester composed of an air gap capacitor, partially filled with a liquid and coated on one side by a 25  $\mu\text{m}$ -thick Teflon PTFE electret. As the liquid moves into the gap due to external forces, the capacitance of the energy harvester changes, directly generating electricity with the electret-based converter. Water and oils have been tested in the cavity. Preliminary experiments have been performed on a 32  $\text{cm}^3$  cavity leading to an output power of 400 nW with an electret initially charged at -500 V.

Over the last decade, more and more researchers have tried to include liquids in electrostatic harvesters to turn mechanical movements into electricity. Actually, liquids present many advantages for electrostatic energy harvesters. First, liquids can conform to any shape, enabling to reach high capacitances in electrostatic harvesters. Secondly, liquids are less subject to ageing than mechanical pieces in movement. Finally, we can expect stable performances over broad frequency ranges in contrast to resonant devices. This work focuses on a structure made of a parallel-plate capacitor (black lines in Figure 1) partially filled with a fluid and polarized by a Teflon electret (red line in Figure 1). Ambient movements induce a motion of the liquid inside the cavity, leading to a variation of capacitance which is finally converted into electricity with the electret (polarization source of the electrostatic converter).

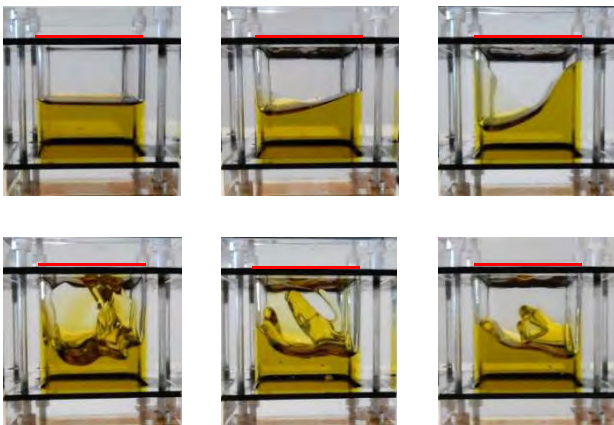


Figure 1: 4 cm-width prototype in operation with oil at 4 Hz.

Like standard electret-based converters, the output power of the liquid-and-electret-based converter we propose is directly proportional to the oscillation frequency ( $f$ ), the square of the surface voltage of the electret ( $V^2$ ), and the variation of capacitance of the energy harvester ( $C(t)$ ), which should be maximized.

While the oscillation frequency and the surface voltage of the electret are set by the environment of the harvester and the dielectric material selected, the capacitance variation depends on the geometry of the harvester, the permittivity of the liquid and should be maximized.

16  $\text{cm}^2$  cavities with various thicknesses, metallized on both sides and covered on one side by a 25  $\mu\text{m}$ -thick electret

charged at -500 V by a corona discharge, have been manufactured. Power generation experiments have been performed on a shaker driven with a horizontal sine movement.

Experimental output powers for various liquids are presented in Table 1 and typical output voltages are displayed in Figure 2.

Frequency (Hz)	Average power generated (nW)			
	Water	Paraffin oil	Olive oil	Aluminum beads
4	44.0	1.1	1.3	4.0
5	99.3	1.8	1.5	4.0
9	396.3	4.6	5.2	18.6
10	222.8	5.4	7.0	18.5
11	180.7	6.2	9.1	80.2
13	164.1	13.1	15.8	127.2

Table 1: Average power generated for various liquids and various frequencies.

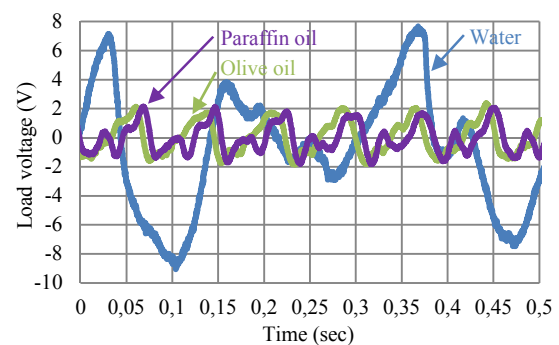


Figure 2: Typical output voltages on a 100  $\text{M}\Omega$  load (oil at 13 Hz and water at 9 Hz).

These first experimental results enable us to better understand the issues of liquid-and-electret-based energy harvesters. Various liquids (conductive and dielectric) have been tested and first output powers in the 100 nW-1  $\mu\text{W}$  range have been extracted. Our efforts are now focused on protection layers to avoid electrets discharges and on the maximization of the capacitance variation in oil process, in order to increase the output powers of these devices.

### Related Publications:

[1] M. Perez, S. Boisseau, J.-L. Reboud, "Power generation from liquid motion combined with electret-based converters", 4èmes Journées Nationales sur la Récupération et le Stockage d'Énergie pour l'alimentation de microsystèmes autonomes (JNRSE 2014), Annecy, France, 7-8 April 2014.

## An autonomous power management circuit for piezoelectric energy harvesters

Research topics: energy harvesting, power management

P. Gasnier, J. Willemin, S. Boisseau, C. Condemine, S. Robinet

**ABSTRACT:** A fully autonomous power management circuit (PMC) based on an Integrated Circuit (IC) and a discrete power circuit is presented. This PMC efficiently converts the raw output power of mechanical Energy Harvesters (EH) into an unregulated 3 V supply source compatible with Wireless Sensor Nodes (WSNs). It autonomously harvests power from 10  $\mu\text{W}$  to 500  $\mu\text{W}$  and operates with high output-voltage harvesters up to 200 V. It performs an efficient energy extraction thanks to an off-chip inductive element and an accurate control strategy. Furthermore, the PMC self-starts and does not need any battery to operate.

In dusty or dark environments submitted to shocks, stresses or vibrations, where solar energy is unreliable or non-existent, mechanical energy harvesting is a pertinent candidate to power Wireless Sensor Nodes (WSN). The piezoelectric principle is a relevant solution to convert mechanical energy into electrical energy: in addition to its low cost and its availability, it offers a high power density at micro and macro scales and low mechanical frequencies. The output power of piezoelectric harvesters is generally in the 10  $\mu\text{W}$  to 1 mW range but their high AC output voltages are not compatible with standard electronic circuits' requirements.

As a consequence, a power management circuit is essential to turn the piezoelectric raw output into a viable supply source for WSNs. Synchronous Electric Charge Extraction (SECE) is a technique to enhance the energy extraction compared to a full-bridge rectifier and a capacitor. SECE consists in entirely discharging the piezoelectric harvester in a coil when its voltage reaches a maximum.

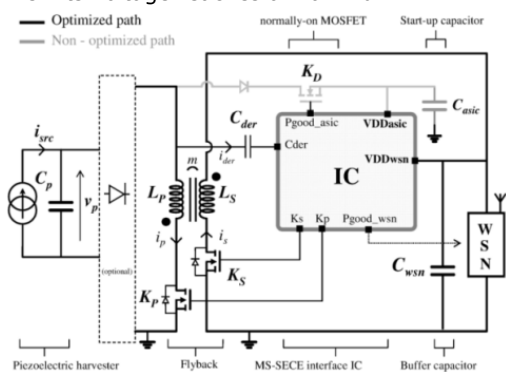


Figure 1: Schematic of the PMC.

The architecture of the PMC is depicted in Fig. 1. It is based on an IC surrounded by discrete components. Its main features are explained below:

- The Flyback ( $L_p$ ,  $L_s$ ,  $K_p$ ,  $K_s$ ) is used to perform an enhanced SECE technique called MS-SECE ("Multi-Shot" Synchronous Electric Charge Extraction): the piezoelectric harvester is discharged in  $N$  successive energy transfers by precisely controlling  $K_p$  and  $K_s$  when the piezoelectric voltage reaches a maximum. This novel technique enables to reduce the volume of the power circuit or to improve the efficiency of the energy transfer compared to SECE, by reducing conduction losses.

- The system is based on two energy paths to implement a self-starting battery-free operation mode. Two storage capacitors are used:  $C_{asic}$  supplies the IC and  $C_{wsn}$  is dedicated to the WSN. The "optimized path" implements the MS-SECE technique by controlling  $K_p$  and  $K_s$ . The piezoelectric harvester is then discharged through the Flyback circuit to charge  $C_{wsn}$  in an optimal way. The "non-optimized path", which connects the harvester to  $C_{asic}$ , is used in the two following cases: during the cold start of the system and periodically when  $C_{asic}$ 's voltage falls below a minimum value.

Fig. 2a shows in (1) the cold-start of  $C_{asic}$  (1-10  $\mu\text{F}$ ) through  $K_d$  (the non-optimized path), in (2) the charge of  $C_{wsn}$  by MS-SECE (Fig. 2b), during which  $V_{DDasic}$  decreases and in (3) the operation of a WSN powered when  $C_{wsn}$  (100-500  $\mu\text{F}$ ) is filled. The WSN is based on a Texas Instrument CC430 platform consuming 100 to 200  $\mu\text{J}$  per operation, including a temperature measurement and an 868 MHz RF transmission.

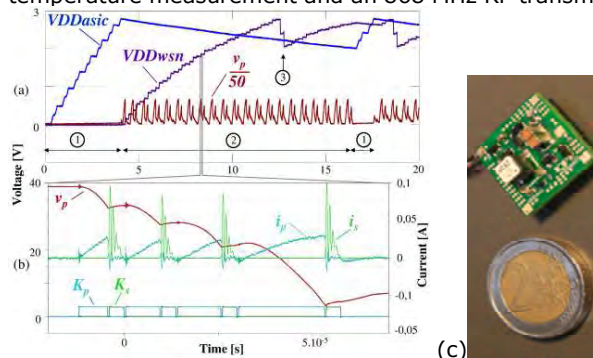


Figure 2: a) Experimental time-domain waveforms during a complete operation, (b) zoom on a 4-shot discharge, (c) whole PMC compared to a 2 euro coin.

The PMC self-starts and operates with capacitors as storage elements. Furthermore, thanks to the off-chip Flyback topology, it is not limited in terms of tolerated piezoelectric voltages, enabling the use of a low voltage and low cost technology for the ASIC. This circuit consumes 1  $\mu\text{W}$  @ 5 Hz. It is shown that MS-SECE increases the efficiency of the energy transfer by 15% and up to 25%. The PMC and the MS-SECE technique also enable to use small inductive components to discharge a considerable quantity of energy without reaching the saturation induction. Its overall volume is less than 3  $\text{cm}^3$  as shown in Fig. 3c.

### Related Publications:

- [1] P. Gasnier, J. Willemin, S. Boisseau, G. Despesse, C. Condemine, G. Gouvernet and J.-J. Chailout, "An autonomous piezoelectric energy harvesting IC based on a synchronous multi-shots technique", *IEEE Journal of Solid-State Circuits*, vol.49, no.7, July 2014, pp. 1561-1570.
- [2] P. Gasnier, J. Willemin, S. Boisseau, G. Despesse, C. Condemine, G. Gouvernet and J.-J. Chailout, "An autonomous piezoelectric energy harvesting IC based on a synchronous multi-shots technique", *39th European Solid-State Circuits Conf. (ESSCIRC)*, Bucharest, Romania, 16-20 Sept. 2013.

## Online estimation of Li-ion batteries electrical impedance

Research topics: Battery Monitoring System, impedance tracking

H. Piret, P. Granjon, V. Cattin, N. Guillet

**ABSTRACT:** a new method to estimate and track the variations of a lithium ion battery electrical impedance is presented. This algorithm relies on a recursive implementation of a wideband frequency estimation method based on Fourier transforms. Its estimation performance and tracking capability are tuned thanks to a unique parameter called the forgetting factor. The method reaches good estimation performances and allows continuous tracking of battery impedances.

The development of electrical vehicles inevitably leads to the improvement of efficient battery management systems (BMS) in order to provide more representative informations of the present state of the battery. The electrical impedance describes the dynamic behavior of the battery and regularly changes with the evolution of the battery temperature, state of charge and state of health. In this context, we develop an algorithm dedicated to the battery electrical impedance estimation, which is efficient enough to track accurately the time variations of this quantity and to be embedded in a vehicle or a nomad device. This algorithm relies on wideband signals used with a frequency domain estimation method recursively implemented.

The battery dynamics depend on several internal and external parameters, such as its polarization current, its states of charge and health, as well as its internal temperature. In what follows, all these parameters are assumed to be constant, and the input current variations are imposed to be small enough for the battery to be considered as a linear and time-invariant (LTI) system during each measurement. Its electrical impedance  $Z(f)$  can thus be theoretically defined by the ratio between the cross power spectral density (CPSD)  $S_{ui}(f)$  between voltage and current and the power spectral density (PSD)  $S_{ii}(f)$  of the current. It has been shown previously [1] that this method leads to a correct estimation of the battery impedance over a given frequency band, but is unable to follow its possible variations during the measurement time.

The new version proposed [2] relies on a recursive average to estimate the CPST and PDS. As an example, the following equation gives the algorithm used to recursively estimate the CPST, where  $a \in [0, 1[$  is the forgetting factor, and  $\hat{P}_{ui(k)}(f)$  is the cross-periodogram of the  $k^{\text{th}}$  blocks of voltage and current signals:

$$\hat{S}_{ui(k)}(f) = a\hat{S}_{ui(k-1)}(f) + (1-a)\hat{P}_{ui(k)}(f)$$

When  $a = 0$ , no average is performed and the battery impedance is simply estimated by the ratio of the Fourier transforms of the voltage and the current, leading to poor estimation performance regarding measurement noise. When  $a$  increases, the power spectral densities involved in the impedance estimation are more and more averaged, and the final estimator converges to the result obtained in the non-recursive case when  $a \rightarrow 1$ .

We compare the estimation performance of this recursive version with that of a classical galvanostatic electrochemical impedance spectroscopy (GEIS), and a non-recursive estimation algorithm, on a commercial lithium nickel manganese cobalt oxide (NMC)/Graphite battery. Figure 1 shows the Nyquist plots obtained with a forgetting factor  $a = 0.9$ . The non-recursive estimation is close to the result obtained through the usual GEIS thanks to an average over the whole data set. On the contrary, the recursive estimate is noisier because it is averaged over a smaller local window whose size is set by using the forgetting factor. This parameter controls the length of the convergence time and the quantity of fluctuations around the final error.

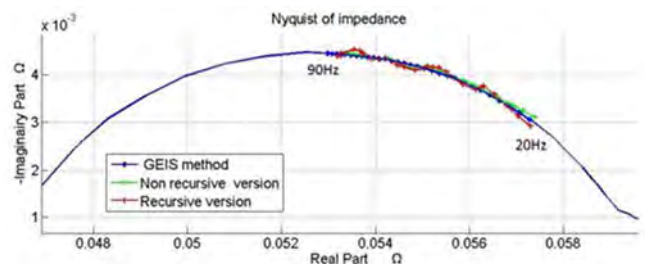


Figure 1: estimated impedances between 20 Hz to 90 Hz by using the three methods.

Fig. 2 highlights the influence of this parameter on the learning curve of the algorithm. When  $a$  is close to 1 (red curve) a large convergence time is obtained ( $\sim 2.5$  s) with small final estimation error and fluctuations. For a smaller value (black curve), the convergence time is much shorter ( $\sim 1$  s) but the final error and fluctuations are increased.

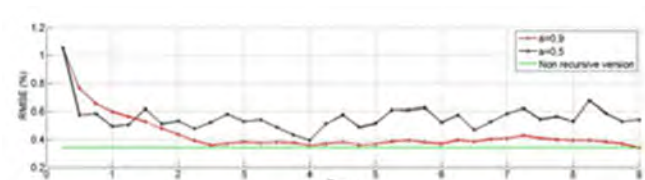


Figure 2: learning curves for  $a = 0.5$  (black),  $a = 0.9$  (red), and the non-recursive algorithm (green).

These results highlight the existence of a trade-off between the obtained convergence time (related to the tracking capabilities of the algorithm) and the final estimation error (related to the estimation performance of the algorithm). In the near future, this algorithm will be implemented in an embedded system and applied to a test bench in real-time.

### Related Publications:

- [1] R. Al Nazer, V. Cattin, P. Granjon, M. Montaru, M. Ranieri, "Broadband identification of the battery electrical impedance for HEVs", *IEEE Trans. on Vehicular Technology*, vol. 62, no. 7, Sept. 2013, pp. 2896-2905.  
 [2] H. Piret, P. Granjon, V. Cattin, N. Guillet, "Online Estimation of Electrical Impedance", *7<sup>th</sup> Int. Workshop on Impedance Spectroscopy*, Chemnitz, Germany, 24-26 Sept. 2014.







# 6

## PhD degrees awarded in 2014

*Kameni Ngassa Christiane*

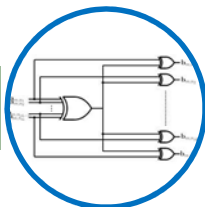
*Zevallos Luna José Alberto*

*Rutkowski Jaroslaw*

*Gasnier Pierre*

*Al Nazer Rouba*

## PhD degrees awarded in 2014



**Kameni Ngassa Christiane**

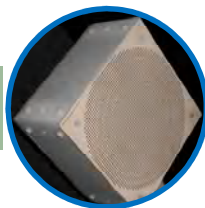
University: Cergy-Pontoise

### LDPC decoders running on error prone devices: theoretical limits and practical assessment of the error correction performance

Error correction decoders built out of unreliable components have attracted an increasing interest over the last few years, as reliability issues emerged as one of the greatest challenges for future generations of integrated digital circuits. This thesis focuses on the class of LDPC codes decoded with iterative message-passing (MP) decoders running on faulty hardware.

The theoretical analysis and understanding of the noisy Min-Sum (MS) decoder, by using a noisy density evolution approach, showed that it can operate when its different computational units are noisy, and we determined the hardware noise parameters allowing the decoder to achieve a target error probability. Additionally, the practical performance of several decoders was verified through Monte-Carlo simulation in the non-asymptotic case. Our results showed that the Self-Corrected MS (SCMS) and the stochastic decoders are very robust to transient errors, providing nearly the same performance as their noiseless counterparts. We also investigated the impact of specific hardware implementations on the error correction performance of noisy MS and SCMS decoders, and a complementary error scenario consisting of the imprecise arithmetic framework.

Our investigations on noisy SCMS and Stochastic decoders reveal the significant role that memory mechanisms (e.g. the self-correction rule within SCMS, or edge-memories within stochastic decoder) play in increasing the robustness to hardware noise. Although such memory mechanisms are themselves faulty, they allow detecting or correcting a number of errors that largely surpass the number of errors induced by their implementing circuits. Moreover, we also focus on alternative means to improve the MS and SCMS reliability, by protecting critical bits within the decoding process. The benefits of this approach are assessed through both asymptotic DE analysis and finite-length Monte-Carlo simulation.



**Zevallos Luna José Alberto**

University: Grenoble

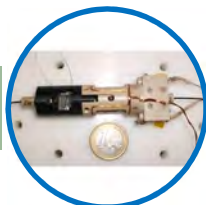
### Integrated antennas for wireless devices at millimeter-wave frequencies

This thesis investigated the integration of antennas on silicon substrates at millimeter-wave frequencies in order to obtain fully-integrated and packaged transceiver modules using standard technologies.

We investigated first the design and realization of integrated antennas in a standard QFN package coupled to a 60 GHz Ultra-Wide-Band (UWB) transceiver chip with two integrated folded-dipole antennas implemented in a 65-nm CMOS-SOI technology on high-resistivity silicon. We defined a simulation model from which we studied the performance of integrated antennas, taking into account the influence of the environment (package, lid, wirebonding and manufacturing technology). Then, we optimized the antenna performances in impedance matching and radiation gain using radiating elements printed on a substrate and coupled to the on-chip folded dipoles. This antenna led to the demonstration of high-data rate communications (up to 2.2 Gbps) with a very low power consumption. We showed that the communication distance can be extended up to several meters using a transmit array printed on a low-loss substrate.

Next, we investigated the design and realization of a multi-beam antenna in V-band for long-range applications; it is based on a transmit-array realized in standard printed technologies associated with a focal source array, which consists of a small number of integrated antennas on silicon in order to achieve a good compromise between the radiation gain, the cost and the beam steering capabilities. Several arrays were demonstrated with a circularly-polarized beam, a gain of 18.6 dBi and a beam-steering capability of  $\pm 24^\circ$ .

## PhD degrees awarded in 2014



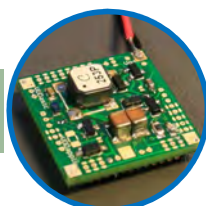
**Rutkowski Jaroslaw**  
University: Franche-Comté

### Study and realization of a miniature isotropic helium magnetometer

Optically-pumped magnetometers suffer from dead zones and heading errors limiting their accuracy. In the SWARM project funded by the European Space Agency, CEA-LETI has successfully designed and manufactured an isotropic  $^4\text{He}$  magnetometer with a  $1 \text{ pT}/\sqrt{\text{Hz}}$  resolution (DC-100 Hz) and an accuracy better than 45 pT. Its isotropy is obtained thanks to a nonmagnetic servo-driven piezoelectric motor which sets the linear polarization angle of the pumping light with respect to the magnetic field to be measured. This thesis focused on the miniaturization of this isotropic helium-4 magnetometer, which first required a study of the scaling laws of the sensor. To this end, a theoretical model has been developed and showed a good agreement with experimental measurements of key parameters (metastable atom density and their relaxation time). The model allows to predict the optimal pressure, with which the glass cells of the miniature magnetometer have to be filled as well as the theoretical shot noise level of the miniature sensor.

The miniaturization required also a redefinition of the system architecture and the replacement of some components. A polarization rotator based on liquid crystals has been identified as a replacement of the piezoelectric motor previously used. This device has a large miniaturization potential and is fully compatible with semiconductor batch processing. Sample structures have demonstrated a continuous polarization rotation from  $0^\circ$  to more than  $300^\circ$  with response times compatible with mobile or space applications. The construction and the electrical driver of this liquid crystal polarization rotator are nonmagnetic.

In the next step, a first demonstrator of a miniature isotropic  $^4\text{He}$  magnetometer has been designed and characterized. An overall magnetic field sensitivity around  $8 \text{ pT}/\sqrt{\text{Hz}}$  has been obtained using a  $100 \text{ mm}^3$  glass-blown gas cell and the liquid crystal rotator. This sensitivity can be further optimized. Finally, first steps towards a "chip-scale" package of the sensor have been realized with promising results obtained from the experimental test of microfabricated glass-silicon-glass helium cells confirming the confinement of helium.



**Gasnier Pierre**  
University: Grenoble

### A mechanical energy harvesting circuit to power wireless sensor nodes

Energy harvesting is a relevant solution to replace primary batteries in autonomous systems. As part of a joint project between CEA and Oxylane (Decathlon), this thesis aimed at designing a power management circuit for harvesting mechanical energy from human movements during sport practice in order to power a Wireless Sensor Node (WSN). The electronic circuit recovers the energy from piezoelectric harvesters, extracts and conditions it thanks to an efficient energy extraction technique and to an appropriate power circuit. In response to the random behavior of human body which supplies an intermittent and irregular energy, the Flyback topology and the Synchronous Electric Charge Extraction technique (SECE) are employed. The energy harvester is discharged at its maximum voltage through a coupled-inductor and two MOSFETs transistors. This work proposes a new extraction technique, derived from SECE: MS-SECE ("Multi-Shot Synchronous Electric Charge Extraction") transfers the energy in several magnetic discharges in order to decrease the resistive losses or the size of the magnetic component. In order to satisfy the size constraints, an integrated circuit, fabricated in the AMS  $0.35 \mu\text{m}$  CMOS technology, implements the MS-SECE autonomously. This very low power ( $1 \mu\text{W}$ ) ASIC controls the power circuit and a couple of external components. This way, the electrical energy is efficiently converted towards a buffer capacitor under 3V. Furthermore, thanks to its two operating modes (passive/non optimized and active/optimized), the circuit self-starts and works without battery or initial energy. The complete system is compatible with a large variety of piezoelectric harvesters, especially when their output voltages are large ( $>50\text{V}$ ) and enables the full autonomy of a WSN consuming around  $100 \mu\text{W}$ .

## PhD degrees awarded in 2014



**Al Nazer Rouba**  
University: Grenoble

### Embedded electrical impedance measurement system for Li-ion batteries

Embedded electrical impedance measurement is a key issue to enhance battery monitoring and diagnostic in a vehicle. It provides additional measurements to those of the pack's current and cell's voltage to enrich the aging's indicators and the battery states. A classical method for battery impedance measurements is the electrochemical impedance spectroscopy (EIS). A sinusoidal signal current (or voltage) of a variable frequency sweeping over the range of interest is generated at the input of the battery and the voltage (or current) response is measured. An active identification technique based on wideband signals composed of square patterns was proposed. Particularly, simulations were used to compare the performance of different excitation signals commonly used for system identification in several domains and to verify the linear and time invariant behavior for the electrochemical element.

The performance estimation was performed using a specific quantity: the spectral coherence. This statistical value was used to give a confidence interval for the module and the phase of the estimated impedance. It allowed the selection of the frequency range where the battery meets the assumptions imposed by the non-parametric identification method. To experimentally validate the previous results, an electronic test bench was designed. Experimental results were used to evaluate the wideband frequency impedance identification. A reference circuit was first used to evaluate the performance of the methodology. Then, experimentations were done on a Li-ion battery and comparative tests with EIS were realized. The specifications were established using a simulator of Li-ion battery. They were used to evaluate the performance of the proposed wide band identification method and determined its usefulness for the battery states estimation: the state of charge and the state of health.





# Greetings

## **Editorial committee**

Laurent Dussopt  
François Vacherand  
Dominique Noguét  
Sébastien Dauvé

## **Coordination and graphic design**

Hélène Vatouyas

## **Photos**

© CEA-LETI /G. Cottet





# Systems and Solutions Integration

**Contacts**

**Roland Blanpain**

Head of Systems & Solutions Integration Division  
roland.blanpain@cea.fr

**François Vacherand**

Deputy Manager Systems & Solutions Integration Division  
francois.vacherand@cea.fr

**Céline Soubeyrat**

Program Manager  
celine.soubeyrat@cea.fr

**Jean-Michel Léger**

Program Manager  
jean-michel.leger@cea.fr

**Dominique Noguét**

Head of Telecoms and Security Lab.  
dominique.noguét@cea.fr

**Sébastien Dauve**

Head of Sensors and Systems Lab.  
sebastien.dauve@cea.fr

**Tiana Delhome**

Head of Innovation Lab.  
tiana.delhome@cea.fr



**leti**



CEA-Grenoble  
17, rue des Martyrs  
F-38054 Grenoble Cedex 9  
(+33) 4 38 78 37 29  
[www.leti.fr](http://www.leti.fr)



© CEA 2014. All rights reserved.  
any reproduction in whole or  
in part on any medium or use  
of the information contained  
herein is prohibited without  
the prior written consent of CEA.